Hoang, Duc Quang (2011) *A study of tailored domain wall geometries in ferromagnetic nanowires using Lorentz microscopy.* MSc(R) thesis.

http://theses.gla.ac.uk/4255/

Copyright and moral rights for this thesis are retained by the author

A copy can be downloaded for personal non-commercial research or study, without prior permission or charge

This thesis cannot be reproduced or quoted extensively from without first obtaining permission in writing from the Author

The content must not be changed in any way or sold commercially in any format or medium without the formal permission of the Author

When referring to this work, full bibliographic details including the author, title, awarding institution and date of the thesis must be given

Glasgow Theses Service
http://theses.gla.ac.uk/
theses@gla.ac.uk

A THESIS

FOR THE MSc(R) DEGREE OF PHYSICS

A Study of Tailored Domain Wall Geometries in Ferromagnetic Nanowires using Lorentz Microscopy

SCHOOL OF PHYSICS AND ASTRONOMY

COLLEGE OF PHYSICAL SCIENCE AND ENGINEERING

UNIVERSITY OF GLASGOW

DUC QUANG HOANG

SEPTEMBER 2011

CONTENTS

ABBREVIATIONS

AC	Alternating current
AFM	Anti-ferromagnetic
ATDW	Asymmetric Transverse Domain Wall
BF	Bright Field
CCD	Charge Coupled Device
CDF	Centered Dark Field
CCW	Counter Clockwise
CTEM	Conventional TEM
CW	Clockwise
DC	Direct current
DF	Dark Field
DM	Diamagnetic
DPC	Differential Phase Contrast
DW	Domain Wall
DWTC	Domain Wall Trap Chain
EBL	Electron Beam Lithography
FEG	Field Emission Gun
FFT	Fast Fourier Transform
FIB	Focused Ion Beam
FM	Ferromagnetic
FWHM	Full-Width-Half-Maximum
H	Magnetic field
H_{d}	Demagnetizing field
H_{inter}	Internal field
H_{ext}	External magnetic field
H2H	Head-to-Head
HMS	High Magnification Scanning
HRTEM	High Resolution TEM
J	exchange integral
LAD	Low Angle Diffraction

LL	Landau-Lifshitz
LLG	Landau-Lifshitz-Gilbert
LMIS	Liquid Metal Ion Source
LMS	Low Magnification Scanning
LTEM	Lorentz TEM
M	Magnetization
M_S	Saturation Magnetization
MOKE	Magneto-optic Kerr Effect
MRAM	Magnetoresitive Random Assess Memory
MTJ	Magnetic Tunneling Junction
OAF	Objective Aperture Function
OOMMF	Object Oriented Micro-Magnetic Framework
PCTF	Phase Contrast Transfer Function
PM	Paramagnetic
Py	Permalloy
SEM	Scanning Electron Microscopy
STDW	Symmetric Transverse Domain Wall
STXM	Scanning Transmission X-ray Microscopy
T_C	Critical temperature
T_N	Néel temperature
TDW	Transverse Domain Wall
TEM	Transmission Electron Microscopy
T2T	Tail-to-Tail
UHV	Ultra High Vacuum
VDW	Vortex Domain Wall
XMCD	X-ray Magnetic Circular Dichroism

LIST OF FIGURE CAPTIONS

Chapter 1 Overview and Fundamentals of Ferromagnetism in Nanostructures

Fig. 2.4 (a) Parallel incident electrons are reflected from (*hkl*) planes and interference occurs when the path difference satisfies Bragg's conditions, (b) and (c) are recorded diffraction patterns from an evaporated single crystal film of Gold, Au(100) and a 20 nm-thick polycrystalline permalloy nanowire, reproduced from ref. [13].

Fig. 2.5 Simplified schematics of (a) full diffraction (b) bright field (c) dark field and (d) centered DF imaging modes. The insets illustrate the principle of electron diffraction in the TEM for the BF and the centered DF imaging modes.

Fig. 2.6 High resolution TEM images of a magnetic tunnel junction (MTJ), structured as Si/electrode/Ta(5)/$Mn_{74}Ir_{26}$(15)/$Co_{82}Fe_{18}$(3)/Ru(0.8)/$Co_{74}Fe_{16}B_{10}$(4)/MgO(3)/$Co_{74}Fe_{16}B_{10}$(3)/Ru (5)/Ta(5)/ (units in nm). The images of the MTJ structure were taken in (a) BF and (b) CDF modes, respectively. A brighter line within layers in the BF image is the barrier layer, it can be seen easily, whereas it is hard to distinguish in the DF image where the homogeneous barrier layer is not dominate in the dominant contrast. However, the *Z* contrast is improved in the DF image for IrMn layer. This specimen was provided by Dr. R.J. Macedo at INESC-MN, Portugal.

Fig. 2.7 (a) Simplified diagram of the electrons deflected by the classical Lorentz force, (b) is intensity profile of transmitted electrons at position below the specimen where valley and peak correspond to darker and brighter bands are shown in (c). (d) is a Fresnel image of 20nm-thick continuous Py film which shows domain walls on magnetic ripple background and (e) is a patterned magnetic permalloy element with a transverse domain wall appears as dark and white boundaries.

Fig. 2.8 (a) A defocused Fresnel image of Au cross-grating with the lattice periodicity of 463nm-cell-size and (b) its FFT image where 6 points are shown which correspond to 6 spatial frequency values, (c) k^2 versus ring number as a linear function when the PCTF crosses ***k***-axis.

Fig. 2.9 (a) Simplified schematic of the electrons with different paths (p_1 and p_2) from a high coherence source interact with a magnet associated with the Ampérian current are virtually turned around where phase shift belongs to the different of the paths (Δp) is considered in a quantum mechanical approach. (b) is an evolution of an electron plane wavefront as it traverses a magnetic material with a single domain.

Fig. 2.10 (a) Schematic of the magnetic phase change when electrons traverse a magnetic specimen consists of 180°-walls. Magnetic phase profile of emergent electron wave form at the back focal plane, derivative and Laplacian are alternatively illustrated. (b) image intensity profiles of

phase shift (Φ_m), electrostatic phase (Φ_e) and the sum of two phase contributions.

Fig. 2.11 A vortex domain wall was simulated by OOMMF for a 19.5nm-thick permalloy nanowire with the dimension of 400nm×2500nm. (a) the output OOMMF image; (b) and (c) are the M_x and M_y components of magnetization; (d), (e) and (f) are calculated magnetic phase, electrostatic phases and magnetic plus electrostatic phase, respectively. The magnetic phase is differentiated to obtain the orthogonal induction maps. The images are sensitive to magnetic induction components indicated by red arrows, as shown in (g) and (h); (i) is the color DPC image included magnetic phase only; (j), (k) and (l) are the Fresnel images calculated from the purely magnetic phase, included magnetic plus electrostatic plus amplitude effects, and *curl*$(M)_z$ (see equation (2.15)), respectively. The Fresnel images with the purely magnetic phase and included effects were calculated in the conditions of C_s=8000mm, λ=2.51pm and defocused value of 1μm.

Fig. 2.12 (a) A specimen mounted in the sample rod where the specimen can be magnetized by DC field when objective lens on, (b) is presented parallel and perpendicular magnetic field components applied in the specimen.

Fig. 2.13 Simplified diagram of a thin film sample is magnetized by pulsed fields which were produced by the traditional designed magnetizing stage [13].

Fig. 2.14 (a) A schematic of the method to calculate DPC signal from the quadrant detector where the convergence angle of the incident beam (α) and deflection angle (β_L) are projected on the detector, described as α and β_L distances. (b) Two orthogonal DPC images of 10nm-thick-patterned Py-nanowire with dimension of 500nm-width×10μm-length where a transverse domain wall was created (details are to be discussed in chapter 3)

Fig. 2.15 (a) and (b) represent a BF image and its sum signal level, while (c) and (d) show a DPC image was taken from different quadrant and its signal level, respectively. Here, the green dash-bar shows the area was scanned crossing the mean width of a nanowire where the signals were summed. Moreover, the red and pink dash-bars also represent scanned areas in either sides of a H2H-TDW where the signal levels were taken from and shown as red and pink dashed-lines in the lower panels.

Fig. 2.16 Schematic of single membrane: front side, back-side and cross-section of a continuous permalloy thin film evaporated onto the membrane.

Fig. 2.17 Schematic of a thin film evaporator used in this thesis.

Fig. 3.5 presents a simulated image of 500nm wide-21nm-thick straight nanowire. Here, a demonstration of MatLab calculation in the 500nm-width nanowire where big and small halves of the TDW are overlayed by red and green backgrounds. Magnetization components existing in each area are also presented.

Fig. 3.6 Wall phase diagram of symmetric-asymmetric TDWs of simulated straight-nanowires in differing widths and thicknesses: (a) is normalized degree of asymmetry in TDWs in variations of nanowire-widths and thicknesses; (b) is ratio of magnetization components (M_x, M_y) as a function of nanowire-widths. The red and blue symbols are presented the transition points of VDW↔ATDW and ATDW↔STDW, respectively, the results are taken from ref. [7], in which the STDW, ATDW and VDW were defined based on their ground states. The violet symbols are presented a particular nanowire with 10.5nm-thick which will be considered extensively in this thesis.

Fig. 3.7 Selected colour simulated Fresnel images of 10.5nm-thick nanowires of different widths (a), with the normalized values of the two areas inside TDWs (b). Here, the smaller areas (blue-circle-symbols) increase more slowly with increasing widths, than larger areas (red-square-symbols). The inset of (b) shows two simulated Fresnel images of 200nm and 400nm wide nanowires with 21 nm-thick which indicates the right-wall-edge is inflected at a point if nanowire width is increased.

Fig. 3.8 Degree of transverse domain displacement in different spin configurations at the anti-notch of 10.5nm-thick straight nanowire with dimension of 300nm-width×2500nm-length: the DW displacements from the anti-notch are 0 nm, 24nm and 56 nm which correspond to the spins are pinned along (a) +Oy-direction [↑], (b) free and (c) -Ox direction [←], respectively. The displacements and spin configurations (at the anti-notch) of these DW configurations are different however the degree of asymmetry values is mostly similar.

Fig. 3.9 (a) A missing pixel was created at different positions along the long edge of the 300nm-width-straight-10.5nm-thick nanowire where the initial state of the simulation is a triangle which a vertex at the anti-notch is virtually divided into 30° and 40° angles. (b) A Fresnel image of the 300nm-width perfect nanowire at the relaxed state where two natural wall edges are occurred at ~27.5° and ~34.7° in either sides of the dividing line, respectively. (c) Normalized degree of asymmetry as a function of missing pixel positions/angles for 100nm, 300nm and 500nm-width straight-nanowires and green- and red-dash lines indicate the two natural wall edges. (d) The results of normalized degree of asymmetry for 100nm, 300nm and 500nm-width nanowires with a missing pixel (red stars) which were added into the wall phase diagram of

10.5nm-thick-perfect straight nanowires in different widths (violet line).

Fig. 3.10 shows 300nm-width-straight nanowire with 10.5nm-thick was rotated in the negative direction/clockwise (a) and positive direction/counter-clockwise (b): From the top downward, the nanowire was rotated at a specific angle of ±45°, ±30°. The insets are shown the edge roughness in the long edges of the rotated nanowires. The arrows are indicated as orientations of the edge roughness which are similar to triangle shapes (triangle anti-notches) grown in different directions at the perfect edge which indicates as dash-lines. The different orientations are induced to variations in local potential energy landscape at the edges.

Fig. 3.11 (a) and (b) are Fresnel simulation images of the rotated nanowires in different angles of 0º, ±10°, ±30° and ±45° (from the top downward) and, (c) shows normalized degree of asymmetry in TDWs as a function of rotation angles and (d) presents the wall phase diagram for 10.5nm-thick-nanowire included the results observed in (c). The blue dashed-line indicates the transition point of STDWs↔ATDWs and the yellow-dashed-line which crosses the mean asymmetry values of the perfect nanowire without rotation.

Fig. 3.12 (a) is schematic of 300nm wide nanowire at the starting state of an OOMMF simulation where a triangle with the 100° angle located at the anti-notch is virtually divided into two sub-angles of 30° and 70°. (b) and (c) show simulated Fresnel images of 300nm-width-straight nanowires with 10.5nm-thick which were rotated in different angles, ±10°, ±30° and ±45° (from the top downward). Here, a triangle with 100°-angle located at the anti-notch was created as the starting state for all simulations.

Fig. 3.13 Grey (a) and color (b) Fresnel simulation images of 500nm-width-curved-nanowires of 10.5nm thickness: (a) an external field of 0.5T was applied perpendicular to the easy-axis which aims to generate H2H and T2T TDWs in either curvatures of the structure; (b) uneven edge roughness on either side of the same curved nanowire at the locations of the H2H and T2T TDWs (color images guide your eyes). The insets show particular regimes where irregular staircase behaviour occurred at the edge of the curved nanowire. The numbers of pixels that make up the irregular staircase are quoted above or below the edges.

Fig. 3.14 A demonstration of measuring degree of asymmetry in TDW using Digital Micrograph™ software, *i.e*., a simulated H2H-TDW Fresnel image in 500nm-width curved-nanowire.

Fig. 3.15 A set of created H2H and T2T TDWs in 10.5nm-thick curved nanowires with widths varying from 200 nm to 550 nm in 50 nm step.

Fig. 3.16 shows degree of asymmetry values of H2H and T2T TDWs in 10.5nm-thick-curved nanowire

as a function of nanowire-widths, respectively. The results are added into the wall phase diagram which was presented in Fig. 3.11(d) where they are presented as dark-red-pentagonal and square symbols.

Fig. 3.17 shows BF images of the curvatures of the patterned curved-nanowires of different widths. The images in the left and right panels correspond to the locations where H2H and T2T TDWs will be created by applying an external field perpendicular to the easy-axis.

Fig. 3.18 (a) is a Fresnel image of remanent state of 10.5nm-thick-patterned-500nm-width-curved nanowire where H2H (right) and T2T (left) TDWs were created by applying a perpendicular external field of 0.5T. In the insets, BF images are shown correspondently at the created H2H and T2T TDW locations. The inset in the top right is a schematic of external field directions correspond to the easy-axis of the nanowire. (b) Fresnel images of relaxed H2H TDWs were created in different external field directions and their schematics are shown underneath..

Fig. 3.19 is Fresnel images of relaxed DWs which were created by the 0°-field-orientation in patterned 10.5nm-thick-curved-nanowires with different widths. H2H and T2T DWs are shown in the left and right-panels, respectively.

Fig. 3.20 Degree of asymmetry values for TDWs in curved nanowires as a function of nanowire widths where the TDWs were created experimentally in different field directions: (a) and (b) are presented results for H2H and T2T TDWs, respectively. The results are presented by this way that aims to compare the experimental results with the simulation results that were presented in Fig. 3.16. Green dashed lines indicate the transition points between STDWs ↔ATDWs.

Fig. 3.21 Experimental results of averaged TDW asymmetry values for the curved nanowires (presented in Fig. 3.20) are plotted against the nanowire widths in combination with the simulation results of straight perfect nanowires (violet solid-circle-dashed line, this was also presented in the previous figures, Fig. 3.9(d), Fig.3.11(d) and Fig. 3.16). Results deriving from straight nanowires with a missing pixel are plotted as the yellow bound (which is defined by the two fitting lines from maxima and minima of the asymmetry values for 100 nm, 300 nm and 500 nm-width nanowires). Simulation results for rotated nanowires (dark cyan pentagon) and curved nanowires (wine solid symbols).

Fig. 3.22 DPC images of H2H TDWs in 10.5nm-thick-curved nanowire with 400nm-nanowire-width, the TDWs were created in different oriented-field directions, 0°, ±10° and ±20°. Results of degree of asymmetry in TDWs as a function of orientation field angles are shown in the graph. The arrows are indicated the sensitive directions of DPC signal.

Chapter 4 Conclusions and Further Work

Fig. 4.1 shows an SEM image of the optimal DWTC-like structure which will be contacted with Au-contacts in order to carry out current driven DW propagation. A DW is created at the first corner of the first nanowire (marked a by violet circle) and is subsequently propagated through the chain by an electrical current.

ABSTRACT

This work presents results on the degree of asymmetry in Transverse Domain Walls (TDWs) by means of micro-magnetic simulation and Lorentz microscopy. Here, head-to-head (H2H)-TDWs were simulated in straight permalloy (Py)-$Ni_{80}Fe_{20}$ nanowires. This aims to explore how to define symmetry and asymmetry of TDWs *via* a quantitative measurement of symmetry/asymmetry as described by a correlation between magnetization components (M_x, M_y) and region areas (A_1, A_2) inside TDWs. Experimentally, curved nanowires of differing widths were patterned by Focussed-Ion-Beam (FIB) irradiation. Lorentz microscopy experiments indicate that the degree of asymmetry of TDWs in the curved nanowires is strongly affected by structural effects, *i.e.* degree of edge roughness. Our results are a new route-map of quantitative measurement for transition between symmetric and asymmetric TDWs. The results are helpful for the determination of TDW configurations in the static state after the application of a magnetic field or electrical current pulse when TDWs are driven by magnetic field or current. Indeed, our results may support a greater understanding of DW creation and propagation in magnetic nanowires which are of interest for concepts of high-density and ultrafast nonvolatile data storage devices such as racetrack memory and magnetic logic gates.

ACKNOWLEDGEMENTS

First of all, I would like to give my sincere thanks to my supervisors, Dr. Stephen McVitie, Dr. Donald A MacLaren, Prof. John N Chapman who I not only a respect as teachers but also as my second fathers figure who helped me go further, scientifically.

During the course of this work, I have been honored to be attended workshops, conferences and the results are potentially considered to be published in respected SCI journals. Followings are the people who helped me attain these achievements.

First, I would like to express my deep appreciation to Ms. Lucy Murray, Dr. Maureen MacKenzie, Dr. Kerry O'Shea, Prof. Alan J Craven, Dr. Sam McFadzean, Dr. Ian MacLaren, Dr. Damien McGrouther, Dr. Nils Wiese, Mr. Brian Miller, Mr. Colin How, Mr. William Smith, Mr. Robert Beacham and other SSP (now MCMP) group members who have helped me since the inception and spent much time with me and who are the main reason for me completing this work. Their enthusiasm and passion has furthered my knowledge in the field of physics.

In the past, I wish to acknowledge Prof. Nguyen Huy Sinh, Prof. Seong-Cho Yu, Prof. Alexander Ulyanov, Prof. Suh- Kun Oh and Prof. Dong-Hyun Kim for their helpful comments and their enthusiasm and passion: as a teacher takes care of a student, a father takes care of his son and a brother takes care of his younger brother. On this occasion, I am indebted to all of my colleagues in the Slolid State Physics Group, Department of Physics and Astronomy, University of Glasgow, UK, in Applied Physics Lab., Department of Physics, Chungbuk National University, Korea and in Cryogenic Lab., Hanoi National University, Vietnam for their kindness and amicable cheers.

I would like to acknowledge the financial support from the SUPA for my research.

Finally, from the bottom of my heart I would like to give the best wishes to my parents, my wife and the members of my family. Their encouragement and words of cheer for my career are always effective and indispensable.

Glasgow, September 2011

DUC-QUANG HOANG

DECLARATION

This work was carried out by myself in the Materials and Condensed Matters Physics Group of the School of Physics and Astronomy at the University of Glasgow in the period 2007-2011. The results described herein are my own with the exception of the continuous Py film used in chapter 3 was provided by Dr. Damien McGrouther resulting from a collaboration with the Nanomagnetism Reseach Group at the University of Konstanz, Germany. This thesis has not previously been submitted for a higher degree.

Chapter 1

Overview and Fundamentals of Ferromagnetism in Nanostructures

In recent years the study of magnetic materials that have dimensions on the nanometre scale has become intense. In particular, the well-known ferromagnetic material, Permalloy (Py, $Ni_{80}Fe_{20}$) is of great interest due to its magnetic properties which can be exploited in applications including magnetoresistive random access memory (MRAM), read-head elements and high density recording devices [1-6]. Like most magnetic materials, the magnetic structure of Py can usually be separated into distinct regions where the local magnetization orientation is uniform. Each region with homogeneous magnetization is named a 'domain' and the boundary between two domains is known as a domain wall (DW), as illustrated in Fig. 1.1.

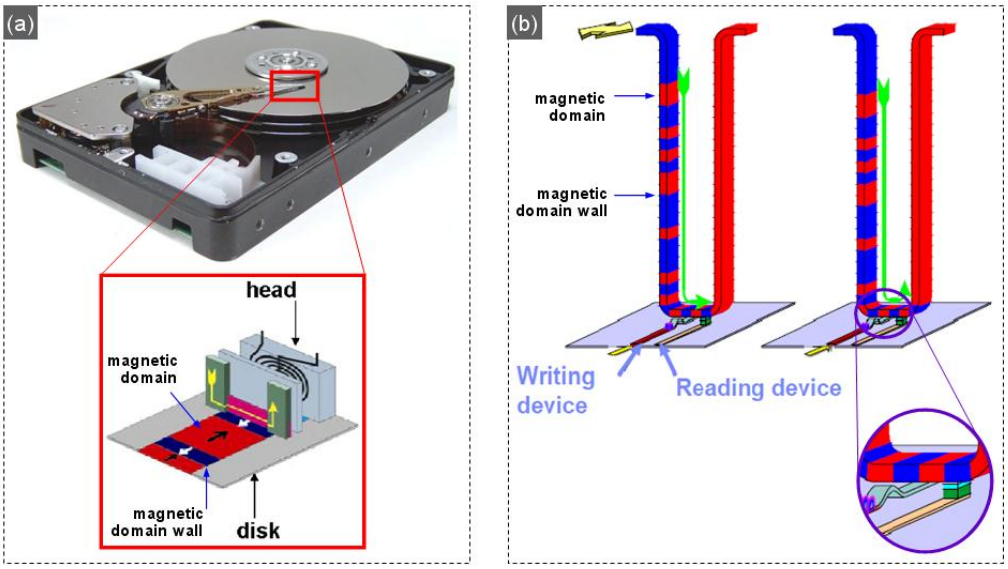

Fig. 1.1 (a) A current application of magnetic domains/ domain walls in recording media devices/ information storage, and (b) a future potential 3D magnetic device-racetrack memory, proposed by S.S.P. Parkin *et. al.* [2] in which domains/ domain walls can be propagated through nanowires by current pulses.

In Fig. 1.1 shows magnetic domain walls which are created in a fundamental magnetic device [1] and in a future potential 3D magnetic device [2]. The domains/domain walls are indicated as red and blue areas with magnetizations in opposite directions. The domain (or

equivalently the domain wall) is considered as a 'bit' of information in a data storage or processor device. An advantage of the racetrack memory is that DWs are used to store information in tall columns of magnetic material (Py) as shown in Fig. 1.1(b). Moreover, the DWs can be propagated in this architecture by using current pulses and subsequently DW transformation will be faster than that of the conventional device. If this 3D architecture is experimentally fabricated, information can be stored in such 3D magnetic devices are also higher than that in the conventional one as shown in Fig. 1.1(a). Thus, understanding domain wall behaviour (*e.g.*, DW configurations, propagation behaviour and effects of intrinsic and extrinsic parameters of Py) under the influence of an applied magnetic field or current is indispensable. Moreover, the domain/domain wall behaviour will also depend on material geometries at low dimension due to the shape anisotropy [1-6]. Indeed, a current 'hot-topic' in modern magnetism concerns the use of different shapes of Py material such as dots, wires or other restricted geometries where the main interest is how the magnetization changes in an applied field [1, 3, 5] or how it responds to an electron flow [2, 4, 6]. The motivation is to understand what happens on very small length scales or very fast time scales, when the structural dimensions become comparable to characteristic length scales [1, 2]. A number of experimental techniques including X-ray magnetic circular dichroism-XMCD [1], magneto-optic Kerr effect (MOKE) magnetometry [3], spin-polarized scanning electron microscopy-SEMPA [6], have been employed in order to visualize magnetic structures of the Py material directly and to allow in-situ measurement of DW structure and dynamics within nanostructured media. A well-known imaging technique is Lorentz microscopy [7] and using this technique, domain/domain wall behaviour can be visualized with high spatial resolution. In the present thesis, patterned Py nanostructures of different geometries are studied by means of Lorentz Transmission Electron Microscopy (LTEM). The aim of the present thesis is to determine how the geometry of a low dimensional structure, *i.e.* nanowire, affects the magnetic behaviour of domain walls. In such structures, edge roughness also greatly impacts DW behaviour, *i.e.* DW formation, transformation and motion [1]. In particular, structural edge roughness induces a DW coercivity when the DW propagates thoroughly the patterned nanostructures. In the present thesis, the edge roughness effect is quantified via a study of DW transformation. Magnetic

simulations were also used to simulate similar structures in order to assist interpretation of experimental results.

The present thesis is structured as follows. This chapter will cover the fundamental concepts of magnetism in ferromagnetic nanostructures that relate to Py nanowires in particular. Magnetic energy terms relevant to ferromagnetic nanostructures are discussed as they are essential to an understanding of simulation results, where the potential energy landscape of a nanostructure is related to these energy terms. Characterization techniques including LTEM and sample fabrication will be described in the second chapter. The third chapter details typical types of domain walls in the static state and their phase diagrams and will show results of a correlation between DW transformation and effects of edge roughness in nanowires. Finally, conclusions and further research plans will be given in chapter 4.

1.1. CLASSIFICATIONS OF MAGNETIC MATERIALS

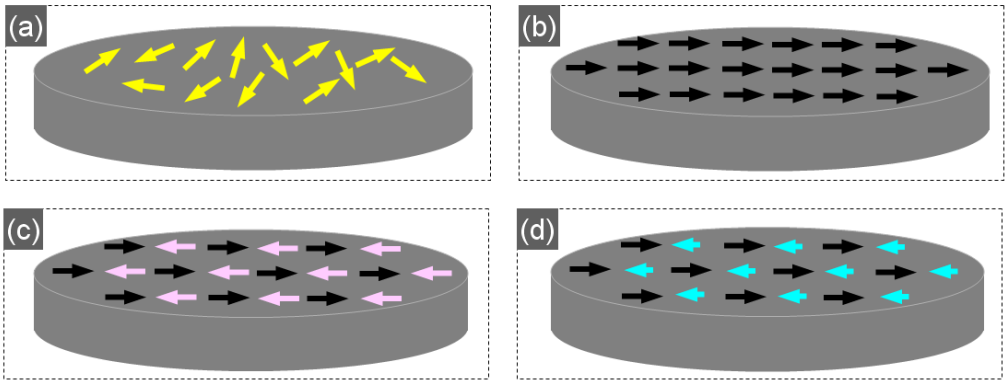

Fig. 1.2 A schematic of selected classifications of magnetic materials: (a) paramagnetic, (b) ferromagnetic, (c) anti-ferromagnetic and (d) ferrimagnetic phases. Arrows indicate the directions of individual spins and are colored to accentuate particular spin orientations.

The properties of magnetic materials ultimately derive from the magnetic moments of their constituent atoms. In principle, the magnetic moment of an atom is produced by the spin and orbital angular momenta of its electrons. The permanent motion of the bound electrons can be considered as a current loop with an associated magnetic moment, in accordance with Ampère's theory of elementary molecular current [8]. The sum of magnetic moment vectors of the whole material volume is typically defined as the total moment vector per material volume, V, which is more usefully described as the magnetization ($\boldsymbol{M}$).

Moreover, a dimensionless proportionality constant that indicates the degree of magnetization of a material in response to an applied magnetic field (***H***) is defined by the relationship, ***M***/***H***, and named the susceptibility, χ, of a material. The net magnetization of an arbitrary material depends on the specifics of the electron configuration and the structural arrangement of its atoms, which gives rise to classes of magnetic material. Some classes (or phases) of magnetic materials are selected and presented in Fig. 1.2.

The first class of magnetic behaviour, encompassing the major five of natural materials, is diamagnetism (DM). In this class, all the electrons are paired with opposite spin, so that the resulting magnetic component is cancelled in the absence of an external magnetic field and this material has negative susceptibility [8]. However, the atomic orbitals are filled according to the Pauli principle [8, 9], some materials have unpaired electrons because of competitions in energy at outer levels (*d* or *f*-orbital). Consequently the magnetic moment components of these electrons are uncompensated, resulting in the second class, paramagnetic (PM), which has positive susceptibility [9] and the magnetic moments associated with the unpaired electron spins are randomly oriented throughout the PM materials, as illustrated in Fig. 1.2(a). In contrast to PM materials, in other classes of ordered magnetic materials the magnetic moments or spins are aligned in particular directions, as shown in Fig. 1.2(b-c). For example, the third class of magnetic materials is ferromagnetism (FM), where neighboring spins are aligned parallel to one another in the absence of an external field (Fig. 1.2(b) due to ordering, thus a spontaneous total magnetic moment for the whole system can exist. In FM materials, the relationship between ***M*** and ***H*** is generally not linear, so a more general definition of differential susceptibility is commonly used, $\chi=\partial \boldsymbol{M}/\partial \boldsymbol{H}$. Nonlinear effects depend on domain configuration of the material when the material's magnetization is not saturated. Those properties are related to many of potential applications and thus FM materials are of great interest [3-6]. In fact, ferromagnetic behavior is found in transition metals (Co, Fe, Ni) and rare earth (La, Gd, Tb,…) elements, but also exists in alloys, oxides, other combinations of these (CoFe, FeNi,…) [1, 2, 8, 9]. In addition to ferromagnetism, another ordered magnetic material type is anti-ferromagnetism, AFM. Neighbouring spins existing in this type of material are arranged anti-parallel, as shown in Fig. 1.2(c). At zero-applied field, the magnetic moment

of the whole AFM system is zero since the moments of the two magnetic sub-lattices are equal but opposite. A fifth class of magnetic materials, as ferrimagnetic, has an electron spin configuration similar to AFM materials, except that the magnetization of adjacent magnetic sub-lattices is not completely balanced and a spontaneous magnetization remains (Fig. 1.2(d)). Thus, ferrimagnetic materials have a net magnetic moment but the total magnetization is weaker than that of most ferromagnetic materials. More complex behaviour is also possible. For instance, perovskites are compounds with the form $A_{1-x}B_xMnO_3$, where A = La, Pr, Nd or Sm and B = Ca, Sr or Ba [9] and can have multiple magnetic phases as a function of temperature (T). In order to distinguish between the phases in complex magnetic materials, an M-T or χ-T relationship is often measured. From the measured M-T or χ-T curves, the transition (critical) temperatures corresponding to phase transitions between FM/AFM and FM/PM can be observed. The critical temperatures of the AFM/PM and FM/PM transitions are called the Néel (T_N) and Curie (T_C) temperatures, respectively, above the Curie temperature, the magnetic ordering is destroyed.

Of the classifications given above, ferromagnetism is the most relevant to the present work. In particular, Py has a ferromagnetic phase at room temperature with $T_C \approx 800$K. In the following sections, the main characteristics of ferromagnetic materials are explained in detail.

1.2. FERROMAGNETIC PHASE

In 1907, Weiss [8] introduced the concept of an internal molecular field, a spontaneous field existing in ferromagnetic materials below the Curie temperature, to explain the magnetic behavior of the FM materials. The molecular field or internal field ($\boldsymbol{H}_{inter}$) can be expressed as

$$\boldsymbol{H}_{inter} = \gamma \boldsymbol{M} \qquad (1.1)$$

where γ is the dimensionless Weiss coefficient and has a value of order 10^4. A disadvantage of Weiss' concept is that it did not explain the origin of the field, which is too large to be realistic. For instance, a typical ferromagnetic material has a molecular field that is calculated to be the order of 10^3 T, which is much stronger than usual laboratory magnetic fields which are generally (<1T). In this case, it is clear that the external field would be

insignificant in comparison to the internal field, indicating that the external field should have little influence on the system, contrary to the known behaviour of magnets. Later, Heisenberg [8] identified the nature of the molecular field as a consequence of the quantum-mechanical exchange interaction, which is related to the overlap of the charge distributions of the atoms existing in a FM material. The overlap of the electron wave functions leads to the appearance of an inter-atomic exchange integral. Simply, if the exchange integral (J) between electrons on adjacent atoms is positive, then the spins on neighbouring atoms would align parallel to minimize the total energy and thereby give rise to FM behaviour. Heisenberg's proposal can be written by the Heisenberg Hamiltonian,

$$H_{ij} = \sum_{i,j} -2J\boldsymbol{S}_i\boldsymbol{S}_j, \tag{1.2}$$

where H_{ij} is the exchange energy. $\boldsymbol{S}_i$ and $\boldsymbol{S}_j$ are the spins on atoms i and j, respectively. J is the exchange integral: if $J<0$ then $H_{ij}<0$ when $\boldsymbol{S}_i$ and $\boldsymbol{S}_j$ are anti-parallel and the material exhibits AFM behaviour, while if $J>0$ then $H_{ij}<0$ when $\boldsymbol{S}_i$ and $\boldsymbol{S}_j$ are parallel and the material is ferromagnetic. This concept also indicates that the exchange integral depends sensitively on the degree of overlap between the orbitals on adjacent atoms. Even though many reliable calculations of the quantities were involved in the Heisenberg's proposal [1, 8-13], equation (1.2) is a convenient empirical description of the exchange energy in which the exchange integral is determined from experiment. Understanding the magnetic behaviour of a FM system is essential in which a number of competing contributions to the total magnetic energy of the system must be considered and will be described in the following section.

1.3. MAGNETIC ENERGY

The total magnetic energy, E_{tot}, of a FM system is expressed as a sum of distinct contributions,

$$E_{tot} = E_{ex} + E_{Zeeman} + E_{\lambda} + E_k + E_d \tag{1.3}$$

As explored below, $E_{ex.}$, E_{Zeeman}, E_{λ}, E_k and E_d are the exchange energy, Zeeman energy, magnetostriction energy, anisotropy energy and magnetostatic energy, respectively. Briefly, the E_{ex} term represents the exchange interaction or Heisenberg interaction among neighbouring spins. The E_{Zeeman} term describes the interaction between a material's magnetization and an external field. E_{λ} accounts for changes in the physical dimensions of a

system under the influence of an applied magnetic field. The anisotropy energy, E_k, is due to intrinsic and extrinsic properties of the system, *i.e.*, lattice structure (magnetocrystalline anisotropy) and specimen geometry (shape anisotropy), respectively, which may give rise to 'preferred' directions of magnetization. Finally, E_d, the demagnetization energy arises from both volume and surface magnetic charges of the system. Most magnetic behaviour can be understood in terms of a competition between these individual terms and E_{tot} is always to be minimized at least locally in a magnetic system to produce stable magnetic states [10]. For instance, the magnetostriction energy is negligible in permalloy due to its material properties.

1.3.1. Exchange Energy

As mentioned in section 1.2, Heisenberg proposed that the ordering of a magnetic system can be considered to arise from interactions between neighbouring spins. This interaction is called the isotropic Heisenberg interaction because it is independent of the change on the magnetization direction. Implicit in the use of the exchange interaction is that the interaction strength decreases rapidly with increasing distance between atoms. If taking into account spins of the system for long-range-order, the total exchange energy, E_{ex} of the system can be written as,

$$E_{ex} = -\sum_{i,j}^{all-space} 2J_{ij}\boldsymbol{S}_i\boldsymbol{S}_j \qquad (1.4)$$

If considering short range order only (i.e., extending the summation only to nearest neighbours, *nn*), equation (1.4) could be simplified by assuming a single-valued exchange parameter, J,

$$E_{ex} = -2JS^2\sum_{i,j}^{nn}\cos\phi_{ij}, \qquad (1.5)$$

where S is the magnitude of the spin vector and ϕ_{ij} is the angle between the i^{th} and j^{th} spins. If $J>0$, then parallel spins correspond to the lowest energy state ($S_i\uparrow\uparrow S_j$), *i.e.* FM.

1.3.2. Zeeman Energy

The effect of an external field ($\boldsymbol{H}_{ext.}$) on a magnetic system with magnetization $\boldsymbol{M}$ is described by an interaction energy, known as the Zeeman energy. Without considering other factors, the influence of $\boldsymbol{H}_{ext}$ on the magnetization of a magnetic material is to attempt to

align the magnetization parallel to the field direction in order to minimize energy. The Zeeman energy, E_{Zeeman}, is described as

$$E_{Zeeman} = -\mu_0 M_S \iiint_V (\boldsymbol{H}_{ext.} \bullet \boldsymbol{n}) dV, \tag{1.6}$$

where, μ_0 is the permeability of free space, $\boldsymbol{n}$ is the unit vector along the direction of magnetization and the energy is integrated over the whole specimen with volume element, dV. Equation (1.6) means that the magnetization tends to rotate and orient to the direction of the external field and this can be used to alter the direction of magnetization as desired. However, competition between external field contribution and self-field contributions (*e.g.*, stray field, demagnetization field as described in section 1.3.4) leads to complicated behaviour.

1.3.3. Magnetostriction Energy

When applying an external field to a ferromagnetic material, in addition to a change in magnetization, a change in physical dimensions can often be observed. This effect is known as magnetostriction where atomic moments are induced by a force under the external field onto the magnetic dipole. By means of this, the electron orbital and spin configuration are distorted under the external field, resulting in mechanical strain. The magnetostriction parameter, λ, is defined as the fractional change in length of the material, $\lambda = \Delta l/l$. λ is maximized when the magnetization in the sample is maximum ($\boldsymbol{M}_S$): this value is the saturation magnetostriction, λ_S. In an applied magnetic field, the direction of λ_S is along the direction of the applied field. The magnetostriction in a magnetic material has an associated energy, E_λ, that is related to the fractional change in length due to the magnetostriction of the material. This effect is significant in some other materials (bulks or thin films), but for the nanostructures studied in the thesis it is negligible (*i.e.* the magnetostriction coefficient of Py is of order 10^{-6} [8, 9]) and will not be discussed further.

1.3.4. Magnetostatic Energy

When a magnetic specimen is uniformly magnetized by an external field, north and south magnetic poles develop at the surface of the material which can be represented as positive (+) and negative (-) magnetic charges, respectively. That are located at the regions

where magnetization is discontinuous or divergent. These magnetic charges produce both external and internal fields. As an example, a thin FM rod uniformly magnetized along its axis is illustrated in Fig. 1.3(a).

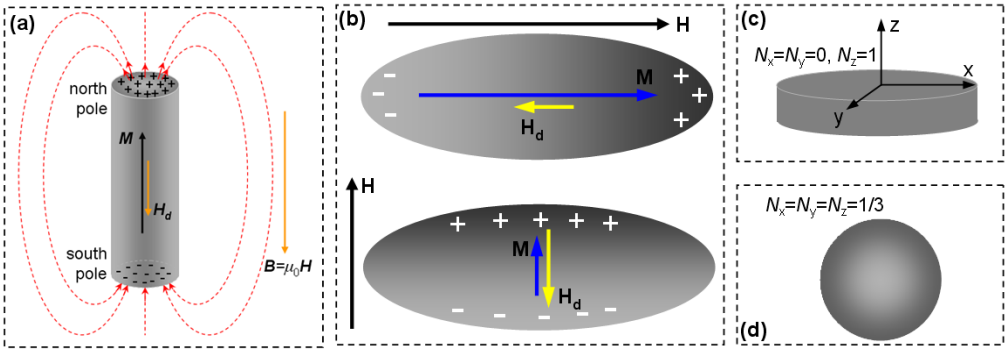

Fig. 1.3 (a) A schematic of a thin FM rod with magnetic poles, analogous to magnetic charges. The magnetic field is represented by lines of flux and the strength of the field is proportional to the density of lines per unit area. (b)-(d) The shape anisotropy energy is affected by specimen geometries and is dependent on the size of the demagnetization fields: (b) an anisotropic ellipsoid which was magnetized along long (upper) and short (lower) axes; (c) and (d) demagnetization factors of a 2D disk and a 3D sphere.

The external field is referred to as the 'stray field' and the internal field is known as the demagnetizing field, $\boldsymbol{H}_{\mathrm{d}}$, which opposes the magnetization. The magnetostatic field arises from both surface and volume charges and this is connected with the magnetic field generated by the magnetic body itself. In general, the stray field at position $\boldsymbol{r}$ (field point) is given by an integration over position $\boldsymbol{r}$' (source) and is expressed as

$$\boldsymbol{H}_d(r) = -\frac{1}{4\pi}\iiint_V \frac{\nabla \bullet \boldsymbol{M}}{|\boldsymbol{r}-\boldsymbol{r}'|^2} dV + \frac{1}{4\pi}\iint_S \frac{\boldsymbol{M}\bullet\boldsymbol{n}}{|\boldsymbol{r}-\boldsymbol{r}'|^2} dS, \qquad (1.7)$$

where $\boldsymbol{n}$ is the outward directed surface normal, perpendicular to the differential boundary surface unit; $\boldsymbol{r}$' and $\boldsymbol{r}$ are the position vectors of the charge source and evaluation point, respectively. The first and second terms of equation (1.7) extend over the sample volume (V) and its surface (S), respectively. The magnetic energy arises from the interaction between the field and the magnetization which it opposes and is given by

$$E_d = -\frac{\mu_0}{2}\iiint \boldsymbol{M}\bullet\boldsymbol{H}_d dV. \qquad (1.8)$$

E_{d} can be minimized by reducing the amount of magnetic charge that builds up in the volume of the material. For a body with an arbitrary shape, the demagnetization field is not

uniform and relates to the magnetization by the demagnetizing factor tensor, $\tilde{N}$, through $\boldsymbol{H}_d=-\tilde{N}\bullet\boldsymbol{M}=-N_aM_x\boldsymbol{i}-N_bM_y\boldsymbol{j}-N_cM_z\boldsymbol{k}$, where ($N_a+N_b+N_c=1$) [8, 10]. $\tilde{N}$ can be calculated for samples of a given geometry, however, for the simple sample geometry of the ellipsoid, H_d is constant.

1.3.5. Anisotropy Energy

Figs. 1.3(b-d) show examples of the dependence of specimen geometries for an ellipsoid, a 2D disk and a 3D sphere, respectively where they are referred to shape anisotropy. Fig. 1.3(b) shows an ellipsoid with shape anisotropy with the magnetization along the long (top panel) and short (bottom panel) axes. It can be seen that free poles are separated by relatively long and short distances, respectively. The external field required to magnetize the material along the long axis is lower than that in the short axis because the magnetostatic energy due to the magnetic charges in the short axis is larger than that in the long axis, as indicated by (+) and (-) charges in Fig. 1.3(b). The shape anisotropy energy of this element can be expressed as the following,

$$E_K=-\iiint_V K_{eff}\sin^2\theta dV, \tag{1.9a}$$

where K_{eff} can be written as,

$$K_{eff}=\frac{1}{2}\mu_0(N_b-N_a)M_S^2. \tag{1.9b}$$

Here, K_{eff} is the effective anisotropy constant and is directly related to the shape/geometry of the specimen. θ is the angle between the long axis of the specimen and the magnetization direction. M_S is the saturation magnetization and N_a and $N_b=N_c$ are known as the demagnetization factors along the long and short axes, respectively. In particular specimen geometries, the demagnetization factors can be simplified, *e.g.* demagnetization factors of a 2D disk and a 3D sphere are relatively simple, as shown in Figs. 1.3(c) and (d), respectively.

As already mentioned the specimen geometries affect the total magnetic energy of the magnetic system, through an energetic term known as the shape anisotropy energy. Another contribution to the anisotropy energy is introduced here which depends on the direction of magnetization relative to the structural axes of the material. This contribution is related to crystalline structure of magnetic materials, the magneto-crystalline anisotropy. Magneto-

crystalline anisotropy is associated with the orientation of magnetic moments with respect to the crystal lattice. It depends on the magnetic order of the material and is determined by the lattice structure- the lattice spacing and chemical bonding of the material, in which the degree of electronic orbital overlap and/or interaction. In a particular material, the orbitals are oriented along certain crystallographic directions, which determine the preferred directions (easy directions or easy axes) where the energy is minimized, and hard directions or hard axes where it is more difficult to align the magnetization. To rotate the magnetization off the easy direction this requires higher energy and can occur under the application of an external field. This is expressed below for a particular lattice structure, the anisotropy energy for a hexagonal lattice structure can be written as

$$E_K = \iiint_V \left(K_1 \sin^2\theta + K_2 \sin^4\theta\right) dV, \qquad (1.10)$$

where, θ is the angle between the anisotropy axis and magnetization direction, V is the volume of material and K_1 and K_2 are the anisotropy constants for the materials. The values of K_1 and K_2 will indicate the easy and hard axes of the system. If K_1 is large and positive, then the easy axis is the anisotropy axis and if K_1 is large and negative, then the easy axis is perpendicular to the anisotropy axis (uniaxial anisotropy). Otherwise, if K_1/K_2 values are in range of -2 to 0, the easy directions lie on a cone (an easy cone) with the angle β relative to the axis (crystal axis or *c*-direction) given by an relation, $\sin(2\beta) = -\frac{1}{2}K_1/K_2$ [8, 9]. In practice, the magneto-crystalline anisotropy could be induced via special processing conditions, for example, if a specimen is fabricated or annealed in a large external field. This effect is often used during the deposition of multilayer devices where magnetic order is initially defined by an external field and annealing conditions induce an anisotropy because the magneto-crystalline anisotropy parameters have strong dependence on temperature. In the case of the soft magnetic material, Py presented in this work, the material has a polycrystalline structure. The uniaxial K of Py is low therefore this is not a major factor. However, the shape anisotropy is an important and dominant factor in our patterned constrained nanostructures as will be explored in detail in chapter 3.

1.4. MICROMAGNETIC SIMULATION

To assist interpretation of experimental results, artificial nanostructures with different

widths, thicknesses and geometries were designed and simulated using the Micromagnetic Framework (OOMMF) package [11]. The simulation provides useful information on the magnetic behaviour of domain walls through the various energy terms for a particular structure. The advantage of this is that it allows us to quickly visualize various configurations. In particular, OOMMF uses the Landau-Lifshitz-Gilbert equations for the precession and damping of magnetization under a magnetic field [12, 13], which are described as follows.

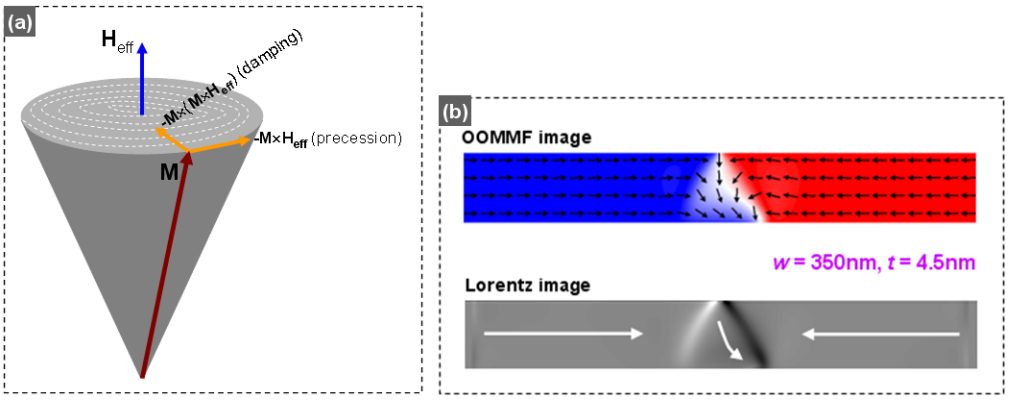

Fig. 1.4 (a) Precession processes of the magnetization, $\boldsymbol{M}$ around the effective field, $\boldsymbol{H}_{\text{eff}}$ with damping and (b) an OOMMF image of a transverse domain wall (TDW) which was simulated in 4.5 nm-thick nanowire with dimension of 350nm×2500nm.

The precession dynamics of magnetization vector in an external field, as shown in Fig. 1.3(a), can be written as,

$$\frac{d\boldsymbol{M}}{dt} = -\gamma_0 (\boldsymbol{M} \times \boldsymbol{H}_{eff.}), \tag{1.11}$$

where t is the time, γ_0 is the gyromagnetic ratio and $\boldsymbol{H}_{\text{eff}}$. is an effective field that relates to the total energy, $E_{\text{tot.}}$, of a system of volume V via the following equation:

$$\boldsymbol{H}_{eff.} = -\frac{1}{\mu_0 V}\frac{\partial E_{tot.}}{\partial \boldsymbol{M}} \tag{1.12}$$

In practice, equation (1.12) describes continuous precession and does not account for dissipation, where the dissipation acts to diminish the precession, returning the magnetization vector towards $\boldsymbol{H}_{\text{eff}}$. So, adding a dissipation term into the equation (1.11) gives the Landaul-Lifshitz (LL) equation,

$$\frac{d\boldsymbol{M}}{dt} = -\gamma\left(\boldsymbol{M} \times \boldsymbol{H}_{eff.}\right) - \frac{\gamma\alpha}{M_S}\boldsymbol{M} \times \left(\boldsymbol{M} \times \boldsymbol{H}_{eff.}\right) \quad (1.13)$$

Here, the second term is referred to as the LL damping term and includes a material-specific constant, α, that is known as the damping coefficient. In a simulation, the equation (1.13) is re-evaluated for each spin-spin interaction until an equilibrium (either stable or metastable), is reached. An equilibrium state may be reached by a limit of on the number of iterations or simulation time in which a minimum value of the torque dM/dt was typically set to 10^{-5} A/m•s. The process of finding the equilibrium state is repeated at each step of increasing the applied field. In a real structure, it would include all atoms in the system for the simulation, however this is not achievable due to the limit of the computing power and time. The OOMMF software operates by dividing the magnetic system into a set of discrete cells, where each cell of the mesh is considered as single unit of spin with magnetic moment, $\boldsymbol{m}_i$. Here the cell-size is an important parameter which strongly affects the outcome of the simulation. Typically, a cell-size is chosen close to the characteristic exchange length in order to get realistic results. Most of the simulations in this thesis were using a cell-size of 4 nm, which is comparable to the magnetostatic exchange length ($l_{ex}=(2A/\mu_0 M_S^2)^{½}$) [8-10,12] for permalloy (5.3 nm), where A is the *exchange stiffness* (discussed later). Another factor that should be considered is that the cells used in simulations for perfect structures with straight edges and uniform thickness. In fact, experimental structures contain a degree of roughness due to limitations of the fabrication process, which will be discussed in chapter 3. Other factors were chosen as the standard material parameters for permalloy, such as $M_S=860\times10^3$A/m, $A=13\times10^{-12}$ J/m. Regarding the damping parameter, α, becomes important when the magnetization dynamics are to be evaluated. Many people have studied the damping parameter as a function of relaxation time [14]. Experimentally, the damping parameter can be estimated, *e.g.* by ferromagnetic resonance measurements [15], time resolved measurements [16], or electrical measurements [17]. It is material specific [15] and has been measured for Permalloy, yielding estimates between 0.013 and 0.03 [18, 19]. In some cases, when the static magnetic configuration is sought, the choice of α does not noticeably influence the result. A higher α (α = 0.5) was used in this work and an example result is shown in the upper panel of Fig. 1.4(b) where the above parameters were used to

simulate a TDW in 4.5nm-thick nanowire with dimension of 350nm×2500nm. The calculated Lorentz image is shown in the lower panel. Details of magnetic domains and Lorentz image interpretation are to be described in the next section and chapter 3, respectively.

1.5. THE DOMAIN STRUCTURE OF FERROMAGNETS

1.5.1 Magnetic Domains

As discussed in section 1.2, FM materials are characterized by a distribution of spins which are aligned parallel to one other to produce a net magnetic moment. However, the balance of energetic terms indicated in equation (1.3) often leads to more complex spin configuration that depend on the shape of the material, its crystallinity, the presence of structural or chemical defects and the existence of an external magnetic field. Landau and Lifshitz showed that domain structure is a natural consequence of the minimizing the total energy [8, 10] or ferromagnetic materials can lower their total energy from a uniformly magnetized state by spontaneously breaking up their magnetization into domains. Here, the total energy of a particular magnetic system can be reduced by removing the surface charge and therefore lowering the magnetostatic energy. Thus, domain formation can reduce stray fields by providing regions of opposing magnetization where individual components of stray field (as already described in Fig. 1.3(a)) cancel each other. For example, some possible domain configurations in a thin Py rectangular element are illustrated in Fig. 1.5.

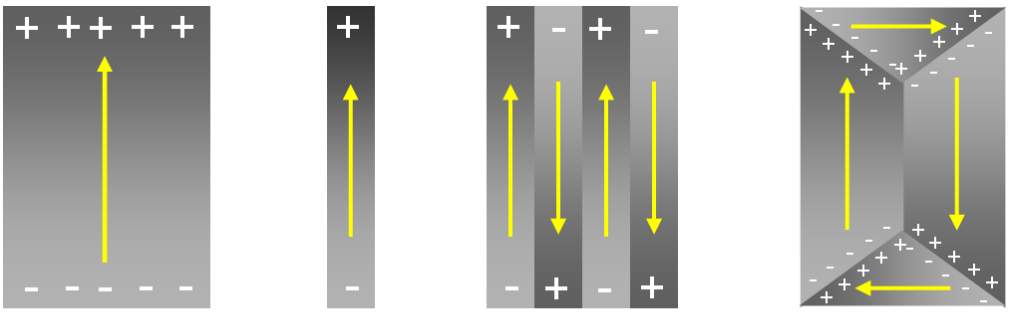

Fig. 1.5 Possible domain configurations in a thin NiFe rectangular element: (a) a single domain, (b) a single domain in a nanowire with strong shape anisotropy, (c) multi-domain and (d) flux closure domains.

Here, those configurations arise from the interplay between energy contributions. The

simplest configuration is the single domain state, as shown in Fig. 1.5(a), in which the exchange energy is minimized with the parallel alignment of neighboring spins. However, a large amount of surface charge is built up, so a large magneto-static energy is produced. Thus, this configuration is not preferable as ground state, it is only stable under large external magnetic field or if the material has a high uniaxial anisotropy (*e.g.* an elongated magnetic system or nanowire), as shown in Fig. 1.5(b). Without those conditions, the system generally prefers to have uniformly magnetized domains, shown in Fig. 1.5(c). In this case, the exchange energy is significant larger due to the presence of anti-parallel domains, and the surface charge distribution is reduced. This state is also not preferable, but it is when there is a high uniaxial anisotropy parallel to the long axis of the element. Otherwise, if the system has a small uniaxial anisotropy (for example, if the width of the element is comparable to the length, similar to cubic anisotropy), then the system tends to form a flux closure state as illustrated in Fig. 1.5(d). Thus, among those states, the state present in Fig. 1.5(b), some surface charge is generated and the magnetostatic energy is minimized and the shape anisotropy dominates, resulting in the magnetization lying parallel to the long axis of the nanostructure (easy-axis). This state has the lowest energy in case of absence external field. So, narrow nanostructures/ nanowires are strongly affected by the shape anisotropy or geometry dependence. Indeed, to understand microscopic properties of domains in a magnetic material, the basic concepts of the domain structure are essentially discussed in the next sub-sections.

1.5.2 Hysteresis loop (M-H curve)

Generally, when applying an external field to a ferromagnetic material, the magnetic moments tend to align parallel to the field in order to minimize their Zeeman energy. When all magnetic moments are aligned with the external field, the maximum magnetization of the whole sample is observed, called the saturation state, $\boldsymbol{M}_S$. If the external field is then removed, in FM materials the total magnetization may not vanish, but remains at a finite remanent magnetization, $\boldsymbol{M}_r$. The applied field then required to reduce $\boldsymbol{M}$ to zero is called the coercive field, H_C. The system can then be saturated in the opposite direction if the reverse field is increased. This process can be explained in terms of domain rotations and displacements. The relationship between $\boldsymbol{M}$ and $\boldsymbol{H}$ is normally plotted as $\boldsymbol{M}$ vs $\boldsymbol{H}$ which

depends on the direction of ***M*** (history), a so-called hysteresis loop. [8, 10, 20-22] Typical hysteresis loops are shown in Fig. 1.6 and reveal two general trends that are used to distinguish ferromagnetic materials as either 'soft' or 'hard' ferromagnetic materials. If both values of H_C and M_r are large, magnetic materials are 'hard' ferromagnets, whereas if magnetic materials have small values of H_C and M_r, then they are 'soft' ferromagnets. For instance, permanent magnets such as NdFeB alloy with a corecivity of 1T are classed as hard magnetic material whilst permalloy has a coercivity of 0.04mT and is classed as soft magnetic material [8-10].

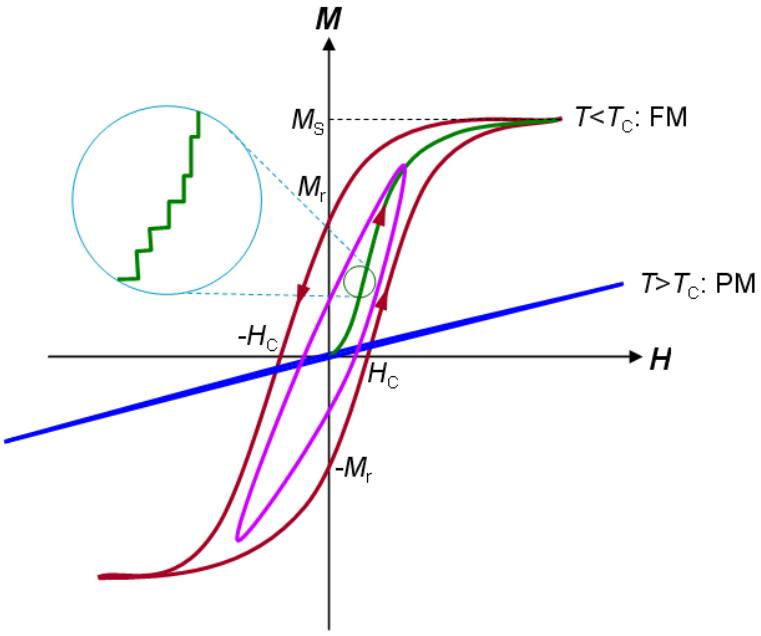

Fig. 1.6 Major and minor *M-H* curves of a magnetic material in temperature lower than the Curie point (red and violet curves, respectively) and higher than the T_C (blue line). An inset presents Barkhausen steps.

As shown in Fig. 1.6, the hysteresis loop can be separated to several stages. In the first stage of the magnetization process at a specific temperature far below the T_C (the green solid line), *M* is zero in the as-grown state and magnetic moments are basically oriented by an external applied magnetic field on a microscopic scale. This process may be reversible for very small incremental changes in the external field, but looking at the whole process, the local magnetization in each domain is rotated and propagated under the magnetic field. The incremental grain-by-grain flipping/ rotation of local magnetization causes sudden jumps in the net magnetization; this process is known as domain wall jumps or the

Barkhausen effect. The effect is dominant in bulk and large thin film ferromagnetic materials because a number of intrinsic and extrinsic parameters are contributed dominantly to the effect. Furthermore, when the saturation state is reached and the external field is turned off, subsequently the magnetization decreases and does not go back to the stage as it was increased, *i.e.* the process indicated by the green-solid-line is never repeated. The magnetization is retained at the M_r value. The type of the hysteresis loop is shown in Fig. 1.6 (red curve) is a major loop, and minor loops can be generated in lower field values, *i.e.*, violet-curve in Fig.1.6. Similarly, at temperatures higher than the Curie temperature (PM state) indicating that *M-H* relationship is a linear dependence, shown as a blue line in Fig. 1.6. Thus, a method to recognize the phase transition between ferromagnetic and paramagnetic phases in a magnetic material with multiple phases is to measure *M-H* curves at specific temperatures: if the *M-H* curve is nonlinear, then the material is in a FM phase, whereas if the *M-H* curve is linear, the material is in a PM phase [8, 9].

1.5.3 Microscopic Magnetization Reversal

When an external magnetic field is applied to a magnetic system, the magnetization can respond in different ways. Reversal of magnetization occurs by either coherent or incoherent processes [1, 8, 9, 10], as illustrated in Figs. 1.7(a) and (b). The reversal of magnetic moments under the applied magnetic field may occur by coherent rotation, where entire magnetic moments rotate like one big spin, or incoherent reversal where magnetic moments change locally. This process is also possible by the nucleation and annihilation of domain walls. The coherent rotation of magnetization was first proposed by Stoner and Wohlfarth [23] and can be described by considering small single domain particles with uniaxial anisotropy, where creation of domain walls would need more energy rather than spin rotation. It could also be applied to small elements with dimensions of only a hundred (or less) nanometers. For instance, coherent rotation of magnetization in a prolate spheroid ferromagnetic particle is shown in Fig. 1.7(a). As an external field is applied perpendicular to the anisotropy axis, the magnetization smoothly rotates and aligns to the external field. The magnetization direction of the specimen is changed completely and reversal is occurred. The system is saturated when an applied external magnetic field strength is equal to anisotropy field, $H=2\mu_0 K_U/M_S=H_K$. Incoherent rotation of magnetization also occurs in

larger specimens or materials with complex geometries but the reversal processes are more complicated and may occur by nucleation, movement and annihilation of domain walls, as illustrated in Fig. 1.7(b).

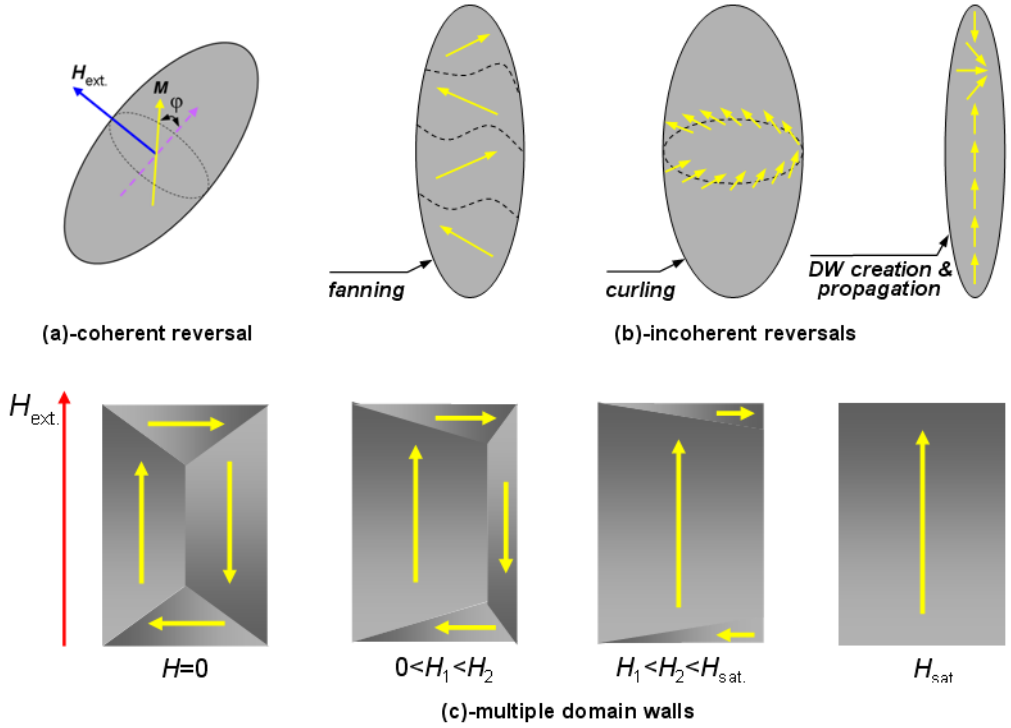

Fig. 1.7 (a) Schematic of a prolate spheroid ferromagnetic particle where coherent rotation of magnetization acts as the magnetization reversal processes, (b) common incoherent reversal models of prolate spheroid ferromagnetic particles in different shape in which domain walls were created and respond in different manners (fanning, curling and DW propagation) under an applied magnetic field, and (c) multiple domain walls existing in a rectangular-shape ferromagnetic film under a magnetic field applied parallel to the long axis of the specimen where magnetization process can be separated into 4 stages which relate to the field strengths.

Here, incoherent reversal can occur in prolate spheroid ferromagnetic particles, Fig. 1.7(b). In the presence of an external field, the magnetization can be split up into many domains with zigzag behaviour (fanning case) or spins are curled on the hard axis plane of the particle (curling case) and/or a DW wall is created and then propagates through the particle. Incoherent reversal also depends on the size, shape and material properties (*e.g.* crystalline character). Indeed, controlling the structural geometry of a specimen is an important parameter to understand reversal processes of magnetization under an external

field. However, further details of the coherent and incoherent processes will not discussed much in the thesis. Another simple example is reproduced from Fig. 1.5(d), where a system has flux closure state (multiple domain walls) and it is under an external field, as illustrated in Fig. 1.7(c). If the external field is applied parallel to the long axis of the structure, then the domain with magnetization aligned parallel to the field becomes larger and the anti-parallel domain becomes smaller. Here, one can distinguish the reversal process via four stages. In the case of no applied magnetic field (H=0), the system is in a flux-closure configuration. Increasing in the external field strength ($0<H_1<H_2$), the magnetic system becomes asymmetric with the left domain (parallel to the field) increasing at the expense of the right domain. Further increases in the applied field ($H_1<H_2<H_{sat}$ where H_{sat} is defined as an external field required to saturate the system), lead to annihilation of the smaller domain. In this range, if the external field is turned off, the system can be returned to the initial state (H=0), *i.e.* this is a reversible process. Finally, if the external field is big enough, all magnetic moments/spins within the structure align parallel to the field and the system is then saturated with a homogeneous magnetization and all domain walls are annihilated. In this case, even if the field is turned off, the original structure may not form or not return via the same path, the homogeneous magnetization state can be retained and the process is irreversible.

1.5.4 Magnetic Domain Walls

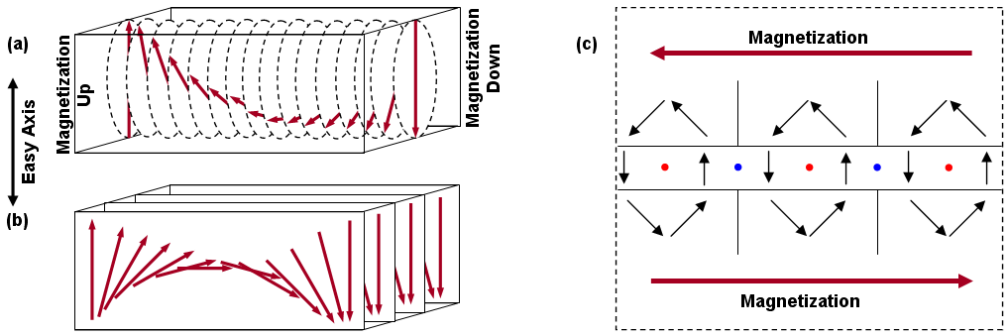

Fig. 1.8 Schematic of typical types of domain walls: (a) Bloch wall, (b) Néel wall and (c) cross-ties wall.

As mentioned above, domains and domain walls are important considerations within magnetic materials during the magnetization processes. The domain walls that form in a specimen depend on the specimen geometry. In systems with restricted geometry, such as a

nanowire of width and thickness much less than the nanowire length and/or thin films, two fundamental types of domain walls form and are classed as either Bloch or Néel walls. When domains walls are formed, it is unfavourable for the magnetizations to change very sharply because of the increased exchange energy. As a result, the local magnetization spreads out over some distance or a characteristic length, called the domain wall width, δ_{DW}. The domain wall width is generally several tens of nanometers [8, 10, 20]. For instance, in the case of a thick film of FM material (> 90nm) where the magnetization on either sides of the domain wall prefer align anti-parallel (180°-wall), spins are gradually rotated in planes parallel to both magnetization planes and the spin rotation occurs along a helical path, as illustrated in Fig.1.8(a). This is known as Bloch type domain wall or Bloch wall. One can see that a Bloch wall generates magnetic charges at the surfaces of magnetization plane which results in the stray field [24], however for a bulk material this is negligible although is divergence free in the volume. If the thickness of the specimen is reduced, *i.e.* lower than 30 nm for Py [10, 21, 22], the magnetic moments are constrained due to the shape anisotropy and rotated in the plane which consists of both magnetizations, as shown in Fig.1.8(b). This is known as a Néel type domain wall or Néel wall [8, 10, 20-22]. In Néel walls, magnetic charges form at either side of the wall and the stray field is confined within the thin film. Moreover, in the case of a specimen that is thicker than 30nm, lower-angle domain wall types can be gained by replacing the 180°-Néel wall with a complicated composite wall, known as a cross-tie wall [8, 10, 25], as shown in Fig. 1.8(c). The cross-tie has Néel section of opposite chirality (sense of rotation of spins within the DW core) separated by Bloch lines. The blue and red solid-circles are known as '*cross-ties'* or *anti-vortices* and '*vortex cores'* of Bloch domain walls, respectively.

To quantify the Bloch wall width, δ_{DW}, the magnetic system is assumed that it has just a competition between exchange interaction and crystalline/shape anisotropy [8, 10, 20]. This competition prefers to align nearest neighbor spins parallel and wants to keep the magnetization oriented only along easy directions. The energy is minimized when neighbouring spins are aligned parallel. Here, assuming that the magnetization rotates within a 180°-wall over N planes of spins (dashed-circles in Fig. 1.8(a)). When the total energy is minimized, the domain wall width can be found,

$$\delta_{DW} = \pi\sqrt{A/K_U}, \qquad (1.14)$$

where, $A=JS^2/a$ is defined as the *exchange stiffness* constant and is temperature dependent, zero-temperature value of exchange stiffness is in relation with the Curie temperature [$A(0)\approx k_B T_C/a$, k_B is the Boltzman's constant], a is the lattice spacing and K_U is the uniaxial anisotropy constant [10, 20, 21].

In general cases, equation (1.14) are able to use to calculate Bloch and Néel domain wall widths,

$$\delta_{Bloch} = \pi\sqrt{A/K_U} \quad \text{and} \quad \delta_{Ne'el} = \sqrt{A/K_D} \qquad (1.15)$$

where, $K_D=\mu_0 M_S^2/2$ is the the stray field energy constant, respectively [8, 10, 20-22].

In the present work, specimens were investigated which have thicknesses are less than 20nm, meaning Néel DWs form exclusively in these films.

1.5.5 DWs in Constrained Nanostructures: Straight & Curved Nanowires

A number of questions are raised regarding how the magnetic behaviour of FM materials change if the specimen dimensions reach, or become comparable to certain characteristic length scales. The main topic of the present thesis focuses on Néel walls in FM nanostructures where the thicknesses and widths are much smaller than the length, *i.e.* nanowires. The main reason for our study is that in soft FM nanostructures it is possible to artificially create, propagate and remove domain walls from the structures by either passing a current or applying a magnetic field. This is an important fact for potential applications such as magnetic memory and logic gates [2, 26]. In such applications, domains/ domain walls can be considered as discrete entities moving in nanowires with different geometries and the domain wall plays an important role in operations of the above devices where it is considered as either 'bit' of information or logical states (opening or closing states in logic gate devices). Thus, it is useful to study domain wall behaviour in the soft FM nanostructures by means of current or field [2-7, 26-29], where DW propagations can be treated as conveyances of information which are driven by either an external magnetic field or an electric current. Each method has advantages and disadvantages in applications. For instance, using magnetic field driven domain wall motion method is an easy way to

characterize architectures, but extrinsic parameters are significantly influenced on the DW propagation process such as Zeeman effects at high applied field. Particularly, when a DW propagates along a nanowire, it must dissipate energy due to Gilbert damping [13]. As a result, the nanowire has to release its Zeeman energy through the DW propagation along the field direction. In other words, the DW propagation speed is proportional to applied magnetic field or the energy dissipation rate. The velocity-field characteristic of a DW has two distinct regimes separated by negative differential mobility in the intermediate field. This is due to the transition from high energy dissipation at low field (uniform motion) to low energy dissipation at high field (precessional motion). In this relationship, the field is larger than the transition point, the so-called Walker breakdown field [20, 27-30]. The Walker breakdown process can be modified by fabricating structures with a certain degree of edge roughness [31], application of an in-plane transverse field [32, 33] or using series of transverse arms patterned at regular intervals along the wire [34]. Even so, this chapter is extensively concerned with DWs in the static state where the DWs were created in different locations of the nanowires in order to understand how structural geometry or edge roughness affects the stable/metastable DW configurations.

The magnetic field-induced domain wall motion was described above is based on the Landau-Lifshitz-Gibert equation [10, 12, 13] and Maxwell's equations [8, 10]. In cases of using current driven domain wall motion method, the magnetization dynamics of spin-polarized current-induced DW motion requires the inclusion of the interaction of the electron charge density and the magnetic moments of magnetic materials in which the torque density of the polarization of the current translates the DW in the direction of electron flow. Thus, by using this method, various specimen properties are manifested such as specimen thickness, grain size and other fabrication dependent parameters. However, this method needs generally complex experimental designs and, when performing experiments of current induced-domain wall motion with high current density, Joule heating can be occurred and subsequently magnetic properties may be influenced or destroyed by such heating [19, 35-37]. Thus, in this work, the field-induced DW experiments were used as simple method for generating DWs in nanowires. Straight and curved-Py-nanowires are extensively considered here with nanowire-thicknesses and widths less than 20 nm and 600

nm, respectively, where the shape anisotropy dominates. The magneto-crystalline anisotropy of Py can be neglected because it is polycrystalline and the magnetization is constrained to align parallel with the long axis of the specimen, *easy-axis* (*i.e.* along the wire) to minimize the magnetostatic energy. Moreover, straight nanowires in simulation are considered as perfect structures without edge roughness, while curved nanowires comprise a degree of edge roughness. However, in experimental structures, the roughness is probably come from both cases.

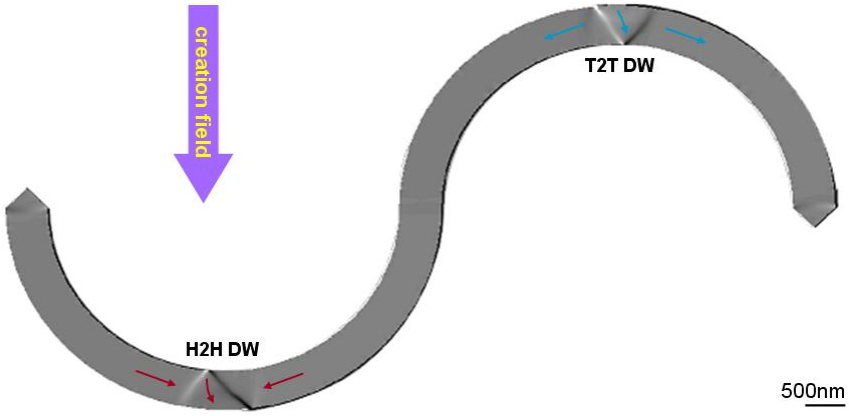

Fig. 1.9 shows H2H and T2T TDWs which were created by an applied field (creation field) perpendicular to the hard axis of a 10nm-thick non-straight/curved nanowire with dimension of 500nm-width×10μm-length.

In a 'non-straight' nanowire, magnetic domain walls may be created if an external field is applied in the hard axis of the structure [5, 6, 26, 34, 38-40], as an example is shown in Fig. 1.9. A number of possibilities occur in each DW creation process and, depending on the orientation of the applied field with respect to the hard axis of the nanowire, two types of wall could be created: either head-to-head (H2H) and tail-to-tail (T2T) domain walls [39, 40], as shown in the curved nanowire (Fig. 1.9) and illustrated in the upper (red) and lower (blue) panels of Figs. 1.10(a-e). Both H2H and T2T DWs have opposing magnetization on either side of the DW. Regardless of whether a H2H or a T2T DW is created in a nanowire, three types of walls can be produced depending on chirality of walls, the thickness and width of the nanowire. These three types are the symmetric transverse domain wall (STDW), the asymmetric transverse domain wall (ATDW) and the vortex domain wall (VDW), shown in Figs. 1.10(a), (b, c) and (d, e), respectively. The STDW and ATDW are simply characterized by symmetrical and asymmetrical triangles, respectively. Whilst the VDW is

configured as outer DWs connected by a diagonal Néel wall and spins circulate around a central vortex core (out of plane), *i.e.* three distinct wall sections in VDWs compared to two wall sections for TDWs. A question raised by these three types of domain walls such as what is the nature of DW configurations, *i.e.* the nature of the asymmetry of ATDWs. For instance, one can be seen in Fig. 1.10(f), if a TDW is virtually divided into two areas, then a correlation between two divided geometrical areas may reflect degree of asymmetry in TDW. Moreover, a correlation between geometrical areas (extrinsic behaviour) and magnetization components (intrinsic behaviour) inside the TDW may also be occurred. This is of interest and will be discussed in detail in chapter 3.

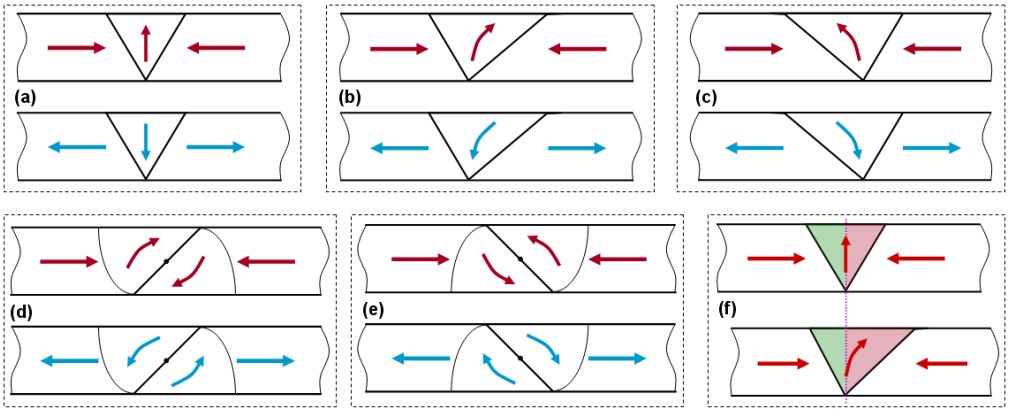

Figs. 1.10 (a-e) show schematics of three types of H2H (upper panels) and T2T (lower panels) domain walls: (a) symmetric, (b) & (c) asymmetric transverse domain wall and (d) & (e) vortex domain walls, respectively. (f) demonstrates a method to distinguish symmetric and asymmetric TDWs where the DW is virtually divided into two areas by a violet line. A correlation between those areas reflect the degree of asymmetry in TDWs (symmetric or asymmetric).

Returning to domain wall configurations, although straight and curved nanowires have been investigated in both simulation and experiment [2-6, 26-30], a full understanding of domain wall behaviour is still lacking, *e.g.* STDW↔ATDW↔VDW transformation mechanism, effects of structural geometries from structure to structure, *etc*. More recently, investigators have been trying to build up a full picture of domain wall behaviour in a particular geometry of structures, *i.e.*, straight, curved nanowires and ring-nanostructures [2-6, 20, 24-26, 30-34, 38-40]. A phase diagram of wall types existing in straight nanowires in different widths and thicknesses has been plotted by Nakatani *et. al.* [30] where the

ground state of the DW type is shown in Fig. 1.11. However, these results are from the straight nanowires. In fact, metastable states could be created in imperfect structures, *i.e.*, curved nanowires, ring-nanowires, due to the edge imperfection. Thus, the situation will be different in structures with different geometries. Furthermore, as mentioned, the qualification of asymmetric TDWs is of interest. Indeed, as shown in Fig. 1.10(f), our suggestion is, as mentioned above, if the TDW is virtually divided by a line starting from an intersection of the walls and perpendicular to the easy-axis, a correlation may exist between the spin configurations of the TDW and the divided areas inside the TDW. Another question to be answered is how structural roughness affects the symmetry/ asymmetry of TDWs. If those questions are answered, ATDW can be quantified directly from observed images experimentally. Those questions will be attempted to be answered in this work by means of a Lorentz TEM study and OOMMF simulations. If the answers of the above questions are realized, it is a useful road map to quantify ATDWs directly, not only for imaging techniques, also for other experimental techniques.

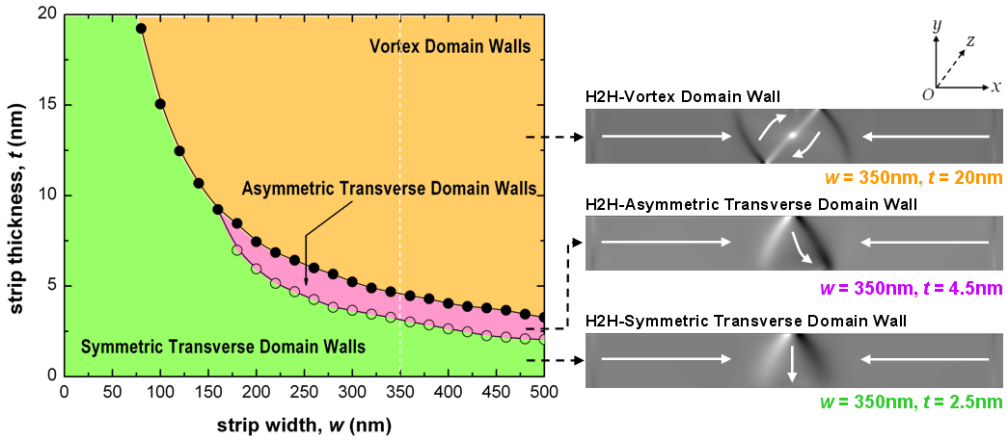

Fig. 1.11 A simulated phase diagram of wall types existing in straight FM nanowires in variations of width and thickness, recited from ref. [30] (left panel). Three types of H2H domain walls are presented in the left panel, vortex DW, asymmetric TDW and symmetric TDW [from top to downward].

Throughout the chapter the fundamental concepts of magnetism in nanostructures were discussed. Further details of magnetic imaging techniques, sample fabrication methods and experimental results, they will be given in the next chapters.

REFERENCES

[1]. J. Stöhr and H.C. Siegmann, *Magnetism: From Fundamentals to Nanoscale Dynamics*, Springer (1st Ed., October 19, 2006)

[2]. S. S. P. Parkin, M. Hayashi, L. Thomas, *Science* **320** (2008) 190 and http://www.nec.co.jp/press/en/0906/1705.html

[3]. R. P. Cowburn, *J. Phys. D: Appl. Phys.* **33** (2000) R1

[4]. M. Hayashi, L. Thomas, C. Rettner, R. Moriya, X. Jiang, S.S.P. Parkin, *Phys. Rev. Lett.* **97** (2006) 207205

[5]. D. Petit, H.T. Zeng, J. Sampaio, E. Lewis, L.O'Brien1, A.V. Jausovec, D. Read, R.P. Cowburn, K.J. O'Shea, S. McVitie, J.N. Chapman, *Appl. Phys. Lett.* **97**(2010) 233102

[6]. M. Kläui, *J. Phys.: Condens. Matter* **20** (2008) 313001

[7]. J.N. Chapman, *J. Phys. D: Appl. Phys.* **17** (1984) 623

[8]. C. Kittel, *Introduction to Solid State Physics* (8th Ed., 2005)

[9]. K.A. Gschneidner, V.K. Pecharsky and A.O. Tsokol, *Rept. Prog. Phys.* **68** (2005) 1479

[10]. A. Hubert and R. Schäfer, *Magnetic Domains*, Springer (1998)

[11]. M. J. Donahue and D. G. Porter, NISTIR 6376, *Tech. Rep., National Institute of Standards and Technology*, Gaithersburg, MD (1999)

[12]. W. F. Brown, *Micromagnetics*, Intersciences (1963)

[13]. T. L. Gilbert, *IEEE Trans. Magn.*, **40** (2004) 3443

[14]. P. Warnicke, Y. Nakatani, S. Kasai and T. Ono, *Phys. Rev. B* **78** (2008) 012413

[15]. N. Inaba, Y. Uesaka, A. Nakamura, M. Futamoto and Y. Sugita, *IEEE Trans. Magn.* **33** (1997) 2989

[16]. I. N. Krivorotov, N. C. Emley, J. C. Sankey, S. I. Kiselev, D. C. Ralph, R.A. Buhrman, *Science* **307** (2005) 228.

[17]. P. M. Braganca, I. N. Krivorotov, O. Ozatay, A. G. F. Garcia, N. C. Emley, J. C. Sankey, D. C. Ralph, R. A. Buhrman, *Appl. Phys. Lett.* **87** (2005) 112507

[18]. G. M. Sandler, H.N. Bertram, T.J. Silva, T.M. Crawford, *J. Appl. Phys*. **85** (1999) 5080

[19]. A. Yamaguchi, S. Nasu, H. Tanigawa, T. Ono, K. Miyake, K. Mibu and T. Shinjo, *Appl. Phys. Lett.* **86** (2005) 012511.

[20]. C. H. Marrows, *Advances in Physics* **54** (2005) 585

[21]. M. Prutton, *Thin Ferromagnetic Films*, Butterworths (1964).

[22]. A. Aharoni, *An Introduction to the Theory of Ferromagnetism*, Oxford University, Press (1996).

[23]. E. C. Stoner and E. P. Wohlfarth, *Phil. Trans. Roy. Soc.* **240** (1948) 599

[24]. J. G. Th. te Lintelo, J. C. Lodder, S. McVitie and J. N. Chapman, *J. Appl. Phys.* **75** (1994) 3002

[25]. M. Herrmann, S. McVitie and J. N. Chapman, *J. Appl. Phys.* **87** (2000) 2994

[26]. D.A. Allwood, G. Xiong, M.D. Cooke, C.C. Faulkner, D. Atkinson, N. Vernier, R.P. Cowburn, *Science* **296** (2002) 2003

[27]. V.V. Volkov and V.A. Bokov, *Domain Wall Dynamics in Ferromagnets*: *Physics of the Solid State* **50** (2008) R199

[28]. A. Thiaville, Y. Nakatani, *Spin Dynamics in Confined Magnetic Structures III*: *Topics Applied Physics* **101** (2006) 161

[29]. J. Miltat, G. Albuquerque and A. Thiaville, *Spin Dynamics in Confined Magnetic Structures I*: *Topics Applied Physics* **83** (2002) 1

[30]. Y. Nakatani, A. Thiaville and J. Militat, *J. Magn. Magn. Mater.* **290** (2004) 750

[31]. Y. Nakatani, A. Thiaville and J. Miltat, *Nature Mater.* **2** (2003) 521

[32]. M. Bryan, T. Schrefl, D. Atkinson, D. A. Allwood, *J. Appl. Phys.* **103** (2008) 073906

[33]. S. Glathe, I. Berkov, T. Mikolajick, R. Mattheis, *Appl. Phys. Lett.* **93** (2008) 162505

[34]. E.R. Lewis, D. Petit, A.V. Jausovec, L. O'Brien, D.E. Read, H.T. Zeng, R.P. Cowburn, *Phys. Rev. Lett.* **102** (2009) 057209

[35]. H. Fangohr, D.S. Chernyshenko, M. Franchin, T. Fischbasher, G. Meier, *Phys. Rev. B* **84** (2001) 054437

[36]. F. Léonard, *Appl. Phys. Lett.* **98** (2011) 103101

[37]. K.J. Kim, J.C.Lee, S.B. Choe, K.H. Shin, *Appl. Phys. Lett.* **92** (2008) 192509

[38]. C.W. Sandweg, N. Wiese, D. McGrouther, S. J. Hermsdoerfer, H. Schultheiss, B. Leven, S. McVitie, B. Hillebrands and J. N. Chapman, *J. Appl. Phys.* **103** (2008) 093906

[39]. K. J. O'Shea, S. McVitie, J. N. Chapman and J.M. R. Weaver, *Appl. Phys. Lett.* **93** (2008) 202505

[40]. C. Brownlie, S. McVitie, J.N. Chapman and C.D.W. Wilkinson, *J. Appl. Phys.* **100** (2006) 033902

Chapter 2

Characterization Techniques and Sample Fabrication

2.1. INTRODUCTION

By using various characterization techniques such as X-ray magnetic circular dichroism (XMCD) [1-5], scanning transmission x-ray microscopy (STXM) [6], magneto-optic Kerr effect (MOKE) magnetometry [7, 8], spin-polarized scanning electron microscopy (spin-SEM or SEMPA) [9, 10] and Lorentz TEM [11], the magnetic properties of ferromagnetic thin films and devices can be visualized quantitatively. Each technique has advantages and disadvantages in exploring the properties of functional materials. In this thesis, the Lorentz TEM (LTEM) technique was used to explore the magnetic behaviour of ferromagnetic nanowires which have potential as future devices [1-11]. Lorentz microscopy is one of the most efficient techniques for the characterization of magnetic materials on the nanoscale and is described in the following sections. The Fresnel mode in particular was used to characterize the domain wall structures in curved Py nanowires, and its interpretation and simulation will be described.

Alongside characterization techniques, sample fabrication methods including thermal evaporation, sputtering deposition and focused-ion-beam (FIB) patterning will be described in this chapter [12, 13].

2.2. TRANSMISSION ELECTRON MICROSCOPY (TEM)

This section describes the fundamental functions of the TEM. In fact, the first electron microscope was built by Max Knoll and Ernst Ruska in 1931 [14] and TEM operation is based on De Broglie's theory of electron wave-particle duality [15]. In a microscope, the electrons are accelerated in a vacuum resulting in a wavelength that is extremely short, around one hundred-thousandth that of visible light. This makes it possible to view objects as on the scale of the diameter of atom. The electron wavelength, λ, can be expressed as,

$$\lambda = \frac{h}{\sqrt{2m_0 eV}}, \qquad (2.1)$$

where, h is the Planck constant (6.626×10^{-34} J·s), m_0 is the rest mass of the electron (9.109×10^{-31}kg), e is the charge on the electron (1.602×10^{-19}C) and V is the operating

voltage of electrons. From equation (2.1) it can be seen that increasing V leads to a decrease in λ. In a modern TEM the accelerating voltage is typically 100-300 kV, which accelerates electrons to speeds greater than a half of light speed. Therefore a relativistic correction should be taken into account, and equation (2.1) should be written as,

$$\lambda = \frac{h}{\sqrt{2m_0 eV\left(1+{eV}/{2m_0c^2}\right)}}, \tag{2.2}$$

where c is the speed of light in vacuum. In this thesis, the microscope used has an accelerating voltage of 200 kV which corresponds to an electron wavelength of 2.51 pm.

A TEM comprises various components such as a vacuum system (incorporating pumps, valves and gauges), an electron source (gun), electron optics (including lenses and apertures), a sample and sample holders, detectors (such as spectrometers, a screen or a charge coupled device camera) and a control system (a PC, a associate software and control panels) [16]. The principal functions of the TEM are described in more detail in the following sections, with a focus on Lorentz TEM.

2.2.1 The electron source and selected modes in LTEM

Electrons in a TEM are produced by two methods: thermionic emission and field emission [16]. Thermionic emission utilizes materials with high melting points, *e.g.* tungsten or lanthanum hexaboride-LaB_6, that are heated to a high enough temperature (*i.e.* the operating temperature of tungsten is 2900K [16]) to excite a fraction of conduction electrons to overcome the work function of the material. Field emission instead utilizes an intense electric field around an artificially-sharp tip to extract electrons by direct tunneling to the vacuum. It produces a more coherent electron beam than thermionic emission.

In a field emission gun (FEG), the source is usually a tungsten needle, operating as a cathode, together with two anodes. The first anode extracts the electrons and the second one accelerates the electrons down the microscope column. To allow stable field emission, the source has to be operated under ultra high vacuum (UHV) conditions ($<10^{-11}$ Torr) to avoid contamination and oxidation of the tip surface. In both types of electron source, when extracted electrons travel down the microscope column, they pass through a crossover point that acts as a virtual electron source for the rest of the optical system. The diameter of the

crossover point determines the size of electron probe. The virtual source size of a field emission source is ~100 times smaller than that of a thermionic source. Thus, FEG TEMs are particularly suitable for applications such as high resolution TEM (HRTEM) and Lorentz imaging techniques (Lorentz TEM, LTEM) which require small coherence source with a small angular convergence at the sample. They also have a smaller energy spread than thermionic sources.

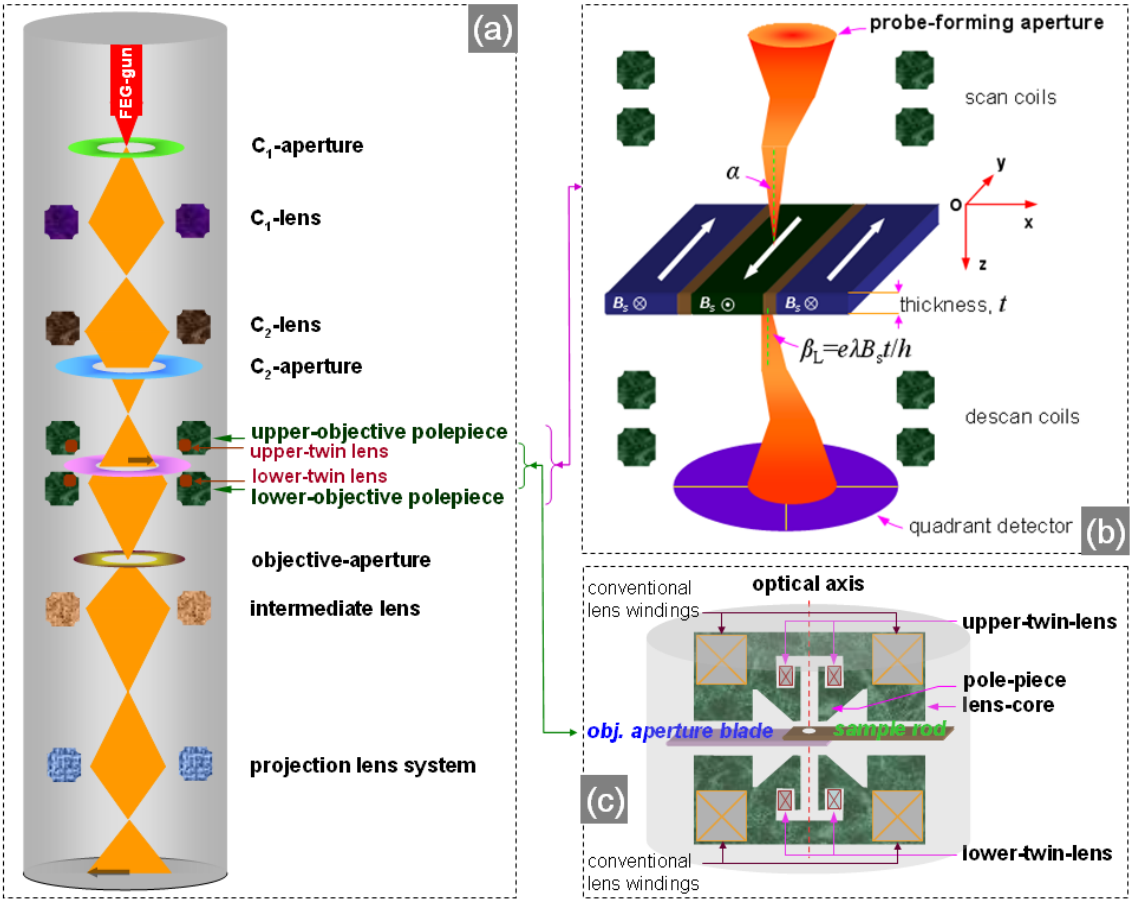

Fig. 2.1 (a) Simplified diagram of a FEG TEM column: electron projection paths, lens and aperture systems (left panel). (b) Schematic of the DPC mode of Lorentz microscopy (STEM) where the electron beam is focused as a finely small probe with the convergence angle of the incident beam is α. The probe is scanned over the magnetic thin film with thickness t. The emergent beam is deflected due to the Lorentz force with angle β_L below the specimen and the beam is not centered at the detector (right-upper panel). (c) showing the modified objective lens regime of the Philips CM20 microscope at Glasgow (right-lower panel).

For the imaging techniques used in this work, as shown in Fig. 2.1, the instrument (CM20 TEM) has been modified for advanced magnetic imaging, modified LTEM, as

shown in Fig. 2.1(c) [11, 17]. In the modified LTEM, if the main objective lens is on, the objective lens field at the sample is around 0.7 T. However, to allow samples to be studied without a strong applied magnetic field, the main objective lens is normally switched-off, thereby preventing a strong magnetic field from affecting the magnetic state of the specimen. Two additional mini-lenses (twin lens) are instead used for probe formation and replace the function of the objective lens (electromagnetic lens). The mini-lenses are located just above and below the sample and allow us to image in field free conditions (see Fig. 2.1(c)), and were used for Fresnel and differential phase contrast (DPC) modes in chapter 3. To distinguish those two modes of the LTEM, it can be simply recognized that the Fresnel mode is a de-focus technique (the details will be discussed in section 2.3), while differential phase contrast (DPC) imaging mode is an in-focus technique or scanning TEM (STEM) technique.

Using the mini lenses described above, the modified TEM/STEM can deliver spatial resolution of ten nanometers in in-focus modes. In the DPC technique, practiced in the scanning mode of LTEM, quantitative information on the magnetic induction can be obtained. Technically, in order to generate a finely focused probe in field free space, the objective lens is usually switched off and the upper twin lens is used to converge the beam, as shown in the right-upper panel of Fig. 2.1. Magnetic contrast in the sample is derived from the difference signal levels at opposite segments of the detector. The spatial resolution of the DPC image is determined by the diameter of the probe (β_L/α) [11]. The variation of the probe diameter depends on the scanning modes of the Lorentz STEM (LSTEM) operation: low magnification scanning (LMS) or high magnification scanning (HMS) mode. The differences between two modes are depicted in Fig. 2.2. Here, LMS mode is operated with the upper twin lens off, resulting in a large probe at the specimen with a smaller probe angle. Thus, this mode provides high sensitivity of the changes of magnetic induction or high magnetic contrast level. Whereas, the HMS mode is used with the upper twin lens on, resulting in a smaller probe diameter and larger probe angle. The achievable probe diameter and probe convergence angle of the LMS mode are about ~30 nm and 150 μrad, respectively while the probe diameter of the HMS mode is down to 10 nm and the probe angle of ~1 mrad. In the next chapter of the thesis, additional magnetic information was

observed by using the LMS mode besides a study of domain wall configuration. Although, the Fresnel imaging mode is mainly used in this project, the DPC mode is briefly introduced to provide additional information to the Fresnel imaging results.

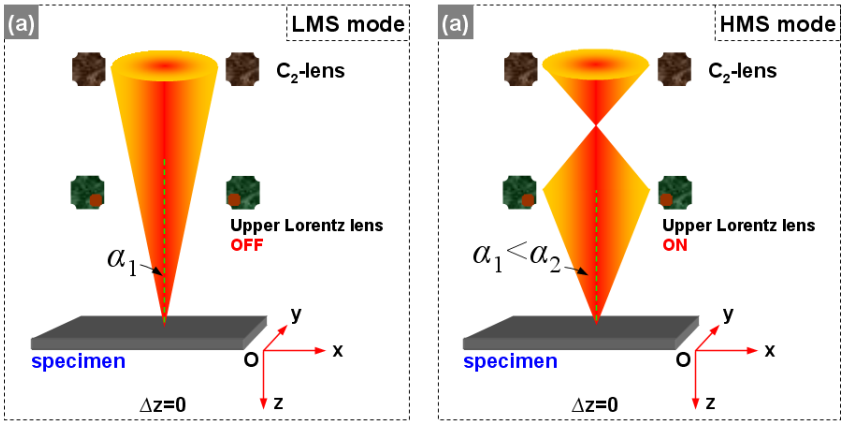

Fig. 2.2 Simplified schematic of scanning modes of the LSTEM operation. (a) Low magnification scanning (LMS) mode, the upper Lorentz lens is switched off, to form small probe convergent angle and large probe diameter at the specimen, whereas (b) High magnification scanning (HMS) mode, the upper Lorentz lens is switched on to achieve a small probe diameter and large probe convergent angle at the specimen.

2.2.2 Detectors in LTEM

Each electron microscope must have the capability to detect electrons resulting from electron beam-specimen interactions. Generally, a viewing screen is used to observe the final image that is located at the bottom of the microscope. The viewing screen is coated with a scintillating material, so that when an electron hits the screen surface light can be emitted. Alongside, digital detectors are also used in electron microscopes. The most common detector is a CCD camera. In this case, the detected electron beam energy is converted to photons by a scintillation plate, that is fibre-optically coupled to the CCD, and the photons are sent to the CCD chip. The captured images are sent to a computer screen and viewed automatically. In Fresnel mode, the CCD camera is mostly used to collect a real-space image, while in DPC mode performed in scanning mode, a quadrant detector is used to detect shift in intensity and position of the central diffraction disk. The quadrant detector is illustrated in the right-upper panel of Fig. 2.1. The quadrant detector is an extremely useful detector for the collection of isotropic scattering patterns. For the collection of accurate data, it is essential that the quadrant detector is positioned correctly

with respect to the scattering patterns. In the DPC used in this work, an eight-segment detector is used which allows a more flexible imaging setup [11].

2.2.3 Electron Optical System

As mentioned in section 2.2.1, the electron beam is extracted from the electron source then travels down the microscope column. A conventional TEM (CTEM) column is illustrated in Fig. 2.1 (left panel). When the electron beam travels down the microscope column, the electron beam intensity, probe size and convergence of the electron beam is controlled by a condenser lens system consisting of electromagnetic lenses. There are two main condenser lenses, C_1 and C_2: the C_1 lens controls the effective source size (spot size), whilst the C_2 lens is used to control the convergence angle of the beam and thereby the intensity of the illumination. So, the condenser lens system acts as a probe-formation system. Below the condenser lens system is a number of positionable apertures with different diameters. The C_2 aperture diameter sizes are varied in range of 20 to 200 μm and users can select a smaller aperture to provide a smaller beam probe angle or convergence angle of the sample. Further down the column, the objective lens system - the main imaging lens system is located below the condenser aperture system and determines the resolution of the microscope. The objective lens consists of two pole-pieces, as shown in the right-lower panel of Fig. 2.1. The pole-pieces are made from a soft magnetic material, *e.g.* iron, with a hole drilled through it. Cu-wire loops surround the pole-pieces which generate field strength. This force causes the electrons to travel in a helical path when traveling through the lens system. Subsequently, the image is rotated with respect to the original object [16]. Moreover, users can control the strength of the field by changing the focal length of the lens. The specimen is located between the upper and lower pole-pieces of the objective lens and therefore is immersed in the magnetic field used for focusing. In some cases the specimen is immersed in a field up to 2 T, aligned parallel to the optic axis of the microscope. A series of intermediate and projector lenses situated below the objective lens which magnify and project the image onto the viewing screen or camera. The intermediate lens and objective aperture are responsible for selecting the mode of operation of the microscope such as diffraction, dark and bright field modes and is discussed in sub-section 2.2.5. Especially, Lorentz image formation is affected by the objective aperture function at the diffraction

plane. This means that the incident wave is modified by transfer function and defocus parameters. Hence, Lorentz image formation is now discussed.

2.2.4 Image formation in TEM

To understand TEM image quantitatively, imaging formation mechanism is now discussed. Image formation in conventional TEM (CTEM) was reported [18, 19] based on the Abbe theory of optics (Fourier Optics) which applied to a sample plane in 2D real space and reviewed by Chapman [11], as recited in Fig. 2.3.

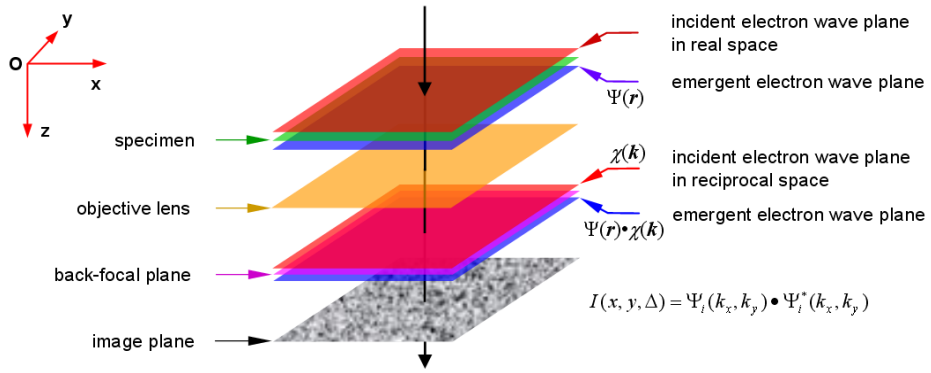

Fig. 2.3 Image forming mechanism in CTEM, recited from refs. [11, 20].

In Fig. 2.3, it is firstly assumed that a specimen is illuminated by an incident wave, $\psi(\boldsymbol{r})=e^{i\Phi(r)}$. The incident wave is modulated when it traverses the sample, then the emergent wave can be written in the form $\psi(\boldsymbol{r})=A(x,y)e^{i\Phi(r)}$, where $A(x,y)$ is the specimen transmittance. In the diffraction plane, effects of the objective lens are introduced into the wave function through spatial frequency ($\boldsymbol{k}$), an objective aperture function (OAF($\boldsymbol{k}$)) and an aberration function ($\chi(\boldsymbol{k})$, which belongs to the imperfect electromagnetic lens systems), where $k=1/\lambda$ is the wave number. Thus, the incident wave is modified by transfer function which includes the aperture function, spherical aberration and defocus (distances where a focused beam is off in either sides of the focal plane), and the emergent wave at the back focal plane can be written as

$$\Psi(k_x,k_y)=FT\left[\psi(\boldsymbol{r})\right]\bullet e^{i\chi(\boldsymbol{k})}\bullet OAF(\boldsymbol{k}). \qquad (2.3)$$

Here, FT is the Fourier transform operation and the aberration effect-$\chi(\boldsymbol{k})$ in the Lorentz microscopy is defined as a function of defocus value (Δ) and spatial frequency, expressed as [16]

$$\chi(\boldsymbol{k}) = 2\pi k^2 \lambda \left[\frac{\Delta}{2} + \frac{C_s \lambda^2 k^2}{4} \right], \tag{2.4}$$

where Δ is the defocus distance, C_s is the spherical aberration and λ is the wavelength of the electron. The OAF varies between 0 and 1, corresponding to a position outside and inside the objective aperture radius, respectively. By inverse Fourier transforming of the wave function in (2.3), the wave function at the image plane is observed as,

$$\Psi_i(k_x, k_y) = FT^{-1}\left\{ FT\left[\psi(\boldsymbol{r})\right] \bullet e^{i\kappa(\boldsymbol{k})} \bullet OAF(\boldsymbol{k}) \right\}, \tag{2.5}$$

The intensity of the image formed at the image plane is finally calculated by multiplying the wave function with its complex conjugate,

$$I(x, y, \Delta) = \Psi_i(k_x, k_y) \bullet \Psi_i^*(k_x, k_y), \tag{2.6}$$

As mentioned section 2.2.3, three selecting modes of basic TEM operation of the microscope are discussed in a following section.

2.2.5 General TEM imaging modes: *Diffraction, Bright and Dark Field Imaging*

When interpreting a TEM image, an important parameter is image contrast which is generally defined as the difference in intensity between two neighboring areas, $\Delta I/I$, where ΔI is a difference of intensity between two areas and I is the intensity (see equation (2.6)) at one of those areas (or mean intensity). Contrast can arise from various electron-specimen interactions. There are several interactions that can occur in the specimen when electrons pass through, *i.e.* the electron-specimen interaction produces forward, backscattered electrons, inelastic, elastic electrons and secondary signals [16, 21]. There are two major types of contrast in the TEM image: amplitude contrast and phase contrast. In a particular situation, one of them tends to be dominant in image contrast. Amplitude contrast arises from a variability in mass-thickness, Z and diffraction contrast. Phase contrast is where the incident wave-front is slightly retarded in comparison with a reference area and where the phase varies across the exit wave-front. This results in constructive and destructive interference, known as lattice fringes, Moiré fringes and Fresnel contrast (in the FEG Philips CM20). Now, selected modes of the conventional TEM are presented as the followings.

Diffraction Mode: When incident electrons scatter with the atoms in a specimen, the electrons will be partly reflected by differing angles from the atomic planes with Miller indices (*hkl*) [16]. Constructive interference of the electrons reflected from neighboring planes occur if Bragg's law is satisfied, $2d\sin\theta=n\lambda$, where d is the lattice spacing of an individual structure, n is an integer, λ is the wavelength of electrons and θ is the Bragg angle, as shown in Fig. 2.4(a). A difference of electron paths from neighboring planes causes constructive or destructive interference in phase, diffraction pattern is therefore observed. Indeed, different materials give rise to different types of diffraction spots/patterns which depend on the order of atomic orientations (long/shot-range order).

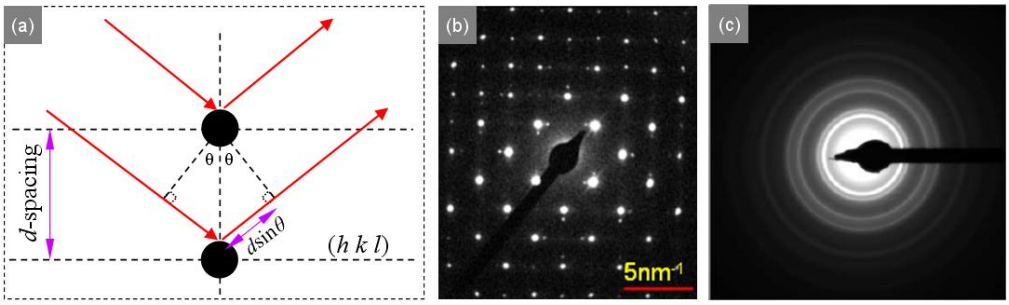

Fig. 2.4 (a) Parallel incident electrons are reflected from (*hkl*) planes and interference occurs when the path difference satisfies Bragg's conditions, (b) and (c) are recorded diffraction patterns from an evaporated single crystal film of Gold, Au(100) and a 20 nm-thick polycrystalline permalloy nanowire, reproduced from ref. [13].

For example, a single crystal material gives rise to a pattern with periodic spots (Fig. 2.4(b)), while polycrystalline materials create superposition of many single crystal spot patterns which merge into rings (Fig. 2.4(c)). Partly similar to the polycrystalline material, the diffraction pattern of an amorphous material has a single fuzzy ring belonging to random azimuthal order because this type of material has no periodicity in any direction. For all types of diffraction patterns, the amplitude of electron intensity tends to reduce when moving away from the centre at the periodic spots/rings. The reason for that is the scattering probability decreases with increasing angle (far away from the centre). Thus, electron diffraction mode in the TEM is useful to investigate structural and/or geometrical characterizations of specimens. It provides information on the crystal structure of a material, for example, the symmetry and grain size distribution.

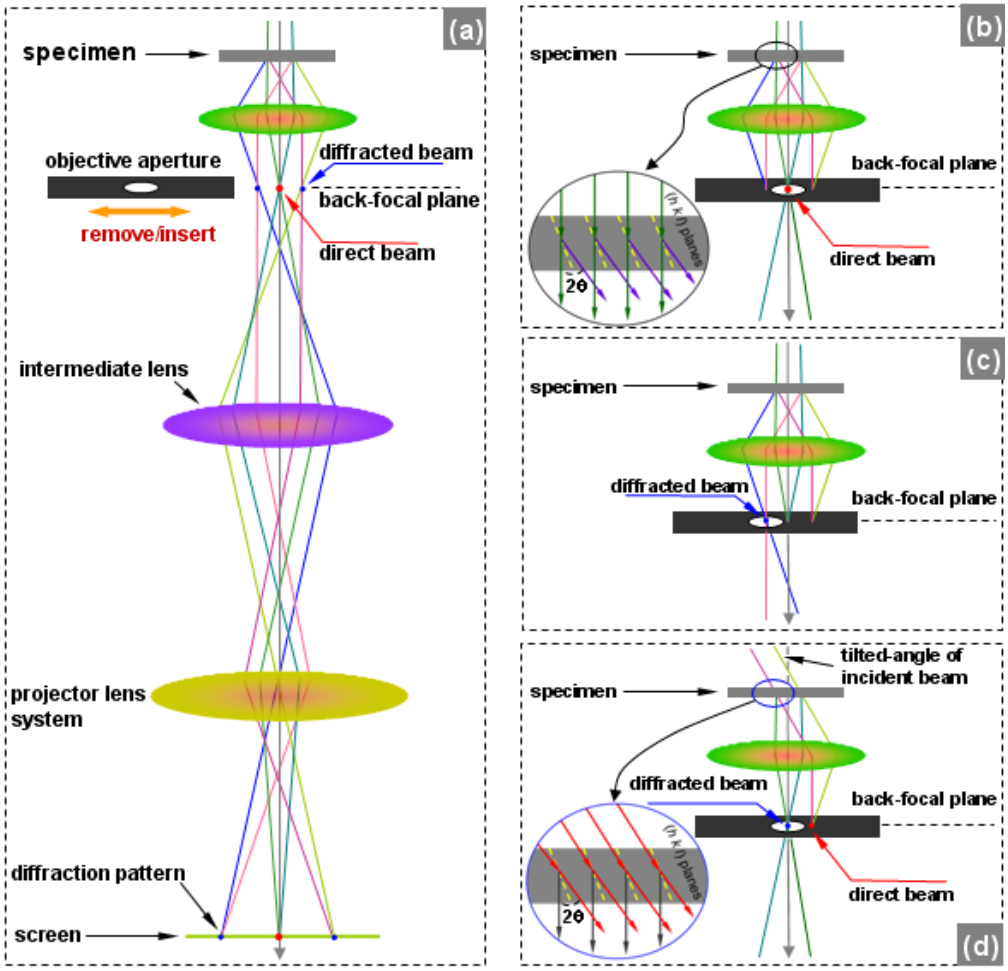

Fig. 2.5 Simplified schematics of (a) full diffraction (b) bright field (c) dark field and (d) centered DF imaging modes. The insets illustrate the principle of electron diffraction in the TEM for the BF and the centered DF imaging modes.

Bright and Dark Field Imaging Modes: As shown in Fig. 2.5(a), the diffraction spots of a single crystal specimen are imaged on the screen which consists of a bright central spot (red) and surrounding spots (blue). Here, the diffraction pattern was imaged using all transmitted electrons from the whole area of interest of the specimen. An image can either be formed using the bright central diffraction spot, known as bright field (BF) imaging mode or using surrounding spots by inserting an objective aperture, known as dark field (DF) imaging mode. These modes are depicted in Fig. 2.5(b) and Fig.2.5(c), respectively. By inserting an objective aperture into the back focal plane of the objective lens when working in the BF or DF imaging mode, the level of image contrast can be improved. The role of the objective aperture is to prevent scattered electrons from a range of Bragg angles

contributing to the final image. The DF imaging mode is particularly useful for materials with large variations in mass, thickness and atomic number, *Z*. For instance, a structure consisting of many layers with different materials and compositions is shown in Fig. 2.6. The specimen was provided by Dr. R.J. Macedo at INESC-MN, Portugal and the images were captured by Dr. Sam McFadzean, University of Glasgow.

However, to avoid use of electrons that travel off-axis and are affected by lens aberrations, the beam can be tilted about the specimen so that the beam hits the sample with an angle equal and opposite to the scattering angle. The scattered electrons now travel along the optic axis and this sub-mode is known as centered dark field (CDF) imaging (Fig. 2.5(d)).

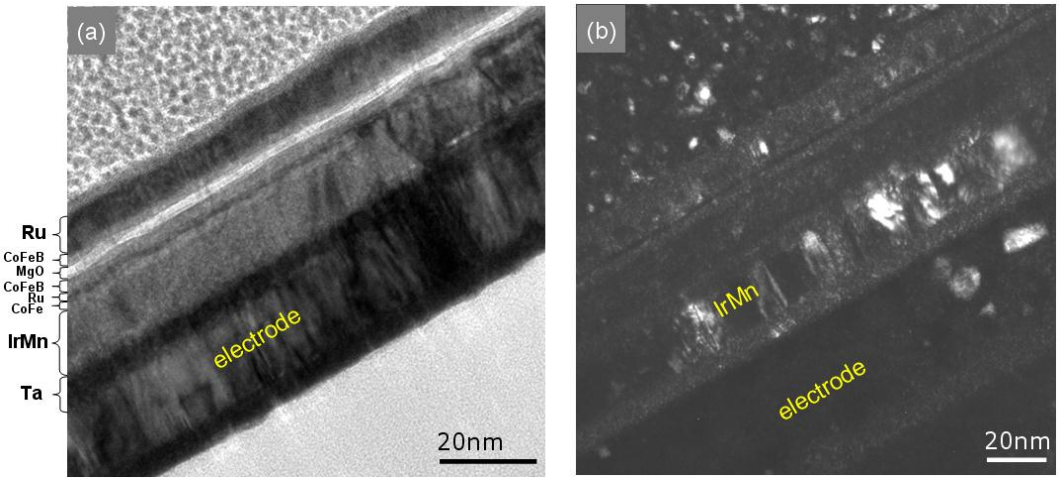

Fig. 2.6 High resolution TEM images of a magnetic tunnel junction (MTJ), structured as Si/electrode/Ta(5)/$Mn_{74}Ir_{26}$(15)/$Co_{82}Fe_{18}$(3)/Ru(0.8)/$Co_{74}Fe_{16}B_{10}$(4)/MgO(3)/$Co_{74}Fe_{16}B_{10}$(3)/Ru(5)/Ta(5)/ (units in nm). The images of the MTJ structure were taken in (a) BF and (b) CDF modes, respectively. A brighter line within layers in the BF image is the barrier layer, it can be seen easily, whereas it is hard to distinguish in the DF image where the homogeneous barrier layer is not dominate in the dominant contrast. However, the *Z* contrast is improved in the DF image for IrMn layer. This specimen was provided by Dr. R.J. Macedo at INESC-MN, Portugal.

2.3. MAGNETIC IMAGING-LORENTZ TEM

In the Lorentz microscope, when the extracted electrons pass through a magnetic specimen, the emergent electrons are deflected by the Lorentz force produced by the magnetic field within and surrounding the magnetic specimen. The Fresnel imaging mode is

depicted in Figs. 2.7(a-c), if the Lorentz lens is de-focused by values of ±Δz (in Oz-direction), either under-focused (-Δz) or over-focused (+Δz) with respect to the focal plane, subsequently magnetic contrast is generated in the Fresnel image. If the deflected electrons are in-focused, resulting there is no magnetic contrast in the Fresnel image.

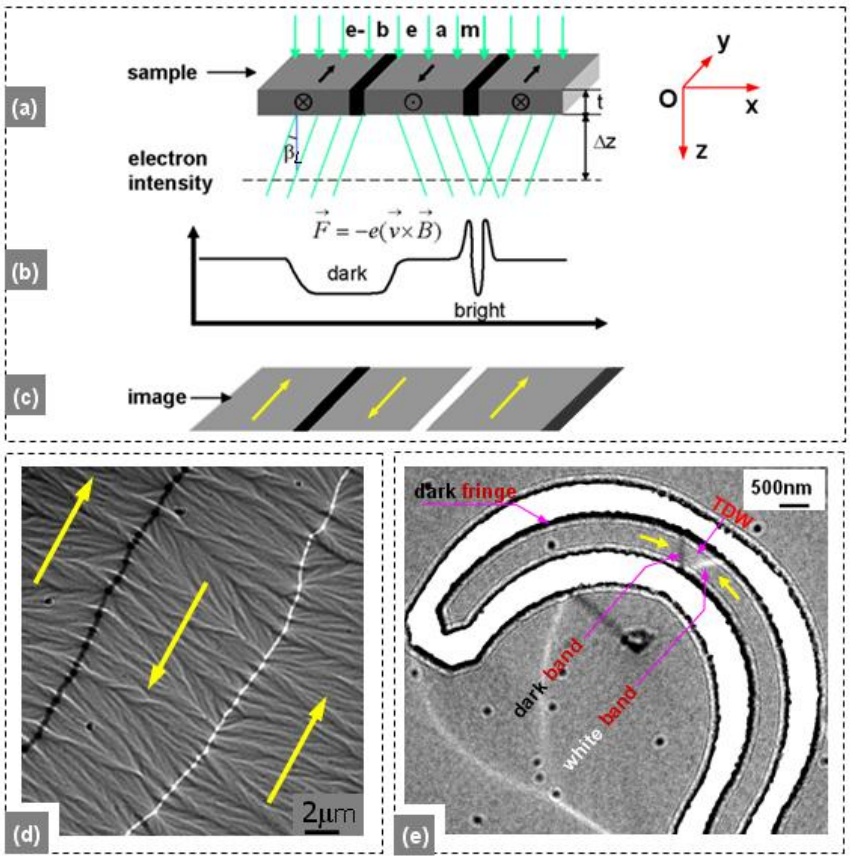

Fig. 2.7 (a) Simplified diagram of the electrons deflected by the classical Lorentz force, (b) is intensity profile of transmitted electrons at position below the specimen where valley and peak correspond to darker and brighter bands are shown in (c). (d) is a Fresnel image of 20nm-thick continuous Py film which shows domain walls on magnetic ripple background and (e) is a patterned magnetic permalloy element with a transverse domain wall appears as dark and white boundaries.

In Fig. 2.7(a), an electron beam that is transmitted through a thin ferromagnetic specimen consisting of 180º domain wall structures (the magnetization rotates by 180°). The beam is then deflected by the Lorentz force with deflection angle, β_L. This force deflects the electrons from neighbouring domains in opposite directions. The domain wall appears as bright and dark bands against a neutral background, as shown in Figs. 2.7(b) and (c). For examples, Fresnel images of a continuous Py film and patterned Py nanowire are

shown in Fig. 2.7(d) and (e), respectively. Fig. 2.7(d) shows a Fresnel image of a 20 nm-thick continuous Py-film containing 180°-walls with magnetization indicated by yellow arrows on a magnetic ripple background. The other Fresnel image is of a 10 nm-thick-patterned Py-nanowire containing a transverse domain wall appears with dark and white bands, as shown in Fig. 2.7(e). Here, a dark fringe also appears along the wire edge which due to the transition between magnetic and non-magnetic material, in which the electrostatic effects come from change in the mean inner potential, this will be discussed details on section 2.3.2.

In the Fresnel mode, the defocused values can be evaluated for a particular condition of each Fresnel measurement. Now returning to equations (2.3)-(2.6), the image intensity is not simply related to specimen properties, but also related to the changes in phase of the electron beam in the microscope, such as spherical aberration, defocus and electron wavelength. However, a number of simplification operate in practice, objective aperture is not normally used for the Fresnel imaging mode and the spherical aberration (C_s) compensation is negligible compared with defocus. Besides, the C_s and λ of a given LTEM are fixed. Therefore, the variation in the $\chi(\boldsymbol{k})$ function comes mainly from the defocus value, Δ. It means that changing the defocus values causes the PCTF to vary. If plotting the PCTF as a function of spatial frequency, $\boldsymbol{k}$, the trend of the PCTF curve goes on forever to high resolution with $\boldsymbol{k}$ increasing, the PCTF is theoretically expressed as [16],

$$PCTF = \sin\left[2\pi k^2 \lambda \frac{\Delta}{2}\right] \tag{2.7}$$

However, in practice the PCTF is damped and vanishes at high order of the $\boldsymbol{k}$. Then, the equation (2.7) passes through zero a number of times and eventually vanishes, $\sin(\pi k^2 \lambda \Delta)=0$ or $k^2\lambda\Delta = n$, this is equivalent to

$$k^2 = \frac{1}{\lambda\Delta} n, \tag{2.8}$$

where, n is the point number when the PCTF curves crosses k-axis until the PCTF vanishes (n is odd or even correspond to bright or dark rings in the Fast-Fourier Transform, FFT, and k is radii of bright and dark rings). This equation is useful as a fast route to estimate the defocus value for a particular specimen under given TEM condition. For example,

experimental k^2 values versus n for the FFT image (diffractogram) which were extracted from defocused Fresnel image of Au grating specimen is presented in Fig. 2.8. The slope of the linear fit for the experimental results is of 111. This value is equal to $(1/\lambda\Delta)$ from equation (2.8), then the defocused value can be found, $\Delta \approx 3600$ μm. This defocus value was used for the Fresnel image as showed in Fig. 2.7(e). To understand the magnetic image quantitatively, classical and mechanical quantum approaches are usually used to aid interpretation of Fresnel image, which are described in the following sections.

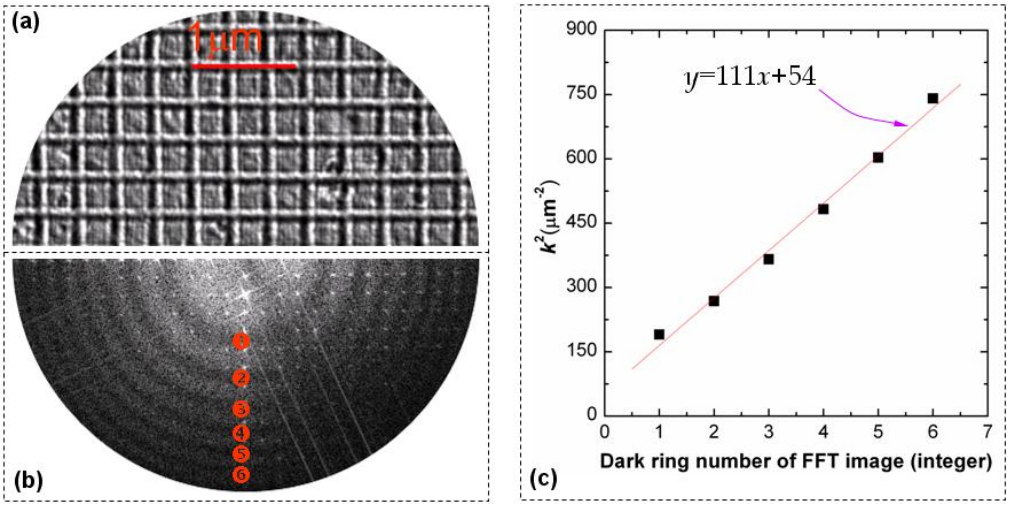

Fig. 2.8 (a) A defocused Fresnel image of Au cross-grating with the lattice periodicity of 463nm-cell-size and (b) its FFT image where 6 points are shown which correspond to 6 spatial frequency values, (c) k^2 versus ring number as a linear function when the PCTF crosses ***k***-axis.

2.3.1 Classical approach

As stated in the beginning of section 2.3, when passing through a magnetic material with in-plane magnetization (the sample plane) split by 180°-domain walls (a Néel wall as described in section 1.5), the transmitted electrons are deflected by the Lorentz force through a small deflection angle β_L, as shown in Fig. 2.7. The deflection angle in relation to the x-coordinate is considered as $\beta_L(x)$ [11] and can be written as,

$$\beta_L(x) = \frac{e\lambda}{h}\int_{-\infty}^{+\infty} B_\perp(x,y)dz, \qquad (2.9)$$

where, $B_\perp(x, y)$ is the induction component in Oy-direction at point (x, y). Assuming that stray field effects are negligible, the specimen thickness (t) and saturation magnetization

(M_s) are uniform then the deflection angle can be rewritten as

$$\beta_L(x) = \frac{eB_s t\lambda}{h}, \tag{2.10}$$

where B_s is the saturation induction ($B_s=\mu_0 M_s$). In the case of a permalloy film with film thickness of 20 nm, the given saturation induction is 1T, giving β_L around 12 μrad. This value is far smaller than a typical first order Bragg angle of about 10 mrad [20]. Here, the classical approach was simply considered an effect of the transmitted beam which is deflected by the Lorentz force produced by in-plane induction components in a magnetic specimen. However, another approach considers the electron phase changes when the electron beam traverses a specimen, in which the transmitted beam is modulated in phase by the specimen, resulting in differing paths of electron trajectories at the electron intensity plane. The phase changes can be visualized in the final image by using the DPC technique. The phase changes can be due to many reasons such as inhomogeneous in specimen thickness, the boundary between magnetic and non-magnetic materials and it can be used to recognize atomic structure, magnetic structure, different materials, sample thickness variations/defects. So, the classical approach is not sufficient when quantitative information is required and for image calculation a mechanical quantum approach is essential.

2.3.2 Mechanical Quantum approach

A mechanical quantum approach to electron propagation through magnetic materials was first described by Aharonov and Bohm [22]. The effect is described as electrons from an electron source or point source are traveled to a magnetic specimen with a magnetic induction, $\boldsymbol{B}$, in different trajectories, p_1 and p_2. This difference (Δp) is due to a phase shift, Φ_m, in which magnetostatic effect affects the electron trajectories when they traveled to the specimen. The phase shift is therefore included in a magnetic image, as shown in Fig. 2.9(a). This effect was recently considered details by McVitie *et. al.* [23] and it has the form as shown in equation (2.11),

$$\Phi_m(x,y) = -\frac{e}{\hbar}\int_{-\infty}^{+\infty}(\boldsymbol{A}\bullet\boldsymbol{n})dz, \tag{2.11}$$

where $\boldsymbol{n}$ is the unit vector normal to the wavefront of the beam, $\hbar = h/2\pi$ and $\boldsymbol{A}$ is the magnetic vector potential which in the 3-D coordinates in which $\boldsymbol{A}$ is in relation to $\nabla\times\boldsymbol{B}$. For

a general description of Maxwell's equation, $\nabla\times\boldsymbol{B}=\nabla\times\mu_0(\boldsymbol{M}+\boldsymbol{H})=\mu_0[(\nabla\times\boldsymbol{M})+(\nabla\times\boldsymbol{H})]=\mu_0\boldsymbol{J}_m+\mu_0(\boldsymbol{J}_c+\boldsymbol{J}_d)$ where $\boldsymbol{J}_c(\boldsymbol{r})$, $\boldsymbol{J}_d(\boldsymbol{r})$ and $\boldsymbol{J}_m(\boldsymbol{r})$ are conduction, displacement and Ampérian current density contributions, respectively. In a static situation, there is no conduction and displacement current contributions or $\nabla\times\boldsymbol{B}(\boldsymbol{r})=\mu_0\boldsymbol{J}_m(\boldsymbol{r})$. Thus, this description is equivalent to the *curl* of induction/magnetization, just one difference is the multiplicative $\mu_0/4\pi r$, where μ_0 is the permeability of free space and the $1//4\pi r$ term is proportional to $1/\boldsymbol{k}^2$ ($\boldsymbol{k}$ is Fourier space). Thus, the magnetic phase shift in the presence of Ampérian current density can be rewritten as the following, [23]

$$\Phi_m(x,y)=-\frac{e\mu_0}{4\pi\hbar r}\otimes\int_{-\infty}^{+\infty}[\nabla\times\boldsymbol{M}(\boldsymbol{r}(x,y,z))]\boldsymbol{n}dz, \tag{2.12}$$

The symbol $\otimes$ denotes a convolution in 2-D coordinates. Assuming that the *xy*-plane is well defined in the film plane, the incident beam is along the *z*-direction and the magnetization is uniform through the film thickness (t), equation (2.12) becomes,

$$\Phi_m(x,y)=-\frac{e\mu_0 t}{4\pi\hbar r}\otimes[\nabla\times\boldsymbol{M}(\boldsymbol{r}(x,y,z))]\hat{z}, \tag{2.13}$$

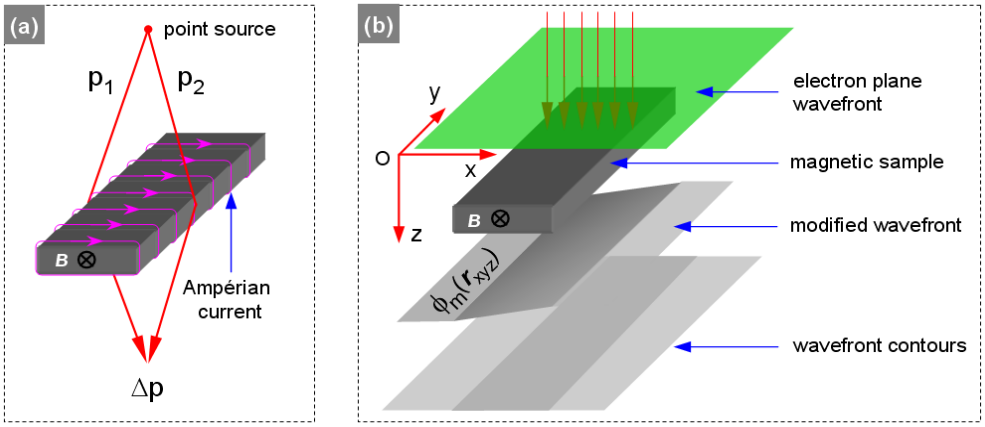

Fig. 2.9 (a) Simplified schematic of the electrons with different paths (p_1 and p_2) from a high coherence source interact with a magnet associated with the Ampérian current are virtually turned around where phase shift belongs to the different of the paths (Δp) is considered in a quantum mechanical approach. (b) is an evolution of an electron plane wavefront as it traverses a magnetic material with a single domain.

Theoretically, the level of contrast in Fresnel image is related directly to the values of defocus and differing in the phase of transmitted electrons [23], and the intensity of the Fresnel image can be written in a form,

$$I(\boldsymbol{r},\Delta) = 1 - \frac{\lambda \Delta z}{2\pi} \nabla_{\perp}^{2} [\phi(\boldsymbol{r})], \tag{2.14}$$

where, Δz is the defocused distance (in the Oz-direction), $\nabla_{\perp}$ is the Laplacian relating to in-plane coordinates and $\phi(\boldsymbol{r})$ is the 2-D-phase function for the in-plane spatial coordinates of the specimen, $\boldsymbol{r}(x,y)$. Thus, the Fresnel imaging intensity is affected by phase effects arise from induction field, $\boldsymbol{B}$, induced by the magnetization of specimen as mentioned above.

From equations (2.13) and (2.14), the authors in ref. [23] proved that,

$$I(\boldsymbol{r},\Delta) = 1 - \frac{e\mu_0 t \lambda \Delta z}{h} curl\left(\boldsymbol{M}(\boldsymbol{r}(x,y,z))\right)_z, \tag{2.15}$$

The above relation can be used to interpret the Lorentz image intensity relative to the sample magnetization [20, 23]. The relation in equation (2.15) was calculated for the linear regime of defocused values ($0 \leq \Delta \leq 160$ nm) [23] and this relation will be used in chapter 3 for MatLab calculations. However, experimental results are largely concerned with the non-linear regime of defocused values (*i.e.* Δ = 3600 μm), this aimed to observe Fresnel images with higher contrast. In addition to Φ_m, a considerable phase shift arises from electrostatic interactions, Φ_e, is also present in the Lorentz images. This derives from variations in either the thickness or the mean inner potential of the specimen and is written as,

$$\Phi_e = \pi \frac{Vt}{\lambda E}, \tag{2.16}$$

where V is the inner potential of the material (*e.g.* 21V for permalloy). This effect can be included in calculated Lorentz images and aids interpretation of the contrast (section 2.3.3). The sum of the two phase contributions is expressed as the total phase change, $\Phi(\boldsymbol{r})$,

$$\Phi(\boldsymbol{r}) = \Phi_m + \Phi_e, \tag{2.17}$$

In order to understand more details, Lorentz image calculations are considered below.

2.3.3 Lorentz image calculation: *Digital Micrograph Calculation*

The OOMMF simulation package [19] which was mentioned in chapter 1 is used for modeling realistic structures. OOMMF images of perfect structures are calculated to understand the roles of each contribution such as magnetic phase, electrostatic phase, amplitude effects and/or sum of those contributions. This might provide useful information for interpreting the experimental images with complex magnetic configurations. Here, two

methods of image calculations are introduced by using Digital Micrograph™ and MatLab software. The methods are discussed below.

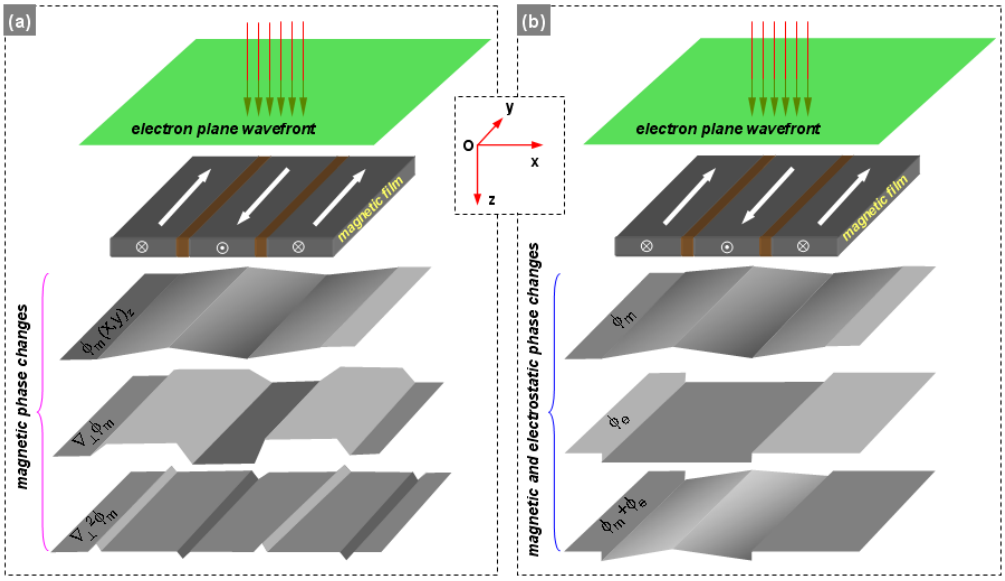

Fig. 2.10 (a) Schematic of the magnetic phase change when electrons traverse a magnetic specimen consists of 180°-walls. Magnetic phase profile of emergent electron wave form at the back focal plane, derivative and Laplacian are alternatively illustrated. (b) image intensity profiles of phase shift (Φ_m), electrostatic phase (Φ_e) and the sum of two phase contributions.

Returning to the concepts introduced in sections 2.3.1 and 2.3.2, a schematic of the phase change when the beam traverses the magnetic specimen is shown in Fig. 2.10. Here, the domain wall width has been neglected and the magnetic phase is represented as a triangular wave form, Fig. 2.10(a). The derivative and Laplacian forms of the magnetic phase are also shown in Fig. 2.10(a). Moreover, an inclusion of the magnetic phase and electrostatic phase is presented in Fig. 2.10(b) where the electrostatic phase has a rectangular wave form. To calculate a Lorentz image which involves the magnetic phase and electrostatic phase, a multiplication of two Fourier transform functions is to be computed in Fourier space (***k***). Therefore, the image calculation needs to use a Fast Fourier Transform algorithm [19] which is available in the Digital Micrograph (DM) software. The scripts of DM used to calculate the phase and Fresnel images were written by Dr. Stephen McVitie and Mr. Gordon White at the University of Glasgow [24]. Fresnel and DPC image calculations are now described as an example to understand the role of magnetic phase and electrostatic phase affected the whole contrast profile intensity of a Lorentz image.

Fresnel imaging intensity is considered as a non-linear function however the conditions for the Fresnel image can be treated as linear function under certain conditions for quantitative application [23]. To calculate the Fresnel image, a uniform incident electron wave with no amplitude variation is assumed. The emergent wave at the back focal plane is then calculated by a multiplication of the Fourier transform of the incident wave and the transfer function (see equations (2.3)-(2.5)) with spherical aberration and wavelength are 8000mm and 2.51pm, respectively for the Glasgow Lorentz TEM physical parameters. The image intensity is finally calculated by using equation (2.6).

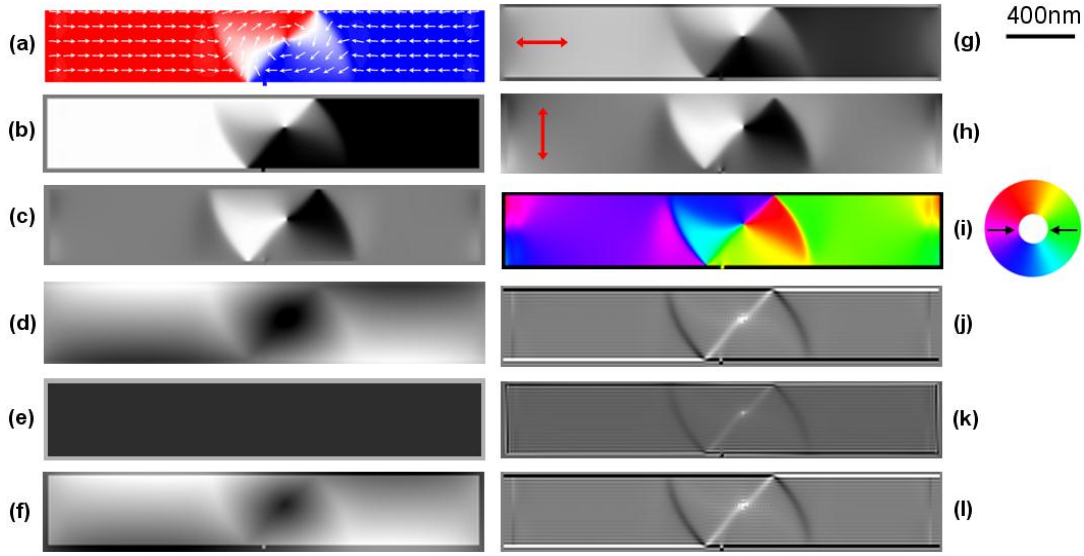

Fig. 2.11 A vortex domain wall was simulated by OOMMF for a 19.5nm-thick permalloy nanowire with the dimension of 400nm×2500nm. (a) the output OOMMF image; (b) and (c) are the M_x and M_y components of magnetization; (d), (e) and (f) are calculated magnetic phase, electrostatic phases and magnetic plus electrostatic phase, respectively. The magnetic phase is differentiated to obtain the orthogonal induction maps. The images are sensitive to magnetic induction components indicated by red arrows, as shown in (g) and (h); (i) is the color DPC image included magnetic phase only; (j), (k) and (l) are the Fresnel images calculated from the purely magnetic phase, included magnetic plus electrostatic plus amplitude effects, and *curl*$(M)_z$ (see equation (2.15)), respectively. The Fresnel images with the purely magnetic phase and included effects were calculated in the conditions of C_s=8000mm, λ=2.51pm and defocused value of 1μm.

As discussed briefly in section 2.2.1, in differential phase contrast microscopy, as shown in the right-upper panel of Fig. 2.1, the electron beam as a fine probe is scanned over the specimen. Consequently, a DPC image is formed by a combination of detector segment

signals where phase changes are converted to intensity variations. The DPC signal is extracted by taking the derivative of the electron phase perpendicular to the electron beam which was presented in the equation (2.11),

$$\nabla\Phi_m(x,y) = -\frac{e}{\hbar}\int_{-\infty}^{+\infty}(\nabla\times\boldsymbol{A})\times\boldsymbol{n}dz = -\frac{e}{\hbar}\int_{-\infty}^{+\infty}(\boldsymbol{B}\times\boldsymbol{n})dz, \qquad (2.18)$$

The DPC signals are therefore related to the integrated magnetic induction perpendicular to the beam. The derivation of the phase shift is taken along two orthogonal components. Phase changes are relative observed in neighbouring domains with opposite magnetization directions which correspond to brighter and darker regions in the intensity.

As an example is shown in Fig. 2.11, a vortex domain wall was first simulated by OOMMF and then calculated by the DM software. Fig. 2.11(a) shows a simulated vortex domain wall in a 19.5nm-thick permalloy nanowire with the dimension of 400nm×2500nm. The red and blue regions indicate two areas with opposite magnetization directions. Figs. 2.11(b) and (c) show the M_x and M_y magnetization components extracted from simulated image, respectively. Figs. 2.11(d), (e) and (f) present alternatively calculated magnetic phase, electrostatic phases and sum of magnetic, electrostatic effects. The magnetic phase is differentiated to obtain the orthogonal induction maps. Thus, the images are sensitive to magnetic induction components indicated by red arrows in Figs. 2.11 (g) and (h). Fig. 2.11(*i*) shows the color DPC image (included magnetic phase only) calculated from the given induction components where induction map is based on a $\tan\theta=B_x/B_y$ relation, θ is the angle between B_x and B_y components. Figs. 2.11(j), (k) and (*l*) show the Fresnel images calculated from the purely magnetic phase, included magnetic plus electrostatic effects and $curl(M)_z$, respectively and all of them are well presented the VDW configuration. However, the Fresnel images which included purely magnetic phase and *curl*(M)z (Figs. 2.11(*j*) and (*l*)) have greater contrast than the other one (Fig. 2.11(*k*)). Hence, one can conclude that the electrostatic effect affects directly the magnetic contrast in a Lorentz image.

Understanding of the magnetic and electrostatic effects, the imaging interpretation is straightforward for simulation results. In fact, a real image is affected by other contributions, *e.g.* diffraction contrast, this leads the image intensity profile is sometimes harder to interpret. This is to be recalled and discussed for typical situations in chapters 3.

2.3.4 Lorentz image calculation: *MatLab Calculation*

A quantitative understanding the internal structure of ATDWs, specifically the degree of asymmetry or symmetry is the main purpose of the next chapter. MatLab software was used to automate measurements of DW asymmetry from OOMMF images. By using this method, components of magnetization (M_x, M_y, M_z) and areas inside domain wall can be extracted directly. The image formation in MatLab is calculated based on equation (2.15) where image intensity is proportional to $curl(M)_z$ (see Fig. 2.11(*l*)). Details of this calculation and results for particular cases are to be discussed in chapter 3.

2.4. EXPERIMENTAL CHARACTERIZATION TECHNIQUES

So far, the basis concepts of magnetic imaging mechanisms and Lorentz image calculations were discussed. In this thesis, two applications were used to acquire Fresnel images in continuous (DC) field or in-situ magnetic field and discontinuous (pulsed) field, are described here. The DC field application allows users to apply an in-situ magnetic field which is achieved by weakly exciting the objective lens. By applying the in-situ magnetic field, it can be used to nucleate, propagate domain walls and drive them from a position to another within a magnetic nanostructure. Even though both DC and pulsed fields were used, the in-situ DC application was extensively used in the thesis aiming to explore magnetic domain wall behaviour in different specimen geometries, while the pulsed filed method is described here as an introduction and this method was used in the project, but results will be presented elsewhere.

2.4.1 Fresnel imaging technique: *Application of DC Field*

Fig. 2.12 demonstrates a measurement method using continuous in-situ DC field [25-31] where a specimen is mounted in the specimen rod (Fig. 2. 12(a)) and tilted to introduce // and ⊥ field components (Fig. 2.12(b)). Here, the sample is magnetized by applying a DC field produced by the objective lens. The produced field direction is either up or down, determined by controlling the DC current direction through the objective lens coils. In the initial state, the specimen plane is horizontal (0°-tilted). This means the objective lens field is perpendicular to the specimen plane, so there is no field component applied to the horizontal sample plane. When the specimen is titled, at angle α°, the field component in the

horizontal plane, $H_{//}$, is given by $H_{//} = H\sin\alpha$. The sample can be applied with the maximum field value when the sample plane tilted 90°. The maximum magnetic field can be generated by the objective lens is less than 0.7 Tesla.

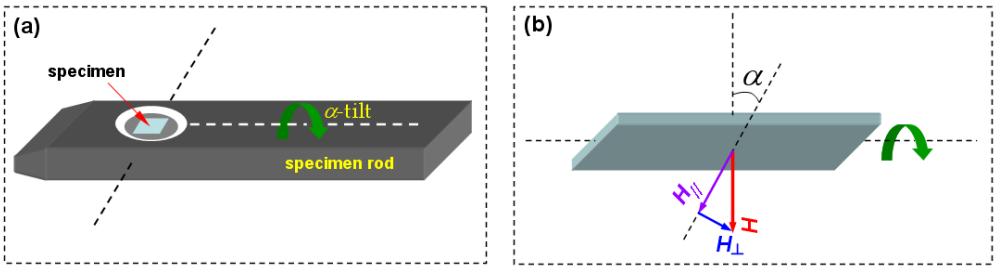

Fig. 2.12 (a) A specimen mounted in the sample rod where the specimen can be magnetized by DC field when objective lens on, (b) is presented parallel and perpendicular magnetic field components applied in the specimen.

2.4.2 Fresnel imaging technique: *Application of Pulsed Field*

As an alternative of the measurement method described above, instead of a DC field, pulsed fields were also produced to magnetize magnetic specimen/nanostructures, as shown in Fig. 2.13, for some of the results in this project but results are not presented here. The pulsed fields generated by this method can quickly build up lots of statistics. They are particularly useful when the DC fields are in a relation with a periodicity of short-time, μs or *ns*. This might provide useful information on the reliability of a specific process in a magnetic specimen, *e.g.* domain wall dynamics in μs-time scale. Technically, the magnetic pulsed field is produced by a pulsed current of two parallel gold wires located below the sample plane. The two gold wires plane is fixed and parallel to the specimen plane. This is a difference with the sample states in the DC field measurement, so the pulsed field is always applied parallel to the sample plane. Using an Agilent Function Generator, arbitrary waveforms of a given frequency and amplitude can be generated which controlled by a 100A-Power Supply connected to the specimen rod. Magnetic field pulses of up to around 200 Oe can be applied to the specimen [13]. The pulse lengths that are achievable with this set-up are in range 0.1-5μs. This method associates with the DC field measurement are to be useful as a combination of static and pulsed field measurements.

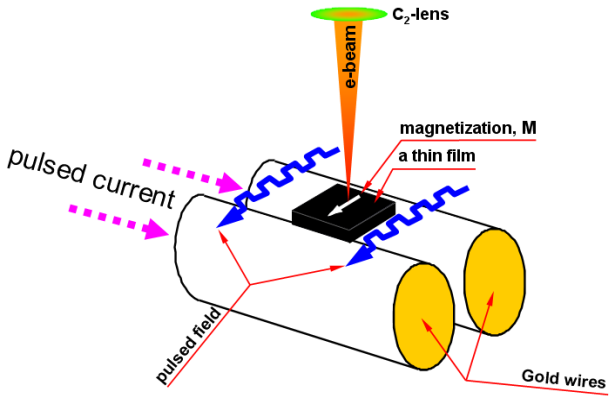

Fig. 2.13 Simplified diagram of a thin film sample is magnetized by pulsed fields which were produced by the traditional designed magnetizing stage [13].

2.4.3 DPC technique

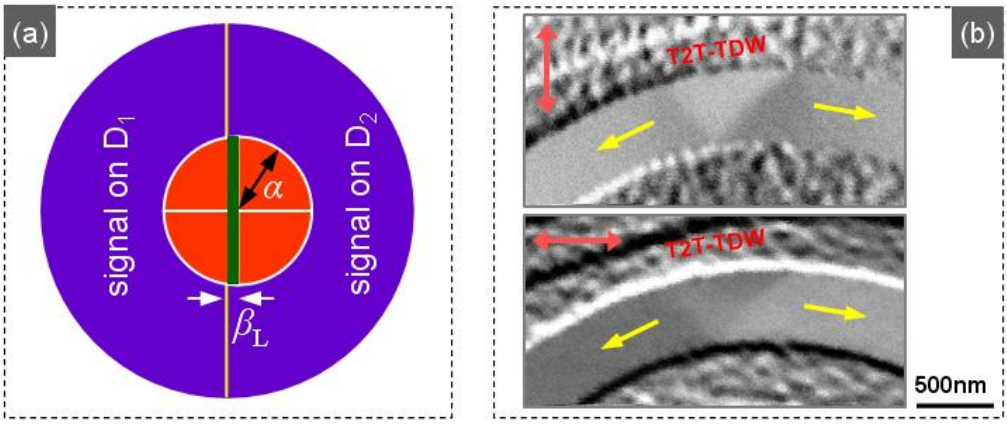

Fig. 2.14 (a) A schematic of the method to calculate DPC signal from the quadrant detector where the convergence angle of the incident beam (α) and deflection angle (β_L) are projected on the detector, described as α and β_L distances. (b) Two orthogonal DPC images of 10nm-thick-patterned Py-nanowire with dimension of 500nm-width×10μm-length where a transverse domain wall was created (details are to be discussed in chapter 3).

As previously discussed, the DPC mode provides better resolution than Fresnel imaging mode in which the beam is focused to a small probe and is scanned across the specimen. The transmitted beam is detected by an 8-segment detector. The image intensity predominantly depends on the magnetization direction or magnetic induction in the domain and detector segment positions. By taking derivative segment detector signals in a plane perpendicular to the normal vector of the emergent electron beam, differential phase contrast can be calculated as,

$$\nabla\Phi_{\perp}(x,y) = -\frac{e}{\hbar}\int_{-\infty}^{+\infty}(\boldsymbol{B}\times\boldsymbol{n})dz = -\frac{e\bullet t}{\hbar}[\boldsymbol{B}(x,y)\times\boldsymbol{n}], \tag{2.19}$$

Experimentally, the convergence angle (α) of the probe is directly related to the radius of the projection beam on the detector when the Lorentz deflected angle (β_L) is small and comparable to the probe angle. This condition is ensured to approximate the arc of circle as a line and satisfied the linear imaging dependence condition. A simplified schematic illustrating how a signal is generated is shown in Fig. 2.14(a). Here, the total signal on the whole detector area and difference signal containing magnetic phase, electrostatic phase, amplitude effects, are alternatively calculated, as shown in the following equations,

$$\sum signal(D) = \alpha^2\pi, \tag{2.20}$$

$$\left.\begin{aligned}\sum signal(D_1) &\cong \frac{\alpha^2\pi}{2} - 2\alpha\beta_L \\ \sum signal(D_2) &\cong \frac{\alpha^2\pi}{2} + 2\alpha\beta_L\end{aligned}\right\} \Rightarrow \Delta(signal) = \sum signal(D_2 - D_1) = 4\alpha\beta_L \tag{2.21}$$

where $\Sigma signal(\mathrm{D})$ are the total signal on the whole detector, $\Sigma signal(\mathrm{D_1})$ and $\Sigma signal(\mathrm{D_2})$ are signal levels from opposite sides of the detector, segments (see Fig. 2.14(a)). $\Delta(signal)$ is the difference signal levels at opposite segments. Practically, the sum image (signal from whole detector) and split images (signal from opposite segments) can be observed simultaneously. Fig. 2.14(b) shows two split images that were taken from the opposite segments. Those images are sensitive to magnetic induction components induced by magnetization of the specimen, as indicated by red arrows.

Thus, based on equations (2.20) and (2.21), the Lorentz deflection angle can be calculated from the ratio of the difference signal and the total signal on the whole detector,

$$\frac{\Delta(signal)}{\sum signal(D)} = \frac{4\alpha\beta_L}{\pi\alpha^2}, \text{ or } \beta_L = \alpha\frac{\Delta(signal)}{\sum signal(D)}\frac{\pi}{4} \tag{2.22}$$

Here, the convergence angle is known in a particular LTEM mode, so the equation (2.22) can be used to estimate β_L directly from the DPC image signal level of the sum image and split images. As an example, BF (sum) and split images of 10nm-thick Py-nanowire with dimension of 400nm-width×10μm-length where a H2H TDW was created, are shown in Figs. 2.15(a) and (c), respectively. Fig. 2.15(b) and (d) are presented the signal profiles that were extracted from selected areas (indicated by dashed rectangular boxes) of the images in

Figs. 2.15(a) and (c), respectively. Here, the averaged total signal level was extracted from the nanowire width area in the BF image (from 50th-pixel to 110th pixel in Fig. 2.15(b)) is indicated by the horizontal green dashed-line. The signal levels in the split image which were taken from either side of the H2H-TDW are presented as horizontal red and violet dashed-lines in Fig. 2.15(d).

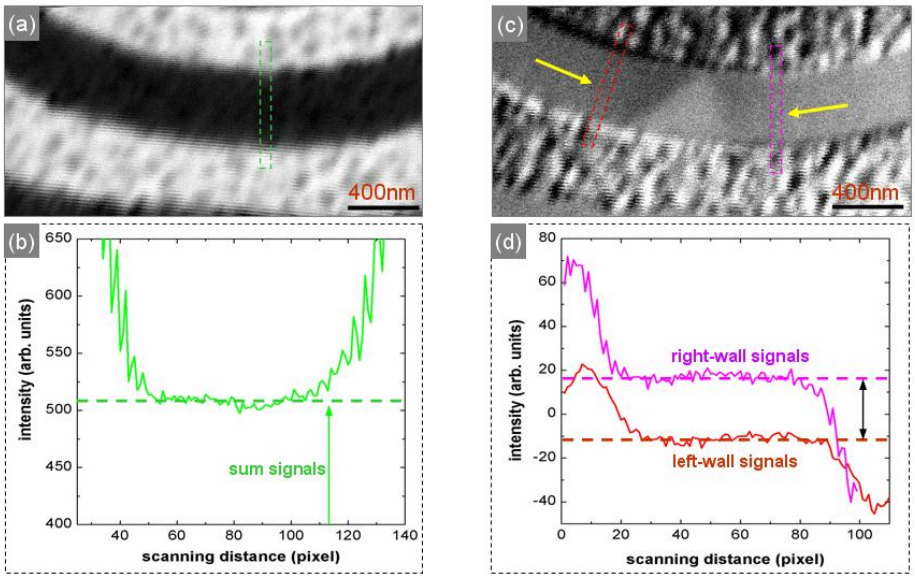

Fig. 2.15 (a) and (b) represent a BF image and its sum signal level, while (c) and (d) show a DPC image was taken from different quadrant and its signal level, respectively. Here, the green dash-bar shows the area was scanned crossing the mean width of a nanowire where the signals were summed. Moreover, the red and pink dash-bars also represent scanned areas in either sides of a H2H-TDW where the signal levels were taken from and shown as red and pink dashed-lines in the lower panels.

From those signal levels, a difference signal level is calculated by subtracting the lower signal level from the higher signal level and this difference corresponds to $2\beta_L$. The averaged signal levels of sum and split images are of 510 and 30, respectively. Assuming that convergence angle of the beam for this measurement is of 150μrad (at LMS mode), the deflected angle can be calculated from equation (2.22), $\beta_L \approx 3.5$μrad. By reason of the small β_L angle, this is due to the sample thickness (~10nm), so magnetic contrast in the DPC images will be affected in which the electron beam passed through the milled areas around the nanostructure is easily saturated. Although the DPC images in Fig. 2.14(b) and Fig. 2.15(c) are low contrast or dominated by noise, but it can be recognized a H2H or T2T magnetization either side of the TDW indicating by brighter and darker areas.

The main characterization techniques were discussed. The following sections are concerned with fabrication methods which were used to produce specimens for this project.

2.5. SPECIMEN FABRICATION

The FIB patterning method was mainly used to fabricate the patterned Py structures investigated in this thesis. The FIB technique and associated processes/routines are to be discussed in the following sections.

The Py nanowires studied here were formed in two main steps. Firstly, a continuous Py thin film was evaporated onto an electron transparent membrane by thermal evaporation. Secondly, Py nanowires were then created by FIB [12, 13] to isolate them from the continuous film. In order to prevent charging during the FIB fabrication and TEM imaging, a sputtering deposition was used to deposit a very thin conducting layer (Al or Au) of less than 10 nm in the back of the TEM membrane substrate. The charging causes major problems for imaging as electrostatic forces can cause membrane to rupture.

2.5.1 TEM membrane

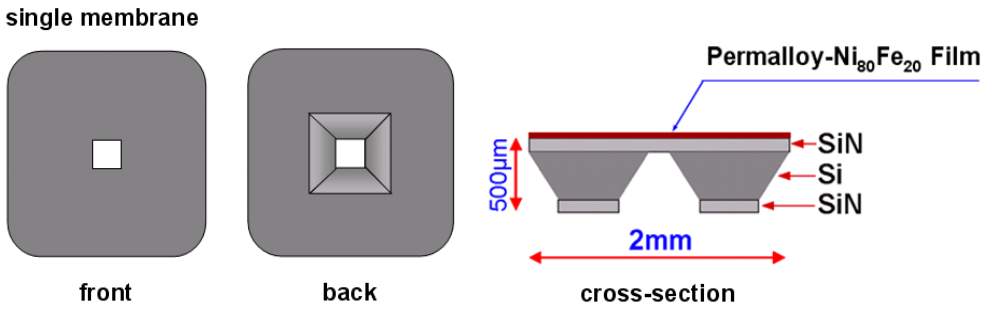

Fig. 2.16 Schematic of single membrane: front side, back-side and cross-section of a continuous permalloy thin film evaporated onto the membrane.

Most of specimens investigated here have to be suitable for TEM analysis, *i.e.* the samples must be thin enough (<100nm) for electron transparency. The specimen substrate is a 35nm-thick amorphous Si_3N_4 membrane with dimension of 100µm×100µm as a 'window' mounted on a 2mm×2mm bulk silicon frame, 500µm-thick. A schematic of a membrane is illustrated in Fig. 2.16 where the bulk silicon is etched and reached to a mask of Si_3N_4 in one side of the substrate, leaving a thin Si_3N_4 membrane on the opposite side. The figure shows back and front sides of a single membrane and a cross-section of a continuous thin

Py film evaporated onto the membrane. The continuous thin film is to be used for patterning by the FIB. Thermal evaporation was used to deposite a thin Py film onto the membrane for subsequent FIB patterning and is described in the next section.

2.5.2 Magnetic thin film evaporation

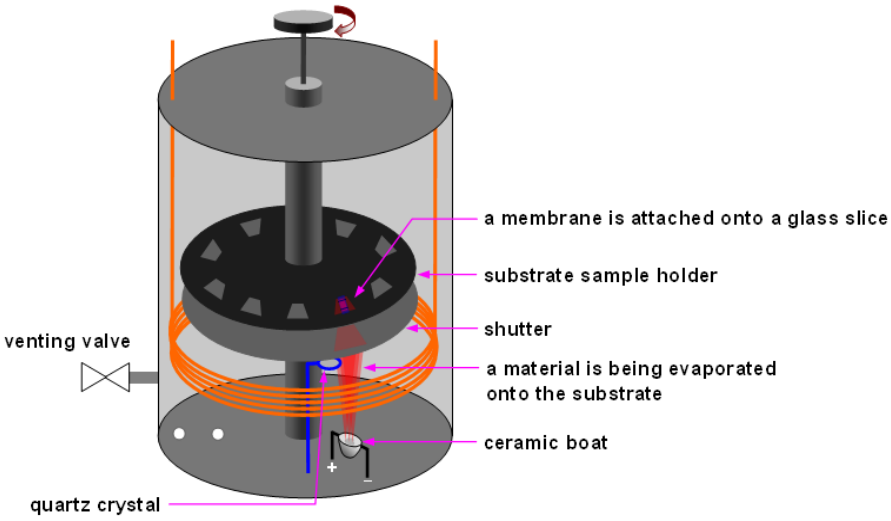

Fig. 2.17 Schematic of a thin film evaporator used in this thesis.

A schematic of a thin film evaporator used in this work is illustrated in Fig. 2.17. The evaporator consists of a high vacuum chamber housing materials which are to be evaporated and associated electrical control systems. A small quantity of the chosen material (*e.g.* permalloy-$Ni_{80}Fe_{20}$) is put into a ceramic boat surrounding by a heating filament. The material is heated to the point of evaporation by using a high DC power supply. The evaporator is able to evaporate a wide range of materials in different locations of the main chamber, and this method is suitable for materials with low melting points. The uniformity of a thin film is negatively affected by the low average kinetic energy of the evaporated atoms impinging on the specimen surface. The evaporation rate of the evaporator could reach to 0.03nm/s. The film thickness was controlled and monitored by using the quartz crystal microbalance technique which measures a correlation between mechanical oscillation and a resonant frequency. The resonance is sensitively affected by material evaporated onto or removed from the surface of the resonator. For an individual material, the vibration frequency is calibrated with thickness of the material, so that the evaporated material thickness on the substrate is indicated precisely.

2.5.3 Sputter Deposition

As mentioned in section 2.1, if depositing a conducting layer on the backside of the membranes, the charging is reduced during patterning and imaging processes, but the magnetic contrast is partly affected/ reduced by adding this polycrystalline sputtered layer. Thus, balancing those conditions, the optimal condition for patterning might be made to reducing charging and enhance the magnetic imaging contrast of the deposited sample. Sputter deposition is commonly used after the Py-thin film evaporation for producing a high quality polycrystalline Au or Al thin film in the back side of the membranes. In this project, some specimens used in the thesis have no conducting sputtered layer, however the deposition method is discussed here as a short introduction. For a deposition, the conducting target material is bombarded by energetic Argon (Ar) ions created by a glow discharge plasma process. The substrate is then exposed to form a thin film. The sputtering chamber is maintained under vacuum and consists of a cathode and an anode, as shown in Fig. 2.18. The sputtered thin film thicknesses depend on the deposition time and distance from the material target to the sample substrate.

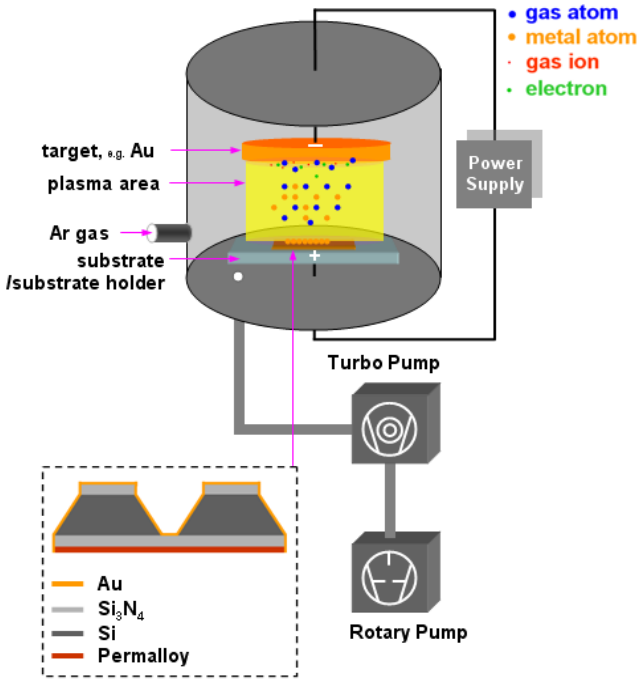

Fig. 2.18 Schematic of the sputter deposition operation and an Au thin film profile is appeared onto the back side of a membrane.

2.5.4 Focused Ion Beam: *FIB instrument*

The Focused Ion Beam system is the most common tool for milling/patterning materials in this thesis. The FIB used for this project was an FEI xT Nova NanoLab 200 DualFIB [32-34]. Technologically, the FIB system consists of a main chamber maintained under vacuum, electron and ion columns where the ion column is tilted to 52° with respect to the electron column, as shown in Fig. 2.19. Imaging and patterning resolutions are able to achieve better than 10nm and sub-100nm, respectively. This technique is not only an excellent choice as a fast route for magnetic nanostructure patterning, but also used intensively for the semiconductor and magnetic recording industries, *i.e.* TEM cross-sections, tomography volume reconstructions [32-39].

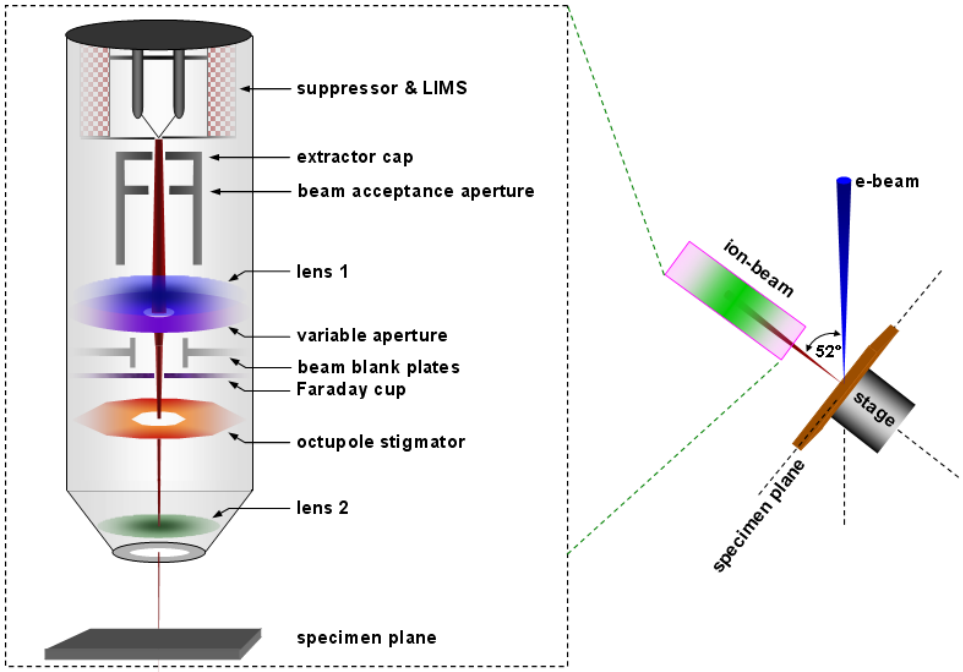

Fig. 2.19 Schematic of FIB LMIS and ion column (left) and a stage of the Glasgow FEI xT Nova NanoLab 200 SEM/FIB in a fabrication (right).

Basically, the FIB is very similar to a Scanning Electron Microscope, which can produce surface images with topographic contrast, except the beam scanned over the material surface is an ion beam. Thus, an image is formed by secondary ions or electrons, and it is detected by a polarity detector, high resolution imaging depends on electron/ion source. A Gallium Liquid Metal Ion Source (Ga^+ LMIS), as shown in the left panel of Fig. 2.19, is one of the most popular sources in FIB systems, because the source has a long

operation life (~800 hours) and high brightness. The Ga^+ LMIS consists of a Gallium reservoir and a Tungsten needle. During FIB operation, Ga^+ flows from the LMIS to the tip of the needle where Ga ions can be extracted by field emission. A strong electric field is produced at the tip of the needle by applying a high voltage to the extraction electrode. The ions are emitted from the source to the ion column under high vacuum of orders 10^{-6} mbar, this condition aims to avoid interference with atmospheric gas molecules. The ion beam column consists of two electrostatic lenses – a condenser lens and objective lens which focus the 30keV beam onto the sample plane. Current profiles are ranged from 1 pA to 2×10^4 pA with beam diameters of 6 nm to 350 nm [12, 32-34]. The beam current is chosen by the user and the beam profile (full-width-half-maximum, FWHM) which corresponds to the pixel spacing of the patterning structure to be milled/irradiated. The current profile used in the thesis is 9.7pA which corresponds to the beam diameter of 10nm. The astigmatism of the ion beam is controlled by the octupole above the second lens and the scanning motion of the beam is controlled by the deflector plates.

2.5.5 Focused Ion Beam: *FIB patterning*

Irradiation: To understand the FIB patterning process, irradiation dose definition is briefly mentioned here as an introduction before going further into a particular magnetic nanowire fabrication. The irradiation definition is quite sensitive because the irradiation dose is not a parameter that can be directly put into the FIB, so the user must control the irradiation dose parameter via a number of available other factors such as dwell time, current, ion Ga^+ charge, milled area, pixel overlap and pixel size, and this can be calculated by the equation below,

$$D = \frac{tI}{eA}, \tag{2.23}$$

where, D is dose (ions·cm^{-2}), t is dwell time (sec), I is current (nA), e is the Ga^+ ion charge, A is the milled area (μm^2). The total dwell time for a milling can be calculated as,

$$t = \frac{Ad}{IS}, \tag{2.24}$$

where, d is the milling depth of each pixel (μm), S is sputter rate (μm^3·nA^{-1}·s^{-1}). From the equations (2.23) and (2.24), an expression for irradiation dose can be obtained,

$$D = \frac{d}{eS}, \qquad (2.25)$$

It is clear that the irradiation does not directly depend on the beam current, as shown in equation (2.25). However, the total dwell time for an irradiation can be calculated, experimentally users can use longer total dwell time and multiple passes per pixel in order to obtain perfect pattern definition rather than a single pass with long dwell time [12, 32-40]. It depends on the aim of research in which users can choose an optimal condition to obtain expected results. By applying different doses onto materials, the material properties are modified/ changed, and a number of trends in research have been raised by effects of FIB irradiation. Effects of FIB irradiation on thin ferromagnetic films have been investigated by Dr. Damien McGrouther [12, 33]. In this study the ion beam is simply used to isolate nanostructres from the continuous Py thin film. Experimentally, if users want to observe each pixel in studying structures receives the same dose, a 0% pixel overlap is preferred for irradiation, or the overlap can be varied between 0% and 50% to observe smoother edge specimen profiles.

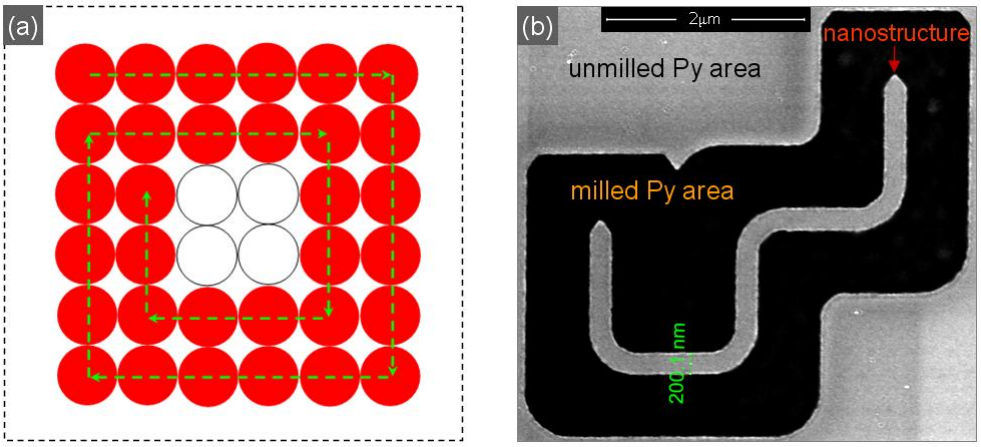

Fig. 2.20 (a) A diagram showing the path of the ion beam during a FIB patterning process using a stream file which was generated by the 'edgestream' program, assuming here that the beam has no overlap and, (b) a SEM-FIB image of a magnetic Py nanowire structure was patterned by a FIB patterning using 50% beam overlapping [12].

FIB patterning: As an example, a permalloy magnetic nanowire was fabricated using the FIB patterning/milling method. The irradiation process proceeds on the selected areas in order to modify material, whereas patterning/milling is irradiated around the area surrounding a specimen which aims to isolate from whole continuous magnetic thin film.

Now the patterning process can be generally understood as several basic steps: nanostructures are designed and then generated by ‘edgestream’ program, the ‘edgestream’ uses vector scanning strategy to trace out shape edges as depicted in Fig. 2.20(a). This program allows the pattern to be milled in several cuts/stages and/or single cut, depending on the size of the structure that will be fabricated. Thus, FIB working screen location, dwell time, sputter rate, milling depth, beam profile (the beam profile-FWHM should match the pixel size) as input parameters are defined. Also during the patterning process the FIB drifts are usually around 10nm/minute which is comparable with the patterning cell-size. Thus, to receive higher edge-profile quality, the patterning time for the first cut should be less than 1 min to avoid drift problems. The details of experimental results will be discussed intensively in the next chapter.

REFERENCES

[1]. J. Stöhr, Y.Wu, B.D. Hermsmeier, M.G. Samant, G.R. Harp, S. Koranda, D. Dunham and B. P. Tonner, Science **259** (1993) 658

[2]. A. Scholl, J. Stöhr, J. Lüning, J. W. Seo, J. Fompeyrine, H. Siegwart, J.-P. Locquet, F. Nolting, S. Anders, E. E. ullerton, M. R. Scheinfein, H. A. Padmore, *Science* **287** (2000) 1014

[3]. S.-B. Choe, Y. Acremann, A. Scholl, A. Bauer, A. Doran, J. Stöhr, H. A. Padmore, *Science* **304** (2004) 420

[4]. H. Ohldag, T. J. Regan, J. Stöhr, A. Scholl, F. Nolting, J. Lüning, C. Stamm, S. Anders and R. L. White, *Phys. Rev. Lett.* **87** (2001) 247201

[5]. H. Ohldag, A. Scholl, F. Nolting, E. Arenholz, S. Maat, A.T. Young, M. Carey and J. Stöhr, *Phys. Rev. Lett.* **91** (2003) 017203

[6]. Y. Acremann, J.P. Strachan, V. Chembrolu, S.D. Andrews, T. Tyliszczak, J. A. Katine, M. J. Carey, B. M. Clemens, H. C. Siegmann, J. Stöhr, *Phys. Rev. B* **96** (2006) 217202

[7]. D. Atkinson, D. A. Allwood, G. Xiong, M. D. Cooke, C. C. Faulkner and R. P. Cownburn, *Nature Materials* **2** (2003) 85

[8]. M. T. Bryan, D. Atkinson and R. P. Cowburn, *Appl. Phys. Lett.* **85** (2004) 3510

[9]. M. Kläui, P.-O. Jubert, R. Allenspach, A. Bischof, J. A. C. Bland, G. Faini, U. Rüdiger, C. A. F. Vaz, L. Vila and C. Vouille, *Phys. Rev. Lett.* **95** (2005) 026601

[10]. M. Kläui, C.A.F. Vaz, J. A. C. Bland, W. Wernsdorfer, G. Faini, E. Cambril, L. J. Heyderman, F. Nolting and U. Rüdiger, *Phys. Rev. Lett.* **94** (2005) 106601

[11]. J.N. Chapman, *J. Phys. D: Appl. Phys.* **17** (1984) 623

[12]. D. McGrouther, PhD Thesis: *Effects of Focused Ion Beam Irradiation on Thin Ferromagnetic Films* (2004) 44-46 and 261-265

[13]. K. O'Shea, PhD Thesis: *Putting a leash on the domain wall*: *A TEM investigation into the controlled behaviour of domain walls in ferromagnetic nanostructures: (2010*) 49-58

[14]. E. Ruska, *Rev. Mod. Phys*. **59** (1987) 627

[15]. L. D. Landau and E. M. Lifshitz, *Statistical Physics: Quantum Electrodynamics*, Part 1-Course of Theoretical Physics, Vol.5

[16]. D.B. Williams and C. B. Carter, *Transmission Electron Microscopy*: *A Textbook for Materials Science*, © Springer Science and Business Media, LLC 2009 NY 10013, USA

[17]. J.N. Chapman, A.B. Johnston, L.J. Heyderman, S. Mcvitie, W.A.P. Nicholson and B. Bormans, *IEEE Trans. Magn.* **30** (1994) 383

[18]. M. Born and E. Wolf, *Prinsiples of Optics*, Oxford: Pergamon (1975) 419

[19]. M. Mansuripur, *J. Appl. Phys.* **69** (1991) 2455

[20]. J.N. Chapman and M. R. Scheinfein, *J. Magn. Magn. Mater.* **200** (1999) 729

[21]. P.D. Nellist and S.J. Pennycook, *Adv. Imag. & Elec. Phys.* **113** (2000) 147

[22]. Y. Aharonov and D. Bohm, *Phys. Rev.* **115** (1959) 485

[23]. S. McVitie and M. Cushley, *Ultramicroscopy* **106** (2006) 423

[24]. S. McVitie and G. S. White, *J. Phys. D: Appl. Phys.* **37** (2004) 280

[25]. M. Tanase and A.K. Petford-Long, *Micr. Res. & Tech.* **72** (2009) 187

[26]. L. Reimer, *Transmission Electron Microscopy*: *Physics of Image Formation and Microanalysis*, Springer-Verlag (1984)

[27]. J.N. Chapman, R. Ploessl and D. M. Donnet, *Ultramicroscopy* **47** (1992) 331

[28]. M.Beleggia, M.A.Schofield, V.V.Volkov, Y.Zhu, *Ultramicroscopy* **102** (2004) 37

[29]. P. Donnadieu, M. Verdier, G. Berthomé, P. Mur, *Ultramicroscopy* **100** (2004) 79

[30]. D. Paganin and K. A. Nugent, *Phys. Rev. Lett.* **80** (1998) 2586

[31]. B. Khamsehpour, C. D. W. Wilkinson, J. N. Chapman and A. B. Johnston, *J. Vac. Sci. Technol. B* **14** (1996) 3361

[32]. XT Nova NanoLab User Manual 4022 262 52351

[33]. D. McGrouther, W.A.P. Nicholson, J.N. Chapman, S. McVitie, *J. Phys. D: Appl. Phys.* **38** (2005) 3348

[34]. J. Fassbender and J. McCord, *J. Magn. Magn. Mater.*, **320** (2008) R579

[35]. C.A. Volkert and A.M. Minor, *MRS Bulletin* **32** (2007) 389

[36]. R. M. Langford, P. M. Nellen, J. Gierak, Y. Q. Fu, *MRS Bulletin* **32** (2007) 417

[37]. M. D. Uchic, L. Holzer, B. J. Inkson, E. L. Principe, P. Munroe, *MRS Bulletin* **32** (2007) 408

[38]. J. Mayer, L. A. Giannuzzi, T. Kamino, J. Michael, *MRS Bulletin* **32** (2007) 400

[39]. W. J. MoberlyChan, D. P. Adams, M. J. Aziz, G. Hobler and T. Schenkel, *MRS Bulletin* **32** (2007) 424.

[40]. G. Xiong, D. A. Allwood, M. D. Cooke and R. P. Cowburn, *Appl. Phys. Lett.* **79** (2001) 3461.

Chapter 3

Characterization of the Degree of Asymmetry in Transverse Domain Walls

3.1. INTRODUCTION

Understanding domain wall behaviour in permalloy nanowires is important for the success of potential applications such as the magnetic racetrack memory [1] described in chapter 1, a number of magnetic storage class memory technologies and magnetic logic gates [2-4] and also provides an insight into their fundamental properties [5, 6]. In the racetrack memory scheme, each magnetic domain can be considered as a 'bit' of information, additionally the domain wall itself can be considered as dynamic entity that can be moved along the ferromagnetic nanowire by a spin-polarized current or a magnetic field [1-7]. Interestingly, when the width and thickness of a particular permalloy nanowire are scaled down to the nanoscale, a number of features are observed and especially related to domain wall behaviour. Furthermore, the detailed creation and motion of these DWs driven by magnetic field/spins-polarized current in different geometries are of great interest. Three types of domain walls, namely symmetric transverse domain walls (STDWs), asymmetric transverse domain walls (ATDWs) and vortex domain walls (VDWs), are found to exist in permalloy nanowires where the shape anisotropy of the structure is dominant, leading to domain wall configurations that depend strongly on the width and thickness of the wire [1-9]. If the wire geometry is locally modified, the energy landscape is also altered, thus allowing more complex domain wall behaviour to form. Fig. 3.1 shows a phase diagram of stable DW structures for Py nanowires of varying width and thickness as simulated by OOMMF simulations (see chapter 1), reproduced from ref. [7]. However, the experimental results of 'non-straight' nanowires were recently shown to be different from the above calculations [9-11]. In those results, local defects and wire geometries strongly influenced the domain wall configurations. This means the behaviour of each wall type can be different in different wire geometries. Whilst there is a lot of work on domain walls in nanowires, often the nature of the wall type is not observed directly. Imaging of the DWs is important in determining their behaviour during motion and how they interact with defects.

Obviously the simulated diagram does not apply for all cases with different structural geometries, but it does present the most stable domain wall structures for straight (perfect) wires. The differences between the above experimental and simulation results are due to imperfect edges (edge roughness) [5] of the nanowires in which the edge roughness constitutes local defects or pinning sites and the pinning sites on the edges create different potential energy levels. The differences in the energy potential levels at the edges will affect the domain wall configurations when they reach to stable or meta-stable states [5]. So, if a DW is created in a nanowire, the DW configuration is not only determined by intrinsic behaviour (*i.e.* magnetic moment components), but also by extrinsic behaviour (*i.e.* nanowire edge roughness or structural geometries). Therefore, quantifying of the DW configurations, *i.e.* asymmetric TDWs, the role of the edge roughness in nanowires may be understood. Indeed, this chapter presents significant observations of both simulated and experimental results by means of a Lorentz microscopy study which should be added into the DW phase diagram [7] based on imperfect nanowires where symmetric and asymmetric TDWs are concerned.

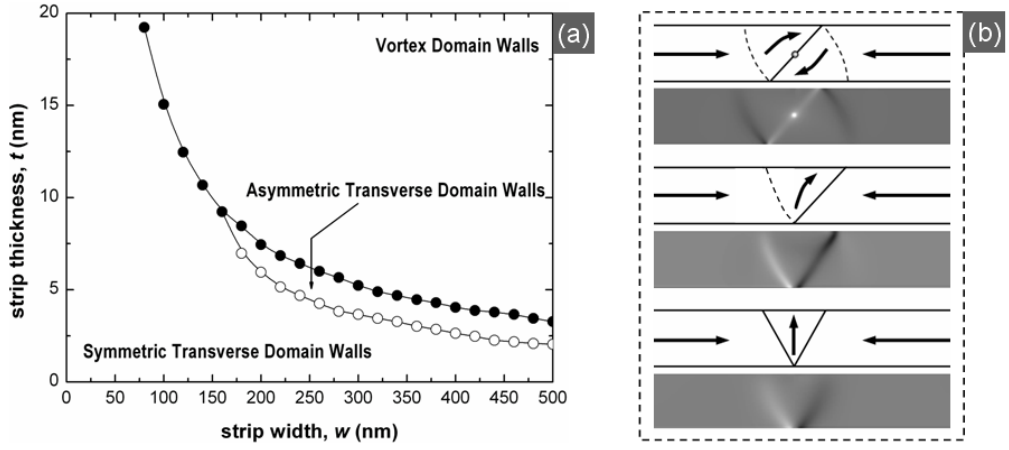

Fig. 3.1 (a) Phase diagram for DW configurations in straight Py nanowires/ strips, reproduced from ref. [7]. (b) Simulated Fresnel LTEM images and schematics of vortex, asymmetric and symmetric transverse domain walls [from the top downward], the stable DW configurations found in straight wires of dimensions 2500nm×300nm, 19.5nm, 5nm and 3nm-thick, respectively.

The simulated phase diagram of Fig. 3.1 raises a number of open questions, for instance, if a TDW is defined as a method suggested in Fig. 1.10(f), then, are there any

relationships between geometrical asymmetry (related to areas inside the TDW) and magnetization components (M_x, M_y) which constitute magnetic structure of the TDW in the nanowire? These questions are answered experimentally in this chapter.

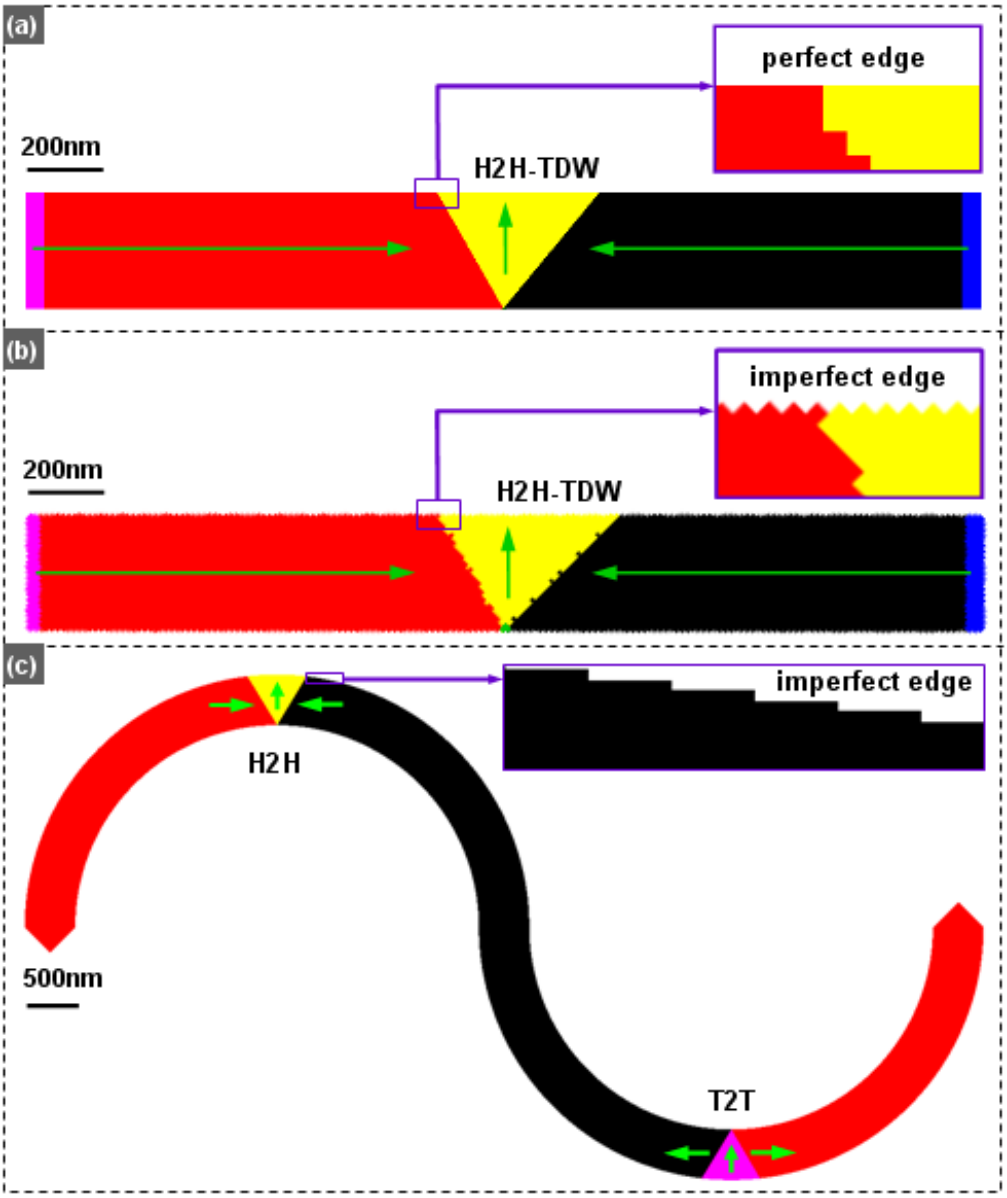

Fig. 3.2 (a) is schematic of a straight nanowire with dimension of 300nm-width×2500nm-length at the starting state of an OOMMF simulation, (b) Another 300nm-width nanowire which was rotated at 45° (regular staircase edge behaviour) prior to simulation in order to understand effects of edge roughness and (c) is an initial state of 500nm-width curved nanowire (irregular staircase edge behaviour, similar to the nanowire studied experimentally) containing head-to-head (H2H) and tail-to-tail (T2T) TDWs. Green arrows indicate the magnetization directions which were defined in each simulation.

To understand the degree of asymmetry/symmetry of TDWs, straight Py-2500nm-length-nanowires of different widths (from 76 nm to 548 nm, in 24 nm steps) and thicknesses (from 1.5 nm to 21 nm, in 1.5 nm steps) were designed and simulated. Here, all structures were assumed to be structurally perfect at the long edges of the structures (wires aligned to grid of cells in OOMMF simulation) and the initial state was taken to be a TDW at the middle point along the length, for example, a 300nm-width straight nanowire is illustrated in Fig. 3.2(a) and its edge roughness behaviour is shown in the insert. Following that, a series of 300nm wide nanowires with a thickness of 10.5 nm were rotated at certain angles (±10º, ±30º and ±45º) and then simulated. Here, edge roughness of rotated nanowires was raised by pixellation effects under rotation process and depending on orientation of straight edge at a certain rotation angle relative to grid of cells. This aims to introduce straight nanowire with different edge roughness behaviour because the edge roughness usually occurs in rotated or curved designed-nanostructures and experimental specimens. Here, a particular example is shown in Fig. 3.2(b) where a 300nm wide straight nanowire is rotated to -45° (clockwise) and the edge roughness of the structure can be seen in the inset of Fig. 3.2(b) as regular staircase behaviour. Finally, a set of 10.5 nm-thick curved nanowires of differing widths are to be considered, *i.e.* a 500nm wide curved nanowire at the initial state is depicted in Fig. 3.2(c). This aims to create non-straight nanowires with uneven edge behaviour and suitable for experimental performances with H2H and T2T DWs can be created simultaneously. One can see that outer-edge roughness of the curved nanowires near the initial H2H TDW location (indicated in figure) is shown in the inset of Fig.3.2(c) as irregular/ uneven staircase behaviour. Hence, the above nanowires with different edge roughness behaviour at the initial states for OOMM simulation were alternatively created. This aims to study how the degree of edge roughness affects DW configurations which are created in those structures. By studying DW configuration behaviour, the role of edge roughness on each type of structure (from perfect structures to structures with uneven edge roughness behaviour) can be explored.

3.2. TDWS IN STRAIGHT NANOWIRES: SIMULATION RESULTS

The purpose of this section is to explore a correlation between the ratio of magnetization components (*i.e.* M_x and M_y, the in-plane magnetization components) and

areas of regions inside a TDW which related to intrinsic and extrinsic behaviour of each DW configuration. As an example, Figs. 3.3(a) and (b) show simulated Fresnel images of STDW and ATDW in 300nm-width nanowire with thicknesses of 4.5nm and 19.5 nm, respectively. In those images, the area inside the TDW is divided into two areas of regions (A_1 and A_2) by a straight line which comes from the TDW intersection and is perpendicular to the long edges of the wire. A parameter is then defined by subtracting the smaller area (A_1) from the bigger one (A_2). Subsequently, if A_1 is equal to A_2 (A_2-A_1=0), a symmetric TDW is observed and, if A_1 is not equal to A_2, we have an asymmetric TDW. This is interesting because if the correlation exists, a new route map of transformation between asymmetric and asymmetric TDWs can be introduced as a direct symmetric/ asymmetric TDW observation method. As mentioned above, the parameter defined by subtracting the smaller area from the bigger one is an extrinsic behavior and experimentally characterized, whereas the ratio of magnetization components is a intrinsic behavior and difficult to measure experimentally. It means that this chapter is purely focused on the transition points of the phase diagram for the symmetric and asymmetric TDWs.

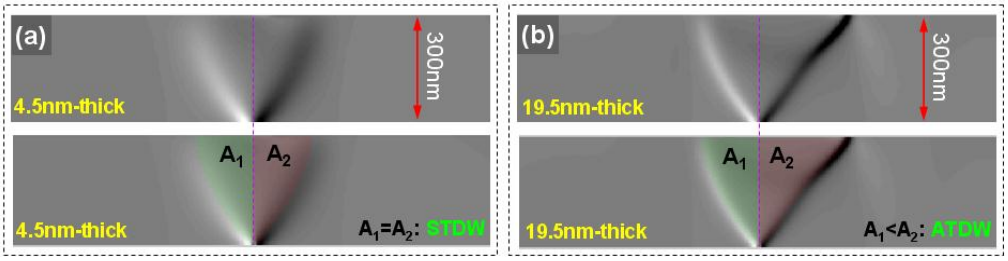

Fig. 3.3 Simulated Fresnel images of (a) a STDW and (b) an ATDW in a 300nm-width straight nanowire with thickness of 4.5nm and 19.5nm, respectively: Here, the lower panels show demonstrations of area calculations inside the DWs (A_1 and A_2), in which the two halves are defined by intensity profiles of the simulated Fresnel image as white and dark bands and the perpendicular bisector of the wire positioned at the TDW apex.

3.2.1 Initial states of OOMMF simulations

Returning to the schematic of the 300nm-width straight nanowire at the initiation state given in Fig. 3.2(a), one can be seen that the straight nanowire consists of a head-to-head (H2H) domain wall and the ends of the element are two regimes overlayered by pink and blue colour which are artificially pinned to avoid domain wall propagation or annihilation

during relaxation processes of the simulation. Moreover, a small protrusion, a so-called anti-notch [10], with dimension of 2×1pixel (8×4nm^2) is attached to one side of the element at the middle point along the length in order to pin a domain wall when it is created. The anti-notch acts as a potential well [1, 6, 10, 11] and pins the DW, preventing lateral wandering along the wire. As a result, the domain wall quickly reaches a metastable/ stable state (relaxation state). There is no difference between the relaxation states of straight nanowires with the same width and thickness if the initiation state is either a symmetric or asymmetric TDW, evidently shown in Fig. 3.4. Thus, all initial states contain asymmetric TWs over the whole of geometry range are to be considered. Simulation results are presented in sections below.

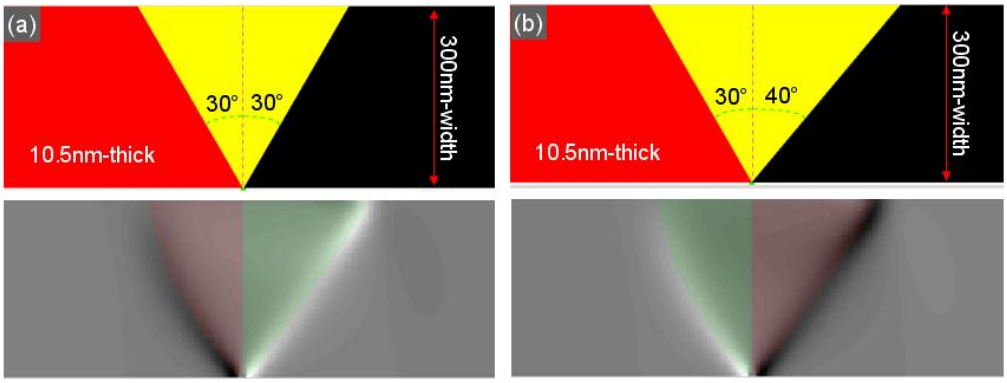

Fig. 3.4 shows schematics of a straight nanowire at different starting states of OOMMF simulations (upper panels) and their simulated Fresnel images (lower panels): the starting states of simulations were used as an isosceles triangle with 60°-apex (a) and a triangle with 70°-apex (b), respectively. There is no main difference between the relaxation states of TDWs, a minor difference is that one TDW orientation is horizontally flipped to be the other one.

3.2.2 From Lorentz images to MatLab calculations

Straight nanowires of different widths and thicknesses were simulated using the OOMMF package [8] as described in chapter 1. The simulations were performed with thicknesses and widths in the ranges of 1.5-21nm and 76-548nm, respectively, and a cell-size of 4nm×4nm×t where t is the thickness. This was chosen because TDW configurations are changed if either the wire thickness or wire width is varied, as shown in Fig. 3.1(a). The initial states of the simulations all contained asymmetric transverse domain walls (see Fig. 3.2(a) and Fig. 3.3(b)), and spins in the anti-notch were artificially pinned in the direction

perpendicular to the easy-axis, so as to pin a DW more stronger at the anti-notch area, without effecting the final DW configuration. The role of spin configurations at the anti-notch will be discussed later on. For each simulation, the magnetic structure was relaxed to observe the stable (or metastable) DW configuration. As discussed below, later simulations also incorporated edge roughness in order to see how the DW configurations were perturbed.

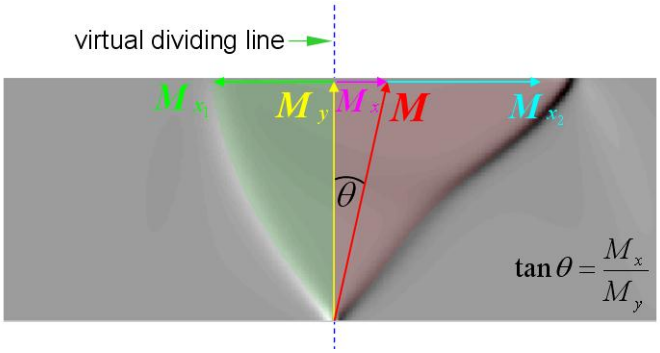

Fig. 3.5 presents a simulated image of 500nm wide-21nm-thick straight nanowire. Here, a demonstration of MatLab calculation in the 500nm-width nanowire where big and small halves of the TDW are overlayed by red and green backgrounds. Magnetization components existing in each area are also presented.

Regarding a Fresnel image where the magnetization components which contribute to the image are now concerned. As a result from the simulation, the OOMMF output can be separated into the magnetization components M_x, M_y and M_z, Fresnel images were then calculated from the equation (2.10) that was mentioned in chapter 2. In this equation, the Fresnel image intensity is proportional to $curl(\boldsymbol{M})_z$ (out of plane) in linear regime [12]. Since, the M_z component does not contribute to the simulated Fresnel intensity profile (the Lorentz deflection is zero for $\boldsymbol{M}_z$//beam). Only the M_x and M_y magnetization components need to be considered, and the Fresnel image intensity becomes proportional to

$$\left(\nabla \times \boldsymbol{M}\right)_z = \frac{\partial M_x}{\partial y} - \frac{\partial M_y}{\partial x}, \qquad (3.1)$$

Based on equation (3.1), MatLab software was used to calculate the areas of the two halves of the TDW and magnetization components inside the TDW directly from the magnetization components produced by OOMMF. A simulated Fresnel image of a 500nm-width, 21nm-thick straight nanowire is shown in Figs. 3.5 where areas inside the TDW are highlighted as green and red regimes. In this image, $\boldsymbol{M}_{x1}$ and $\boldsymbol{M}_{x2}$ are defined as

magnetization vectors within the small and large halves of the TDW, respectively and the total $\boldsymbol{M}_x$ is the sum of $\boldsymbol{M}_{x1}$ and $\boldsymbol{M}_{x2}$ in which $\boldsymbol{M}_{x1}$ and $\boldsymbol{M}_{x2}$ are usually in opposite direction. In the case where M_x is non-zero, the $\boldsymbol{M}_x$ intends to circulate the $\boldsymbol{M}_y$ inside the TDW into one side of the virtual dividing line and this makes an asymmetric TDW. The total magnetization inside the TDW, $\boldsymbol{M}$, is the vector sum of $\boldsymbol{M}_x$ and $\boldsymbol{M}_{y.}$ Thus, if $\boldsymbol{M}_{x1}$ and $\boldsymbol{M}_{x2}$ are equal in magnitude and opposite in direction then the TDW is symmetric despite of the M_y magnitude and the degree of asymmetry is defined by the net $\boldsymbol{M}_x$. The angle, θ, between the total magnetization and the virtual dividing line is calculated through a relation, $tan\theta=M_x/M_y$. Moreover, to allow comparison of nanowires of different widths the subtraction values of the bigger area for smaller area inside the TDW were normalized by the wire width. Simulation results are discussed in the next section.

3.2.3 Degree of Asymmetry in Transverse Domain Wall: A correlation between magnetization components and areas inside TDWs

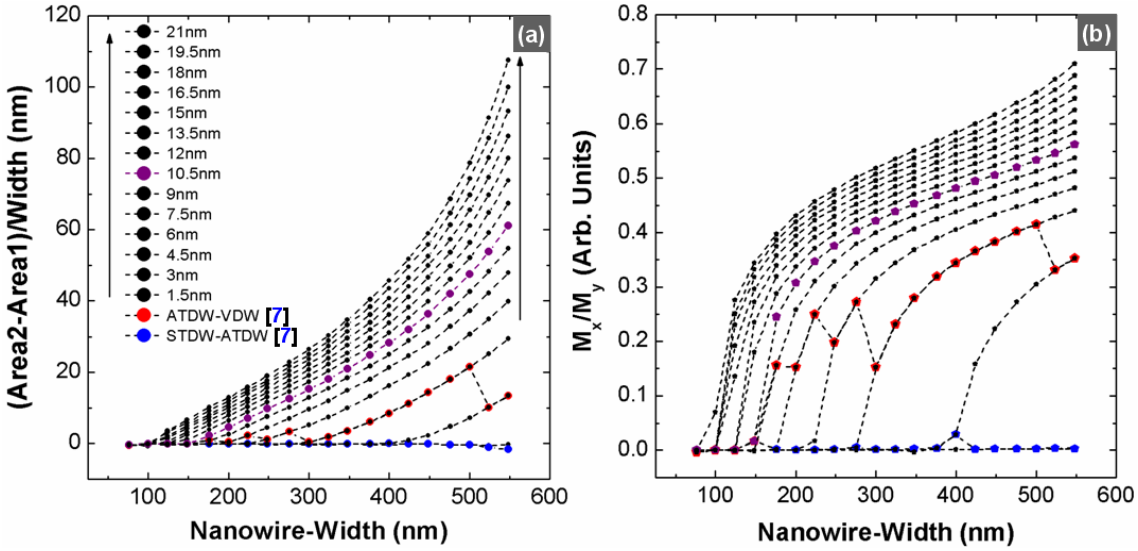

Fig. 3.6 Wall phase diagram of symmetric-asymmetric TDWs of simulated straight-nanowires in differing widths and thicknesses: (a) is normalized degree of asymmetry in TDWs in variations of nanowire-widths and thicknesses; (b) is ratio of magnetization components (M_x, M_y) as a function of nanowire-widths. The red and blue symbols are presented the transition points of VDW↔ATDW and ATDW↔STDW, respectively, the results are taken from ref. [7], in which the STDW, ATDW and VDW were defined based on their ground states. The violet symbols are presented a particular nanowire with 10.5nm-thick which will be considered extensively in this thesis.

The method calculation of degree of asymmetry TDW was mentioned above. A series of simulated TDWs in straight nanowires with different widths and thicknesses were calculated for both areas and magnetization components inside TDWs. Ratios of magnetization components M_x and M_y, and normalized degree of asymmetry in TDW are plotted for all structures in different widths and thicknesses, as shown in Fig. 3.6. The transition points between STDWs and ATDWs (denoted as STDWs↔ATDWs), observed by Nakatani *et. al.* [7], are plotted for a comparison. In particular, the transition points between ATDWs and VDWs (denoted as ATDW↔VDWs) from ref. [7] are also plotted.

As presented in Figs. 3.6(a) and (b), the normalized degree of asymmetry and the ratio of magnetization components of transverse domain walls were simulated in wires of different widths and thicknesses, respectively, which are called wall phase diagrams. Briefly, if the areas of the two halves are equal then the normalized degree of asymmetry is equal to zero, the ratio of the magnetization components (M_x, M_y) is also equal to zero and a STDW is observed otherwise we have an ATDW. By this way, transition points are defined as either M_x/M_y or normalized degree of asymmetry values is equal to zero. Here, it may be seen that the trends in the two wall phase diagrams are similar, but the transition points are in good agreement for all structures of different widths. Increasing the nanowire widths and thicknesses, normalized degree of asymmetry values slowly increase, while the ratios of magnetization components abruptly increase at directly above the transition points which indicate on the diagram. This small difference has two possible sources: firstly it might be caused by the calculation definitions for those curves where the areas inside the TDW are calculated by summing all pixels within the polynomial fittings of maximum and minimum intensities at two wall edges, while the M_x and M_y components are summed inside TDW but some pixels near the two walls were rounded. Secondly, the function describes the ratio of M_x and M_y as mathematically different in comparison to the function that represents the degree of asymmetric TDW via the inside areas. Even so, the trends of the curves reflect the simulated domain wall configurations in the straight nanowires. Particularly, for nanowires with the same thickness, if increasing in the nanowire-width the trend of degree of asymmetry in TDWs plateaus at middle-widths regime where the wall edges in the larger areas are abruptly bent at some points within the two ends of the wall edges, as shown in

Fig. 3.7(a) and inset of Fig. 3.7(b). Quantitatively, one can see the trends of the larger and smaller areas inside TDWs as a function of nanowire-widths are shown in Fig. 3.7(b). Here, the smaller areas increase relative slowly, while the bigger areas increase more rapidly. Moreover, the violet points of the wall phase diagrams are presented results of 10.5nm-thick-straight-nanowires of different widths. These relate to and will be compared with curved nanowires in later sections of this chapter where the degree of asymmetry in TDWs (DoATDWs, units in nm) was experimentally characterized and from that the effect of edge roughness may be exposed quantitatively.

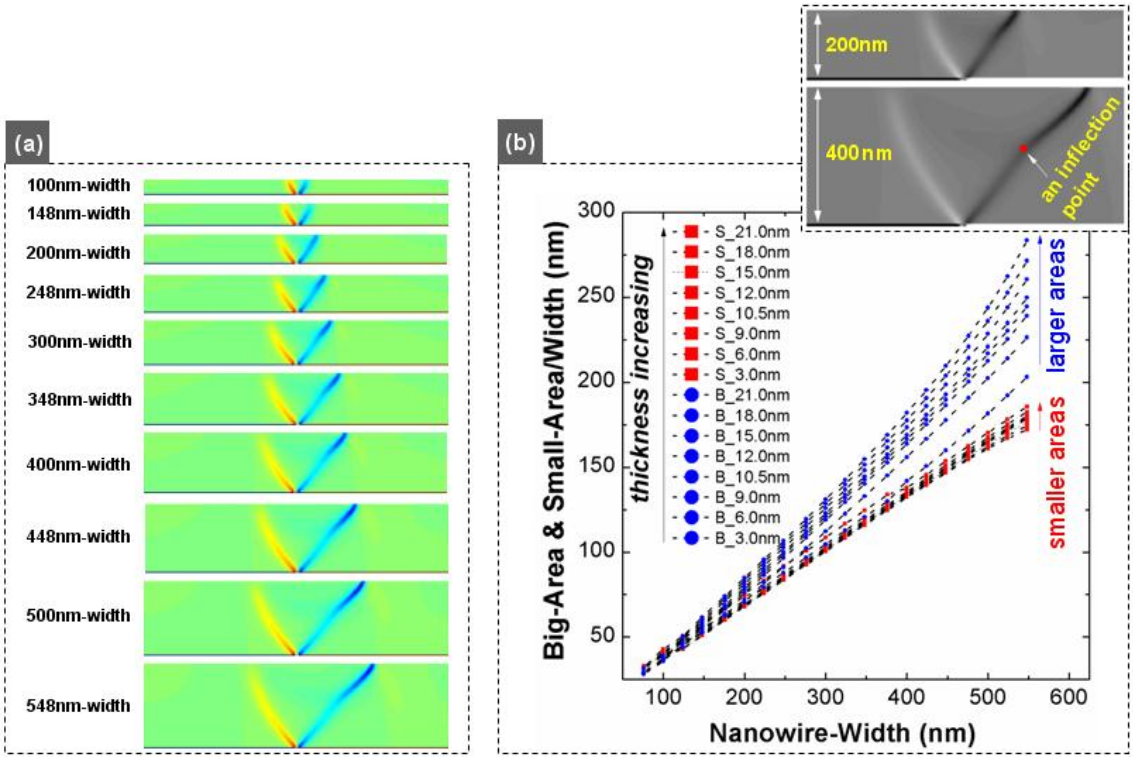

Fig. 3.7 Selected colour simulated Fresnel images of 10.5nm-thick nanowires of different widths (a), with the normalized values of the two areas inside TDWs (b). Here, the smaller areas (blue-circle-symbols) increase more slowly with increasing widths, than larger areas (red-square-symbols). The inset of (b) shows two simulated Fresnel images of 200nm and 400nm wide nanowires with 21 nm-thick which indicates the right-wall-edge is inflected at a point if nanowire width is increased.

Hence, in the wall phase diagram the boundary between symmetric and asymmetric TDWs is distinguished by the points of the normalized degree of asymmetry values being equal to zero, confirmed by the results reported by the authors in ref. [7], blue-points in

Fig.3.6. In addition, the results of boundary between asymmetric TDWs and VDWs reported in ref. [7] are also plotted as red points in the wall phase diagrams. However, it does not mean that all above the red points in the wall phase diagram, those domain walls are vortex domain walls because the initial states were all defined as TDWs, then simulated TDWs could be reached metastable states. Thus, as a short conclusion for this part, two wall phase diagrams for straight-nanowires were investigated by means of Fresnel image simulations and MatLab calculations. Interestingly the normalized degree of asymmetry values was measured quantitatively. Indeed, this simulation investigation is not only observed the transition between STDWs and ATDWs via either quantitative measurements of areas and magnetization components inside TDWs, it is also to be used to calculate any TDWs quantitatively in experiments, in particular refer to subsequent sections. Thus, as the merits of these two approaches, they are able to quantify degree of symmetry and asymmetry of TDWs via a measurement of areas inside a TDW experimentally. The result of the area measurement is also correlated to the magnetization components which were build up the magnetic structures of a TDW and difficult to quantify directly from experiments. Obviously, the correlation between intrinsic (magnetization) and extrinsic (geometrical areas) behaviour is occurred. The wall phase diagram of STDW-ATDWs are discussed more detail as followings.

3.2.4 Effects of spin configurations at the anti-notch in straight nanowires

All of the simulated structures described so far have a geometric protrusion or ‘anti-notch’ at the edge of the wire to pin the DW position. This contrasts with previous work [7] where different calculation’s wall motion was not a problem. Here, we find the details of the role of the anti-notch in our situation. Now the role of the anti-notch and effects of edge roughness are to be discussed here. For the initial purposes of this study, the chosen anti-notch size is small, 2×1pixel ($8\times4nm^2$), *i.e.* this is much smaller than the dimension of the simulated structures. When the domain wall is created, the anti-notch pins the DW at the physical center of the notch, but also reaches the stable state faster than in the case without the anti-notch, because creating a protrusion in the long axis of nanowires is similar to creating a potential well locally in the energy landscape of the nanowire [10, 11]. Clearly,

the anti-notch size geometry on spin structure affects the domain wall configuration [1, 4, 6, 10, 13]. This work does not explore the effect of the anti-notch height but will explore the effect of different spin states in the anti-notch on the DW pinning.

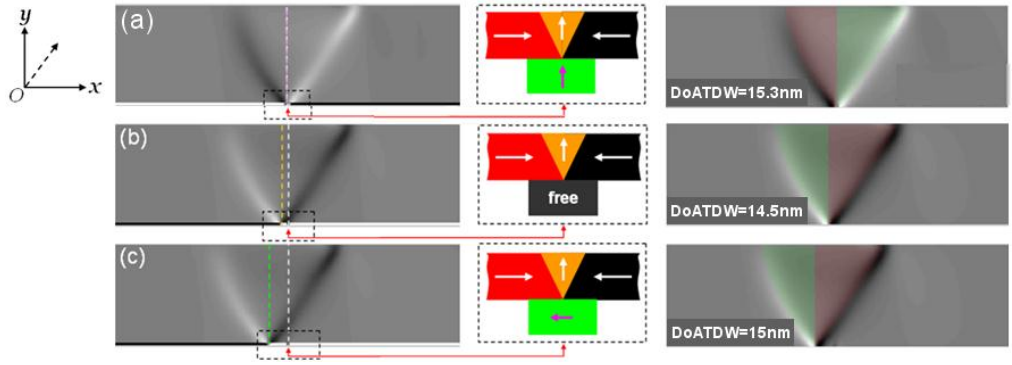

Fig. 3.8 Degree of transverse domain displacement in different spin configurations at the anti-notch of 10.5nm-thick straight nanowire with dimension of 300nm-width×2500nm-length: the DW displacements from the anti-notch are 0 nm, 24nm and 56 nm which correspond to the spins are pinned along (a) +Oy-direction [↑], (b) free and (c) -Ox direction [←], respectively. The displacements and spin configurations (at the anti-notch) of these DW configurations are different however the degree of asymmetry values is mostly similar.

Fig. 3.8 illustrates three different TDW structures resulting from cases in which the magnetization in the anti-notch is free or pinned in different directions (see the magnified images of the anti-notch regimes in the middle panels of Fig. 3.8). Here, the degree of TDW displacement for different spin orientations in the anti-notch is presented. In the case of the magnetization being artificially pinned along +Oy-direction [↑], the transverse domain wall is strongly pinned in the physical center of the anti-notch: domain wall displacement is 0 nm, see Fig.3.8 (a). For the other cases, Figs. 3.8 (b) and (c), the domain walls were displaced away from the centre of the anti-notch, 24 nm and 56 nm for the case where the spins are free and pinned in –Ox-direction [←], respectively. One can see that the role of the spin orientations in the anti-notch strongly affects the domain wall displacement from the anti-notch but has a negligible effect on the degree of asymmetry as the values of asymmetry are shown in the right-hand-panel. With the chosen +Oy[↑]-pinned-anti-notch, it does not affect the results of all simulations. The reason for choosing the [↑]-pinned-anti-notch is only to make sure that created-TDWs are always in the centre of the nanowire thus simplifying the MatLab calculations.

3.2.5 Effects of edge roughness into degree of asymmetry in TDW

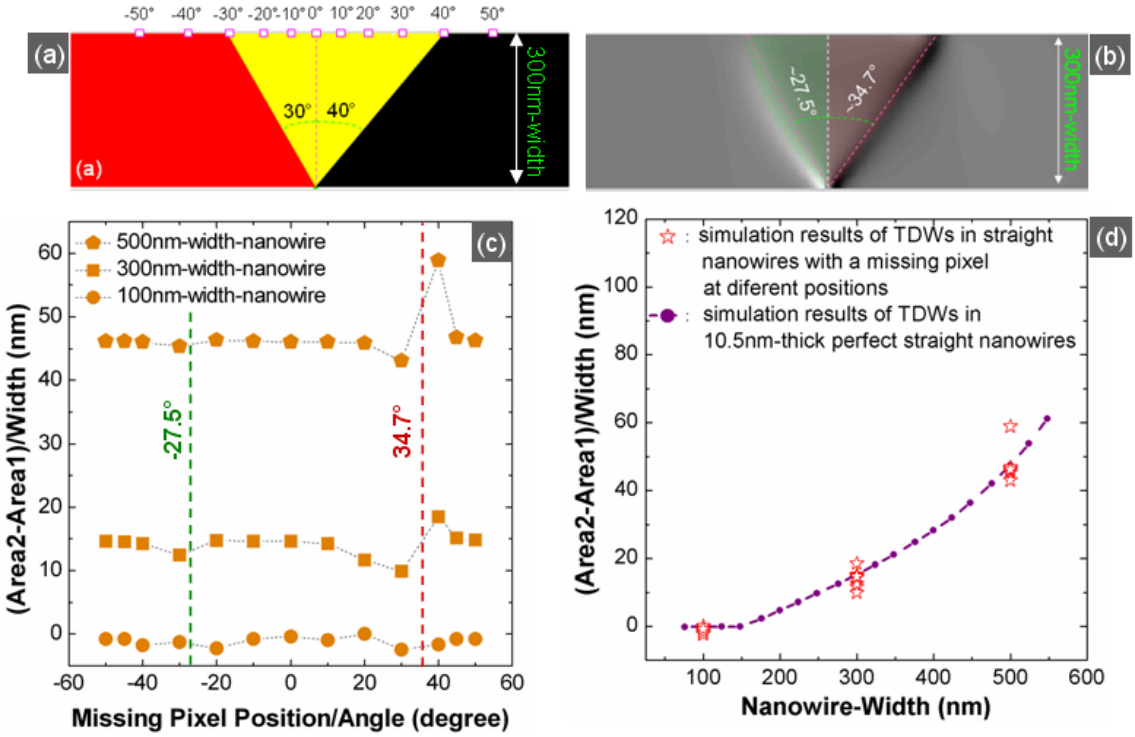

Fig. 3.9 (a) A missing pixel was created at different positions along the long edge of the 300nm-width-straight-10.5nm-thick nanowire where the initial state of the simulation is a triangle which a vertex at the anti-notch is virtually divided into 30° and 40° angles. (b) A Fresnel image of the 300nm-width perfect nanowire at the relaxed state where two natural wall edges are occurred at ~27.5° and ~34.7° in either sides of the dividing line, respectively. (c) Normalized degree of asymmetry as a function of missing pixel positions/angles for 100nm, 300nm and 500nm-width straight-nanowires and green- and red-dash lines indicate the two natural wall edges. (d) The results of normalized degree of asymmetry for 100nm, 300nm and 500nm-width nanowires with a missing pixel (red stars) which were added into the wall phase diagram of 10.5nm-thick-perfect straight nanowires in different widths (violet line).

As discussed in the previous sections, the simulations were undertaken in which the structures were assumed as perfect nanowires. In reality, the domain wall configuration is known to be affected by edge roughness [1, 4, 5]. To understand how the edge roughness of the nanowire affects the degree of asymmetry in a TDW quantitatively, a missing pixel was created in the long edge of three 10.5nm-thick-nanowires with nanowire-widths of 100nm, 300nm and 500nm, and the missing pixel locates in the other side of the anti-notch. This aims to investigate how local potential energy created by the missing pixel affecting to

degree of asymmetry in TDWs. The missing pixel is positioned at angle about the virtual dividing line in the initial state of the TDW, as depicted in Fig. 3.9(a). The initial state of the TDW was created as a triangle with an angle located in the anti-notch of 70°. So, this vertex of the triangle is virtually divided into two-sub-angles of 30° and 40° by the virtual dividing line starting from the centre of the anti-notch. The positions of the missing pixels with regards to the angles in the left and the right of the dividing-line are defined as negative and positive angles, respectively. This also aimed to explore which side of a TDW is affected strongly by the missing pixel or the local potential energy. Fig.3.9(b) shows a Fresnel image of the 300nm-width perfect nanowire with thickness 10.5 nm at the relaxed state where two natural wall edges of the TDW are occurred at ~27.5° and 34.7° either sides of the dividing line, respectively. Fig. 3.9(c) shows results on the degree of asymmetry of TDWs as a function of the missing pixel positions/angles for 100nm, 300nm and 500nm-width-nanowires. One can see that the degree of asymmetry is only affected when the missing pixel is located near the two wall edges of the TDW. In the 100nm-width-nanowire, created TDWs are symmetric, so effects of the missing pixel are equal in both sides of the dividing line (±30°), while created TDWs in the 300nm and 500nm-width-nanowires are affected strongly in the right-hand-wall-edges at 40°. Besides, if the missing pixel positions are far from two natural wall edges of TDW (two wall edges at the relaxation states) the variations in degree of asymmetry are negligible. The above results can be understood that either side of wall edges which locates near the missing pixel, they will be influenced by the local potential energy generated by the missing pixel. This is non-linear effect and makes the trend in degree of asymmetry is spread out as shown in Fig. 3.9(d) for a comparison. One can see in Fig. 3.9(d), the results of normalized degree of asymmetry for 100nm, 300nm and 500 nm wide nanowires with a missing pixel which were added into the wall phase diagram of 10.5nm-thick straight nanowires of different widths with perfect edges. Obviously, the trend in degree of asymmetry is largely varied in wider nanowire width, *i.e.* 500nm-width. In fact, it is not only a missing pixel that contributes to the degree of asymmetry in a TDW, but a number of missing pixels in the edge of nanostructures where they comprise the edge roughness of the structures with non-straight geometries and experimental structures. Thus, nanowires with different edge roughness behaviour are to be discussed below.

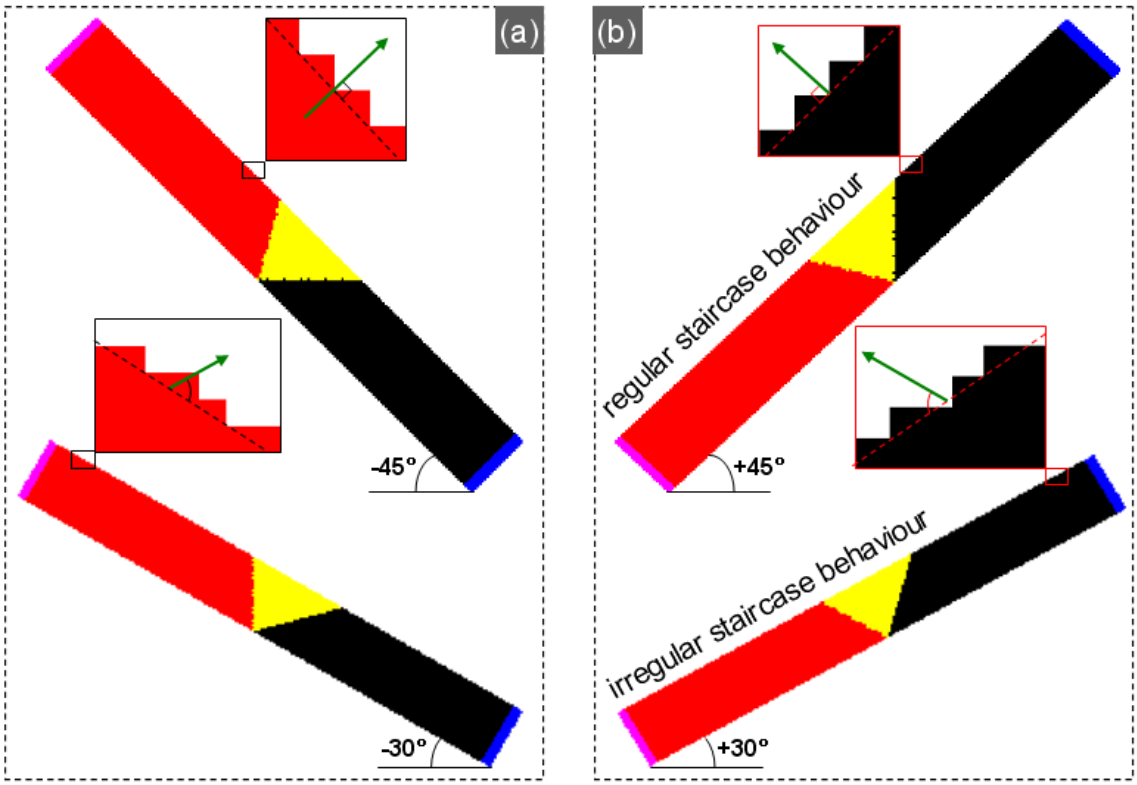

Fig. 3.10 shows 300nm-width-straight nanowire with 10.5nm-thick was rotated in the negative direction/clockwise (a) and positive direction/counter-clockwise (b): From the top downward, the nanowire was rotated at a specific angle of ±45°, ±30°. The insets are shown the edge roughness in the long edges of the rotated nanowires. The arrows are indicated as orientations of the edge roughness which are similar to triangle shapes (triangle anti-notches) grown in different directions at the perfect edge which indicates as dash-lines. The different orientations are induced to variations in local potential energy landscape at the edges.

As a transition point from straight nanostructures (perfect edge behaviour) and straight nanostructures with a missing pixel (controllable edge roughness behaviour) to curved nanowires (uneven edge roughness behaviour), 10.5nm-thick-300nm-width nanowire was first designed as a straight nanowire and then rotated in different angles. This aims to pixelate the long edges of the structure in different edge roughness behaviour, as depicted in Figs. 3.10 (a-b). Here, ± 45°-rotated-nanowires present regular staircase behaviour at their long edges, whereas ±30°-rotated-nanowires have irregular staircase behaviour where pixel arrangements at the long edges act as pinning sites in different orientation levels (see insets). Simulated Fresnel images of those rotated structures and ±10° rotated nanowires are represented in Figs. 3.11(a) and (b), results of normalized degree of asymmetry as a

function of rotation angle are shown in Fig. 3.11(c). The results are contributed into the wall phase diagram for 10.5nm-thick straight nanowires only, as seen in Fig. 3.11(d).

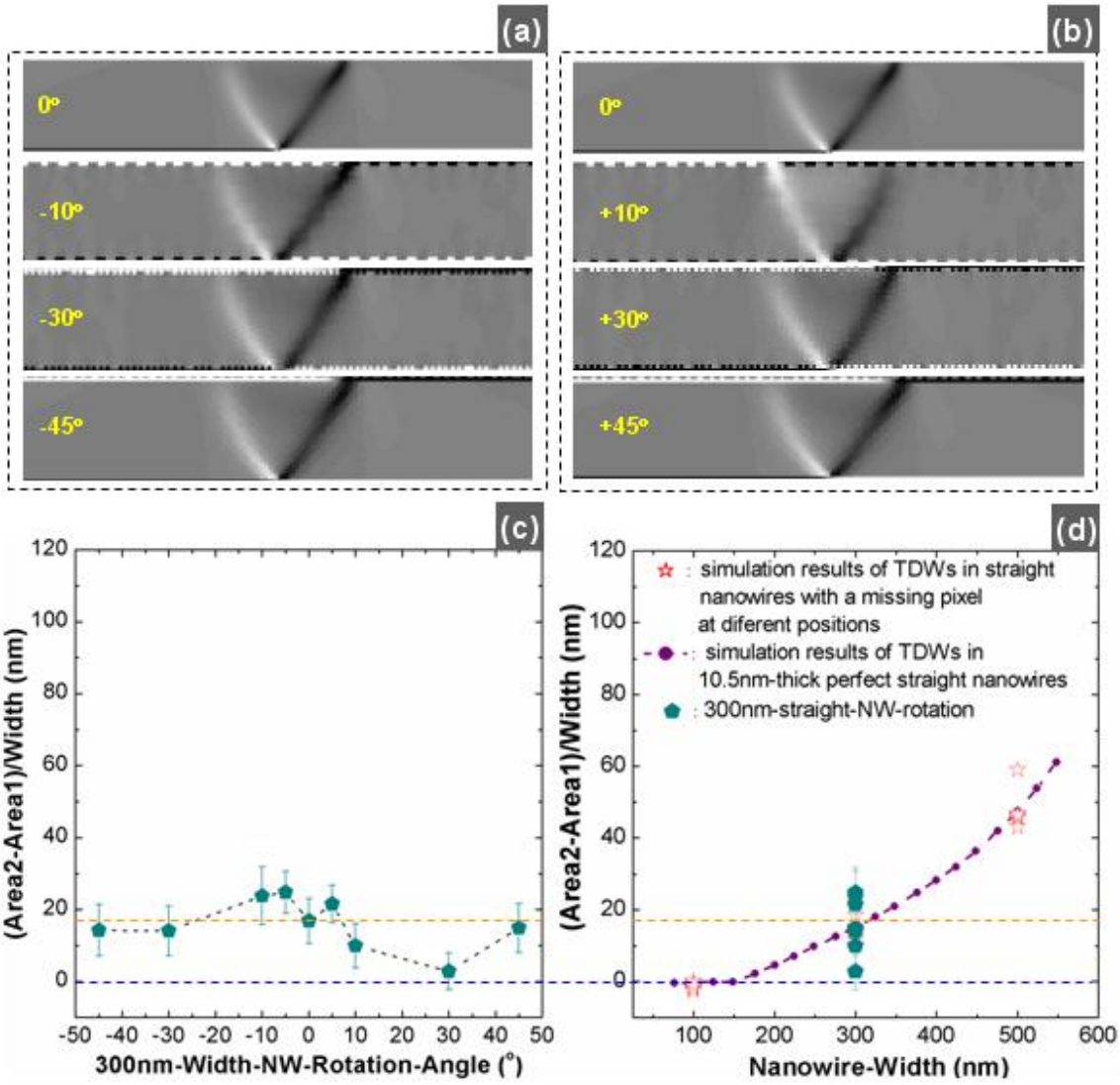

Fig. 3.11 (a) and (b) are Fresnel simulation images of the rotated nanowires in different angles of 0°, ±10°, ±30° and ±45° (from the top downward) and, (c) shows normalized degree of asymmetry in TDWs as a function of rotation angles and (d) presents the wall phase diagram for 10.5nm-thick-nanowire included the results observed in (c). The blue dashed-line indicates the transition point of STDWs↔ATDWs and the yellow-dashed-line which crosses the mean asymmetry values of the perfect nanowire without rotation.

In Fig. 3.11, one can see that the normalized degree values of asymmetry are mostly similar to the structures rotated at ±45° and 0°, indicated by a yellow dash line in Fig.3.11(c). It means that the structures with perfect edges (0°) and rough edges with regular staircase behaviour (±45°) which treats in the similar manner to the TDW. In other

words, the potential energy landscape created by regular staircase behaviour is negligible effects. Close-up, the structures with low-angle-rotations created DWs that tend to be more symmetric in the positive rotations and vice versa. Moreover the asymmetry values are non-equivalent in either side of rotation angles, as shown in Fig. 3.11(c). Taking into account these results with the wall phase diagram for 10.5nm-thick-nanowires with perfect edges, the variations in the degree of asymmetry for the rotated nanowires is wider than that of the straight nanowires with a missing pixel in different positions, as shown in Fig. 3.11(d).

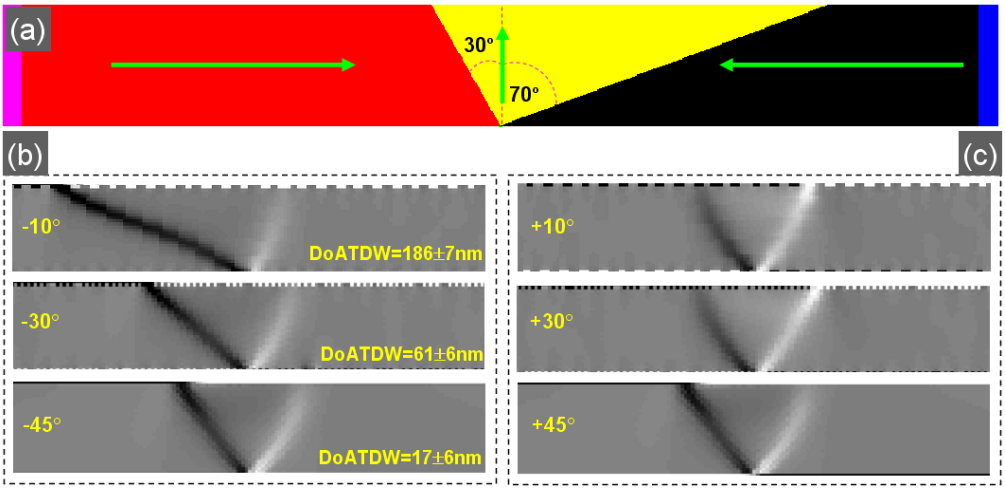

Fig. 3.12 (a) is schematic of 300nm wide nanowire at the starting state of an OOMMF simulation where a triangle with the 100° angle located at the anti-notch is virtually divided into two sub-angles of 30° and 70°. (b) and (c) show simulated Fresnel images of 300nm-width-straight nanowires with 10.5nm-thick which were rotated in different angles, ±10°, ±30° and ±45° (from the top downward). Here, a triangle with 100°-angle located at the anti-notch was created as the starting state for all simulations.

Based on the above results, an issue is raised by the variations in the degree of asymmetry in TDWs for the rotated nanowires in which the degree of asymmetry can be affected by the two wall edge positions at the initial state of the simulation. Hence, instead of creation of a triangle with the 70° angle located at the anti-notch in the initial state of the simulation, another set of rotation structures with the angle of 100° located at the anti-notch were simulated and the 100° vertex can be virtually divided into 30° and 70° angles in either sides of the virtual dividing line, as shown in Fig. 3.12(a). The variation in the degree of asymmetry values in different rotation angles is significantly different, as shown in Figs. 3.12(b) and (c). Here, the asymmetric values are about 186±7 nm, 61±6 nm and 17±6 nm

which correspond to the rotation angles of -10°, -30° and -45°, respectively (see Fig. 3.12(b)). This significant variation at -10º may be affected by enhancement in the degree of pinning at the wall edges due to a variation of magnetization components at the edges. Another reason might come from the starting states of the simulation where one of two wall edges of TDW is pinned more strongly. The reason is, if the two wall edges of the initial TDW are simulated at the states far from the two natural wall edges (for structures rotated at 0º and ±45º) at relaxed state of a TDW, then a competition of the magnetostatic and shape anisotropy is occurred, resulting in the TDW being distorted as presented in the top of Fig. 3.12(b). This only occurs in the simulation where the spin configuration in the anti-notch is artificially pinned, however, this might occur in experiments in the presence of an external field [10, 13].

Obviously, uneven edge roughness behaviour (negative/ positive rotated angles) strongly affects the resulting DW structure and leads to a large variation in the degree of asymmetry in TDWs. Thus, the edge roughness effects were quantitatively explored by means of Fresnel simulations for straight-perfect nanowires, straight-nanowires with a missing pixel and rotated nanowires with uneven edge roughness behaviour. In those cases, the edge roughness can be visualized as regular or irregular staircase behaviour and such behaviour created complicated potential energy landscapes at the perfect edges of the nanowires (indicated by dashed-line in the insets of Fig. 3.10). That way, TDWs created in such nanowires are treated in different ways in relaxation processes depending on the local energy potential landscapes near the two natural wall edges of the TDW. Hence, the simulation results on rotated nanowires are aimed at aiding interpretation of experimental results on curved nanowires, which have an uneven edge roughness parameter. So, by measuring the degree of asymmetry in TDWs experimentally, transformations between STDWs and ATDWs may be determined quantitatively. This is very useful for practical applications in which information on the precise transformation mechanisms within TDW configurations is essential. The remaining parts of this chapter will discuss the experimental results of TDWs which are created in curved nanowires as shown in Fig. 3.2(c).

3.3. TDWS IN CURVED NANOWIRES

In the previous sections, straight and rotated nanowires were discussed where the role of edge roughness was explored. In this section, curved nanowires are introduced where the edge roughness is considered as a combination of regular and irregular parameters resulting from the fabrication process or edge roughness is always existed in experiment. Such structures are mostly familiar to actual structures where the edge roughness is considered as irregular behaviour. Obviously, edge roughness behaviour in curved nanowires is due to the curvature and correlated with rotated straight nanowires (as discussed above). Simulated and experimental results of such structures are reported in the following sections, where both simulation and experimental results of created TDWs in curved nanowires are contributed in the phase diagram.

3.3.1 Simulation results for curved nanowires and their asymmetry calculation

A nanowire was designed as shown in Fig. 3.2(c), a so-called curved nanowire. Here, the ends of the curved nanowire are tapered to gain more control over the switching of this particular section of the element and avoid any DW creations at the ends [17], where tapered geometries were found to provide the lowest switching field, minimize the presence of edge domains and improve stability of the device. By using this architecture, domain walls are generated by applying an external field about an angle with respect to the Oy-direction. This routine is achievable via using the Philips CM20 experimentally as detailed in chapter 2 [10, 13]. When applying an external field, *e.g.* perpendicular to the easy-axis, the curved nanowire generates two different types of domain walls, namely a head-to-head (H2H) and tail-to-tail (T2T) domain wall and an example is shown in Fig. 3.13. Here, Fig. 3.13(a) shows a simulated Fresnel image of 500nm-width-curved nanowire after 0.5 T of external field was applied perpendicular to the easy-axis. Subsequently TDWs were formed in the centre of each curved section. One can see that the H2H TDW is more asymmetric than the T2T one. This might arise from the differences in degree of pinning at the areas where H2H and T2T TDWs are located. Pixellation issues can be visualized at the created TDW locations, one can see from the insets of Fig. 3.13(b), the arrangement of pixels which comprise the curvatures of the curved structure are different, indicated by the numbers

quoting above and below the edges. Such details edge structure differ from structure to structure as nanowire-width is increased.

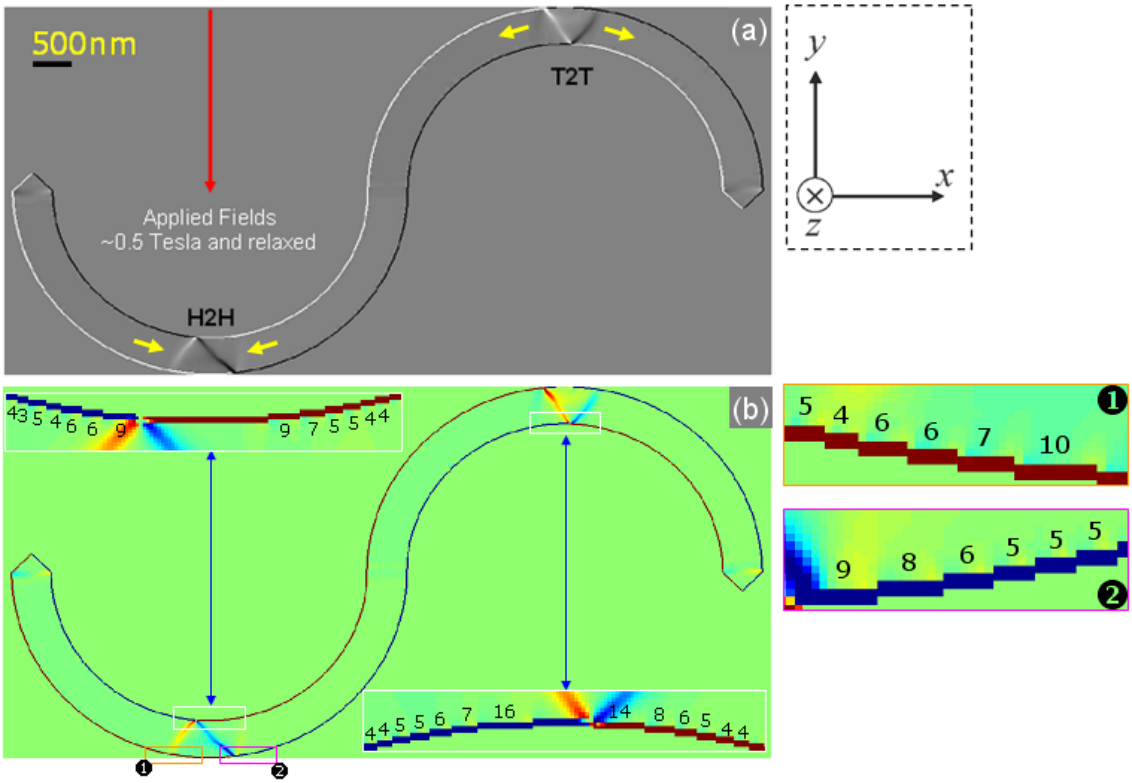

Fig. 3.13 Grey (a) and color (b) Fresnel simulation images of 500nm-width-curved-nanowires of 10.5nm thickness: (a) an external field of 0.5T was applied perpendicular to the easy-axis which aims to generate H2H and T2T TDWs in either curvatures of the structure; (b) uneven edge roughness on either side of the same curved nanowire at the locations of the H2H and T2T TDWs (color images guide your eyes). The insets show particular regimes where irregular staircase behaviour occurred at the edge of the curved nanowire. The numbers of pixels that make up the irregular staircase are quoted above or below the edges.

Now, let's see quantitative results of the effects of edge roughness on the degree of asymmetry of TDWs in 10.5nm-thick-curved nanowires in differing nanowire-widths. Before going further in details, the TDW calculation method in the curved nanowires is now reintroduced where a minor change in the calculation procedures is described. As the first step, instead of using a perpendicular line as the dividing line that crosses the intersection of TDW and perpendicular to the other edge of straight-nanowire, here inner and outer circles fitting into the inner and outer circles of the curvatures of the Fresnel images of the curved nanowires are defined. Secondly, when the inner and outer circles are defined, the dividing

line can be determined by crossing a straight line through the circles centre and the intersection point of the TDW. Finally, two halves of the TDW (A_1 and A_2) are subsequently observed as areas within the dividing line, inner, outer-arcs and either wall edge sides of TDW, as depicted in Fig. 3.14. This calculation is performed using the Digital Micrograph™ software.

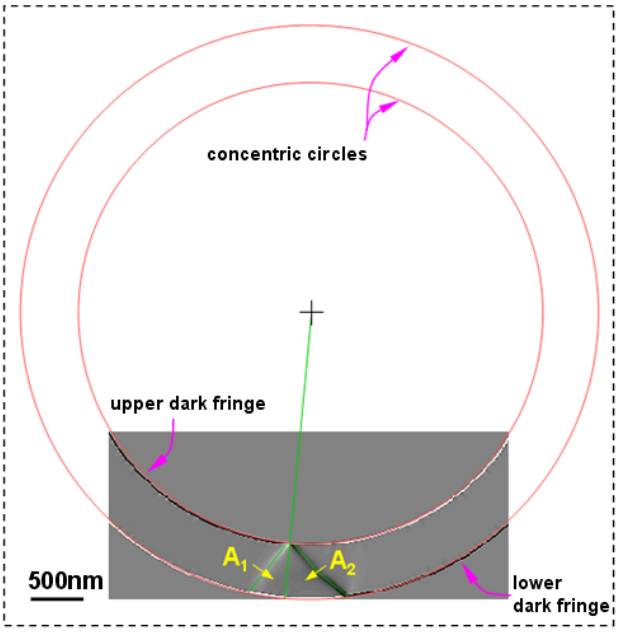

Fig. 3.14 A demonstration of measuring degree of asymmetry in TDW using Digital Micrograph™ software, *i.e.*, a simulated H2H-TDW Fresnel image in 500nm-width curved-nanowire.

Fig. 3.15 shows a series of Fresnel images of H2H and T2T TDW simulated in the 10.5nm-thick-curved nanowires of different widths. By applying an external field perpendicular to the easy-axis of the structure, the structure was then relaxed, H2H and T2T transverse domain walls were created in the lower and upper curvatures of the curved nanowire, respectively. The magnetization configurations on either side of the H2H- and T2T-TDWs could be recognized from dark fringes in the Fresnel images as described in chapter 2. Hence, this chapter is purely focused on measuring the areas inside TDWs. The Fresnel images presented in Fig. 3.15 contain purely magnetic contrast calculated from the in-plane magnetization components and effects of de-focus are negligible. However, the edge fringes in experimental Fresnel images are a combination of both magnetic and

electrostatic effects, subsequently domain walls created in the narrow nanowires, *i.e.*, 200nm-nanowire-width, might not be seen clearly.

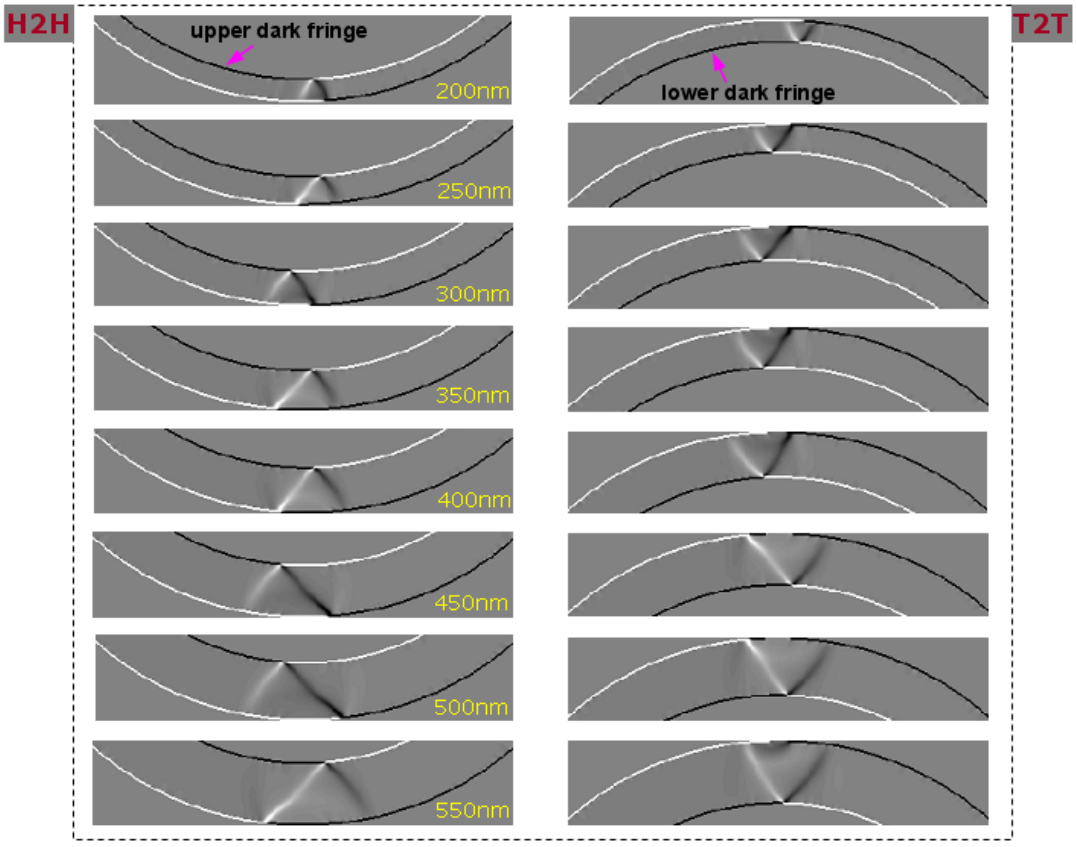

Fig. 3.15 A set of created H2H and T2T TDWs in 10.5nm-thick curved nanowires with widths varying from 200 nm to 550 nm in 50 nm step.

Using the calculation method above (see Fig. 3.14) for all H2H and T2T TDWs (see Fig.3.15), the normalized degree of asymmetry values of H2H and T2T TDWs were calculated and plotted in Figs. 3.16(a) and (b), respectively. This plot aims to compare the previous results with results observed from the 10.5nm-thick curved nanowire of different widths. One can see that the degree of asymmetry values of H2H-TDWs in curved nanowires are comparable to the asymmetry values of TDWs in straight nanowires (Fig. 3.16(a)), while the results of T2T TDWs are far off the asymmetry line of the straight nanowires for widths of 500nm and 550nm (Fig.3.16(b)). Obviously, edge roughness affects the degree of asymmetry of TDWs as it treats in different manners for different types of TDWs at different locations where responsibility of localized spins depends on grain sizes/orientations at the perfect edge (shown as dashed lines in the insets of Fig. 3.10) and

this is clearly visualized in the insets of Fig. 3.13(b). Subsequently, reduction of the T2T TDW asymmetry values at the wider-nanowire-width regime (from 350nm to 550nm) can be understood as irregular edge behaviour (see ❶- and ❷-locations in Fig. 3.13(b)) affecting one TDW type. The TDW configurations can be seen in Fig. 3.15.

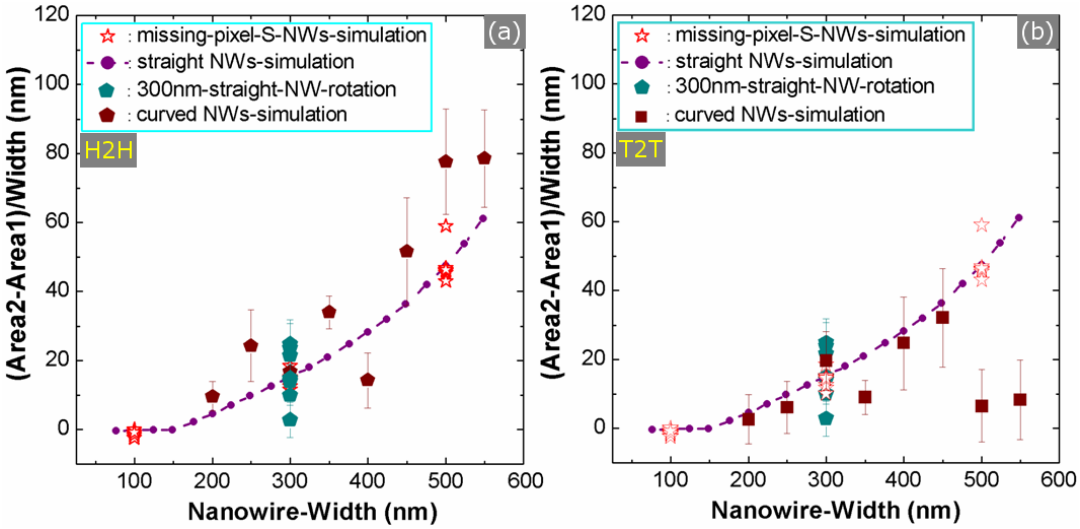

Fig. 3.16 shows degree of asymmetry values of H2H and T2T TDWs in 10.5nm-thick-curved nanowire as a function of nanowire-widths, respectively. The results are added into the wall phase diagram which was presented in Fig. 3.11(d) where they are presented as dark-red-pentagonal and square symbols.

3.3.2 Fabrication of curved nanowires and experimental results

As mentioned above, the edge roughness behaviour of the real structures is an uneven parameter. However, to quantify the role of edge roughness affecting TDWs in experimental structures via the degree of asymmetry measurement, curved nanowires were fabricated/ patterned using the FIB method, in which 50% pixel overlap (expected to be observed smoother edge specimen profiles), 10 nm-FWHM Ga^+ ion probe (energy of 30 keV and current of ~10 pA) were used. The magnetic characterizations were then undertaken using Fresnel imaging mode in the Glasgow FEG CM20. BF images at the curvatures of the curved nanowires are shown in Fig. 3.17 where the images at the left and right panels correspond to H2H and T2T TDW locations. One can see that even aiming to fabricate structures in different widths of 200-550nm with 50nm-step width, patterned structures are slightly wider than that of the designed structures. Moreover, edge roughness is not only different from structure to structure, but also varied in the same structure at different

locations and growth grain sizes. Some darker grain growth covered by recrystallization appearing near the edges of the nanowires are due to the irradiation processes and this may be affected to magnetic properties of the nanowires and also was described elsewhere [21-25].

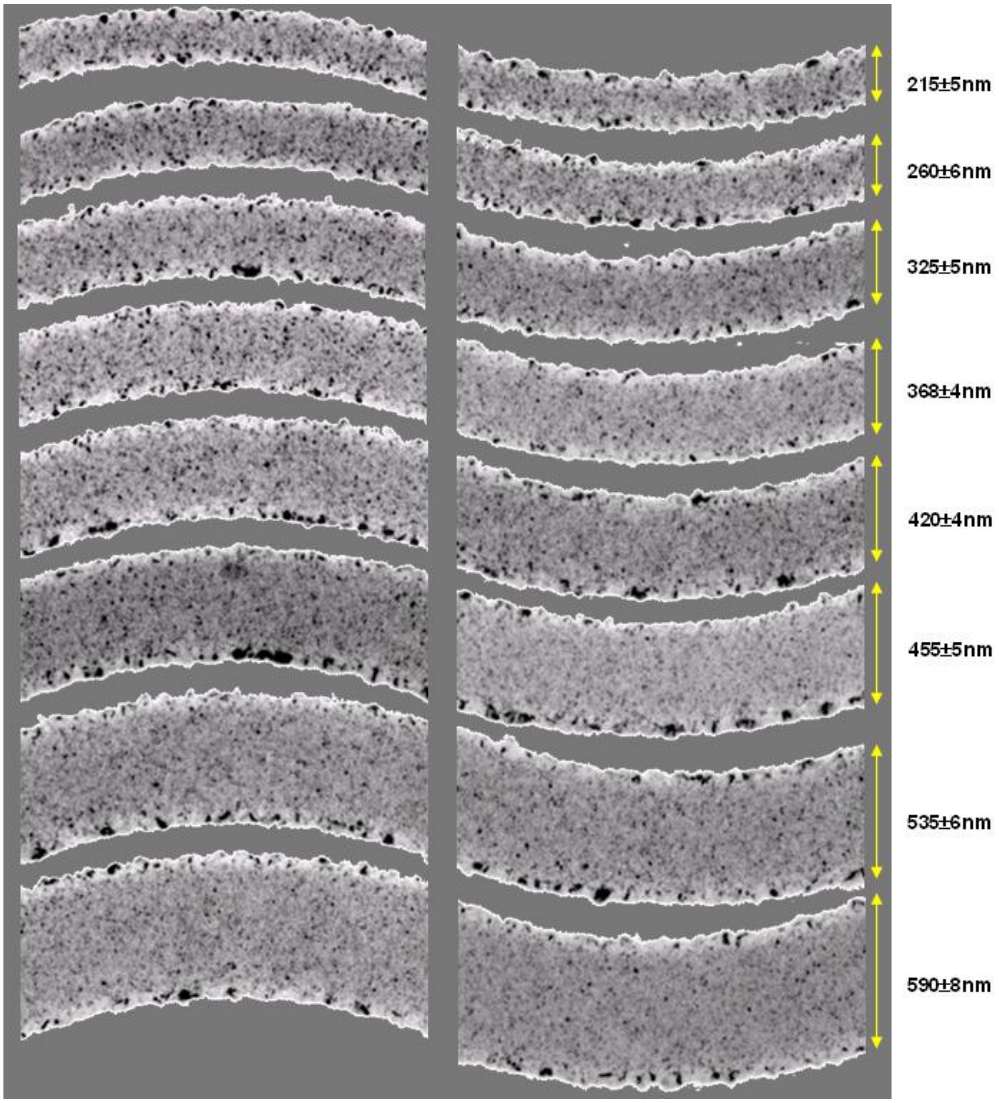

Fig. 3.17 shows BF images of the curvatures of the patterned curved-nanowires of different widths. The images in the left and right panels correspond to the locations where H2H and T2T TDWs will be created by applying an external field perpendicular to the easy-axis.

Assuming that the structures have no edge roughness, asymmetry values of TDWs are therefore equal in differing locations at the same structure. In fact, because of edge roughness, the degree of asymmetry of TDWs is different at different locations in the same structure. Hence, if a TDW is created in the structure at a specific location, the degree of

asymmetry might be changed when the TDW is created at other locations in the same structure. In order to understand this, external fields were alternatively applied in different directions with respect to the direction perpendicular to the easy axis of the structure, as depicted in Fig.3.18. This aims to create DWs at various positions in the structure and the degree of asymmetry values was then calculated for the created TDWs at particular positions. From that the role of edge roughness may be exposed.

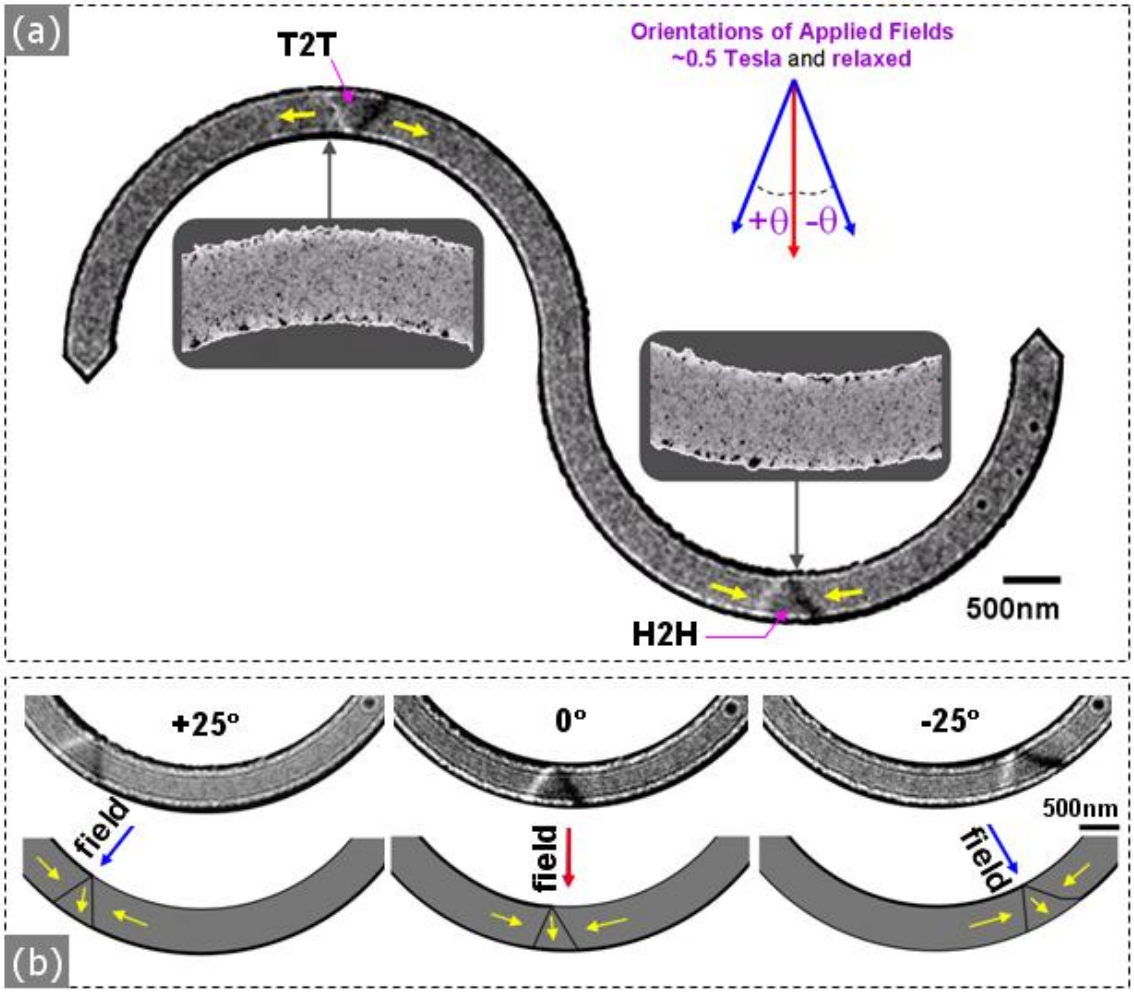

Fig. 3.18 (a) is a Fresnel image of remanent state of 10.5nm-thick-patterned-500nm-width-curved nanowire where H2H (right) and T2T (left) TDWs were created by applying a perpendicular external field of 0.5T. In the insets, BF images are shown correspondently at the created H2H and T2T TDW locations. The inset in the top right is a schematic of external field directions correspond to the easy-axis of the nanowire. (b) Fresnel images of relaxed H2H TDWs were created in different external field directions and their schematics are shown underneath.

As an example, a defocused (Δ≈3600μm) Fresnel image of patterned 10.5nm-thick-500nm-width curved-nanowire is shown in Fig. 3.18(a) where TDWs were created by applying an external field perpendicular to the easy-axis. BF images of selected areas of the appropriate curvatures in the curved nanowire are also represented as the insets. Moreover, a schematic of external field orientations is attached in the top-right of Fig. 3.18(a). One can see that H2H and T2T TDWs are simultaneously created in the same structure and the TDWs are roughly symmetric. In the cases of using different external field directions, +25°, 0° and -25°-orientated fields were alternatively applied with respect to the direction perpendicular to the easy-axis of the curved nanowire, subsequently Fresnel images were observed in which H2H-TDWs were created at specific locations as shown in Fig. 3.18(b). It can be seen in Fig. 3.18(b), TDWs that were observed in the +25° and 0°-oriented fields are roughly similar, while under the -25°-field orientation, TDW is more asymmetric. This might suggest that after the TDW is created by the oriented field it could be pinned by uneven pinning sites at the long edges of the curved nanowire. Thus, using different oriented fields, the effect of the edge roughness can be probed. Therefore, asymmetry values for all TDWs created in different field orientations (± 25°, ± 15° and 0°) were calculated from Fresnel images.

For instance, as shown in Fig. 3.19, Fresnel images of H2H and T2T TDWs were created in the 10.5nm-thick-curved nanowires under 0° oriented field direction, those results are to be discussed in the next sub-section. Note in particular that DWs created in narrow-width-curved nanowires, *i.e.* 215nm and 260nm-width are difficult to analyze on their Fresnel images due to the reduced widths. The difficulty is due to the level of magnetic contrast being reduced due to electrostatic effects becoming dominant edge effects, i.e, the top images of Fig. 3.19. Thus, some points for the curved structures with the narrow widths will not present in the wall phase diagram.

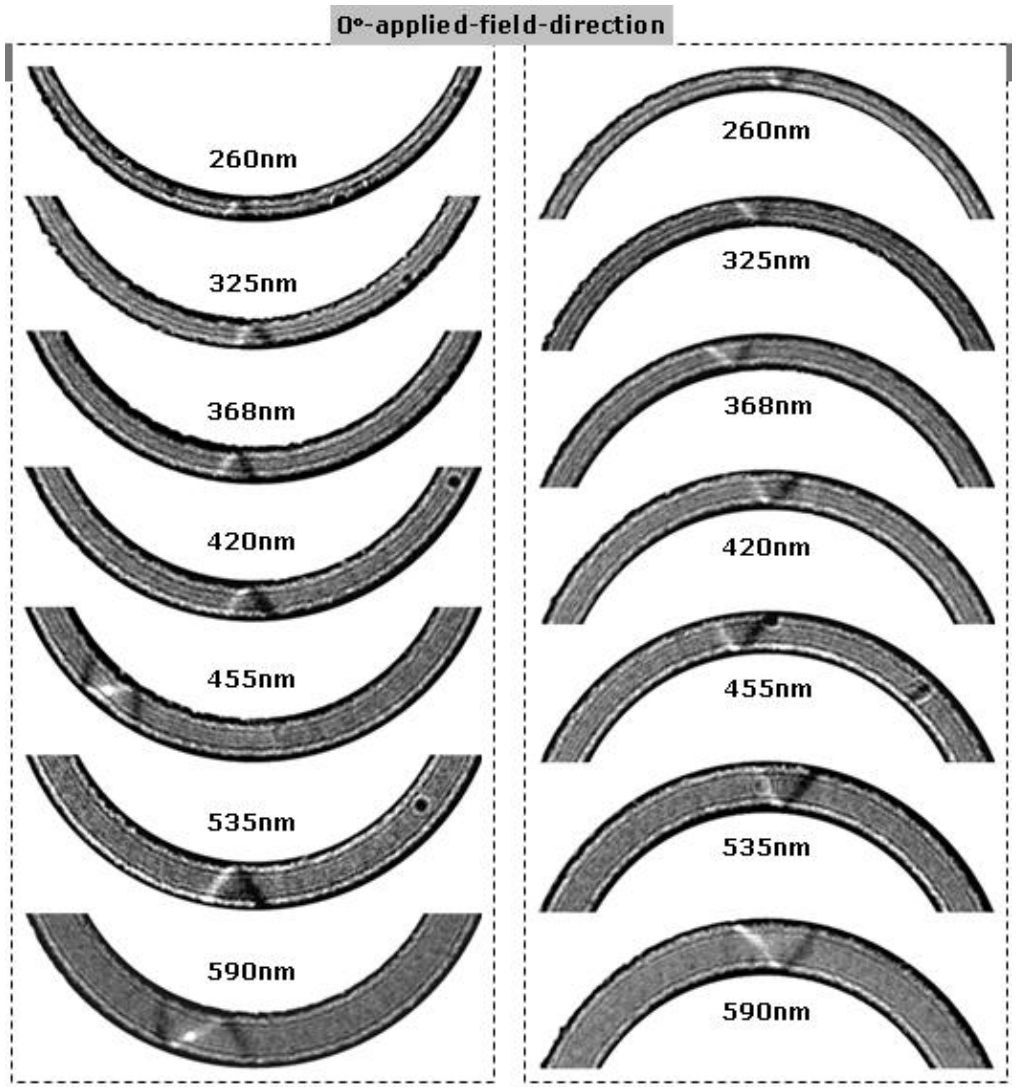

Fig. 3.19 is Fresnel images of relaxed DWs which were created by the 0°-field-orientation in patterned 10.5nm-thick-curved-nanowires with different widths. H2H and T2T DWs are shown in the left and right-panels, respectively.

3.3.3 Degree of Asymmetry in TDWs created in 10.5nm-thick curved-nanowires

Fresnel images of H2H (left) and T2T (right) DWs in the 10.5nm-thick-curved-nanowires for different nanowire-widths are shown Fig. 3.19, where DWs were created by the 0°-oriented-field-direction. It can be seen that most of DWs are TDWs, except two H2H VDWs were created in the 455nm and 590nm-width-nanowires. Those two VDWs are fallen to the VDW regime in the phase diagram reported in ref. [7]. Again, as mentioned earlier in sub-section 3.2.2, above the transition points of ATDWs↔VDWs, the VDW can possibly be observed. Creation of VDWs might be due to edge roughness that affects

directly to DW transformations during the DW creation process [18] or stability of a DW as a function of time in which the edge roughness of the structure is build up a potential energy landscape that affects each DW creation/relaxation process. Moreover, under the 0°-oriented-field-direction, the created VDWs is shifted away from the central positions, which could be due to different degrees of pinning along the structure edge with a number of stable and metastable states. Alternatively ±15° and ±25° oriented-fields were applied to create DWs at specific points in the curvatures of the curved-nanowires. H2H DWs that were created by the positive field directions are more reproducible than that of H2H DWs created by the negative fields. Moreover, some of the created DWs transformed from TDWs to VDWs in the creation and/or imaging processes, while the T2T DWs are mostly stable and did not transfer from TDWs to VDWs. This implies that the field directions also affect DW formations in the structures with irregular roughness behaviour on either side of the nanowires (structural asymmetry).

The results of normalized degree of asymmetry of H2H and T2T-TDWs created by different orientated-fields in the curved nanowires as a function of the nanowire-widths are plotted in Figs. 3.20(a) and (b), respectively. The number of points plotted in Fig. 3.20(a) is less than that plotted in Fig. 3.20(b), due to VDWs being created in some nanowires and those TDWs in very narrow nanowires, *i.e.* 215 nm and 260 nm-widths being unmeasurable. Here, all asymmetry values were calculated by using the same method which was introduced in Fig. 3.14. Clearly, the experimental results are scattered more widely than the simulation results of the perfectly nanowires. None of the points corresponding to the H2H TDWs are exactly lined on the transition points (asymmetry values are equal to zero, STDW), while at least one point in the T2T-TDW graph is lied on the transition line, indicated by green dashed lines in Fig. 3.20. However all of the experimental points for H2H and T2T TDWs show a similar trend, an increase in degree of asymmetry with increasing nanowire width. As one can see in the wall phase diagram of the H2H TDWs in the straight nanowires without a missing pixel and rotation, if the nanowire-widths are wider than 150nm, it is impossible to create STDWs theoretically, however it can be observed in curved nanowires, as shown in Fig. 3.20(b) where at least one point lies on the transition line and the possibility of finding STDWs in the structures with narrower

nanowire-widths is higher than that of simulated straight nanowires, indicated by error bars. Here, the error bars came from 5 measurements for each TDW at a certain field direction. Moreover, in the certain field direction, 5 TDWs were created and calculated, thus the error bars indicate the level of TDW stability and reproducibility of a TDW at a specific area in the nanowire.

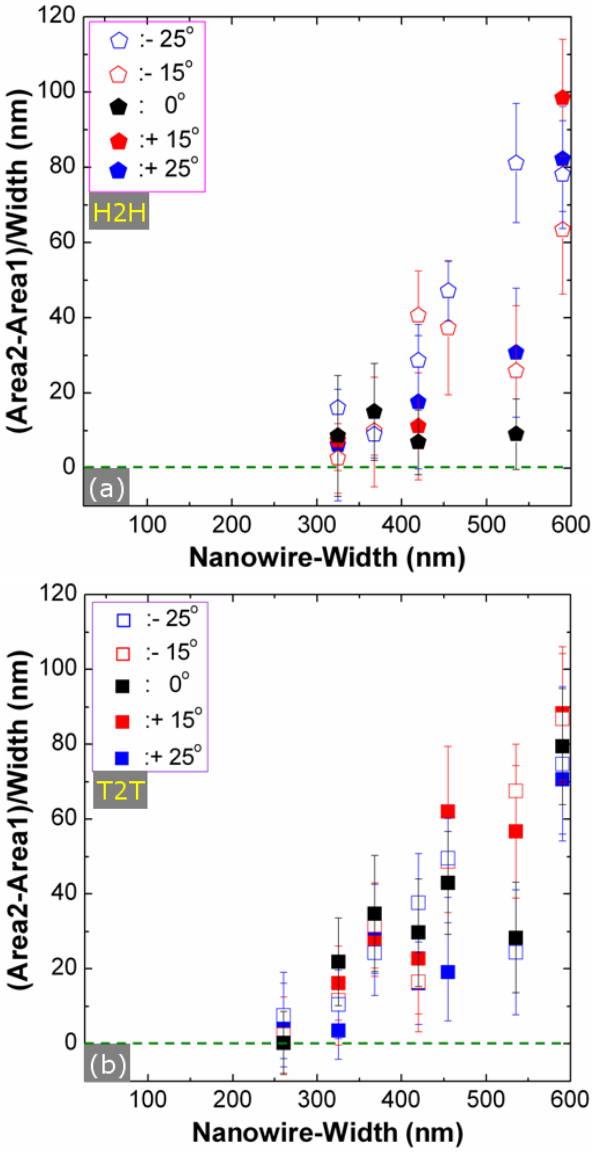

Fig. 3.20 Degree of asymmetry values for TDWs in curved nanowires as a function of nanowire widths where the TDWs were created experimentally in different field directions: (a) and (b) are presented results for H2H and T2T TDWs, respectively. The results are presented by this way that aims to compare the experimental results with the simulation results that were presented in Fig. 3.16. Green dashed lines indicate the transition points between STDWs ↔ATDWs.

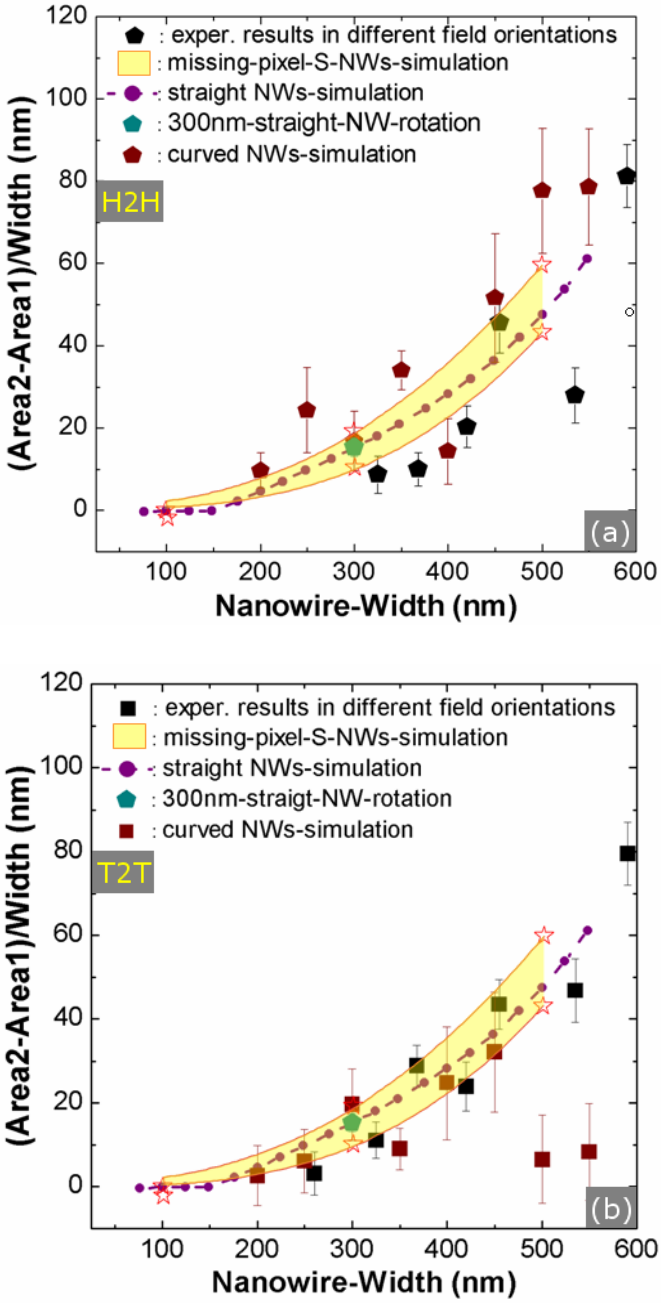

Fig. 3.21 Experimental results of averaged TDW asymmetry values for the curved nanowires (presented in Fig. 3.20) are plotted against the nanowire widths in combination with the simulation results of straight perfect nanowires (violet solid-circle-dashed line, this was also presented in the previous figures, Fig. 3.9(d), Fig.3.11(d) and Fig. 3.16). Results deriving from straight nanowires with a missing pixel are plotted as the yellow bound (which is defined by the two fitting lines from maxima and minima of the asymmetry values for 100 nm, 300 nm and 500 nm-width nanowires). Simulation results for rotated nanowires (dark cyan pentagon) and curved nanowires (wine solid symbols).

The simulated and experimental results for straight, rotated and curved nanowires can be combined in a graph for each type of TDWs. The wall phase diagrams of H2H and T2T TDWs can be summarized, as shown in Fig. 3.21. Here, the experimental results of asymmetry values in different oriented-fields are averaged and represented as black-solid-pentagons and squares in Figs. 3.21(a) and (b), respectively. One can see clearly the trends of TDW asymmetry values in curved nanowires in both experiment and simulation in correlation to the trend of H2H-TDW asymmetry values of perfect nanowires. The simulated and experimental results of the H2H TDWs in the curved nanowires are distributed closely around the results of simulated straight-perfect nanowires and the bound of asymmetry values of the TDWs in straight nanowires (100 nm, 300 nm and 500nm-widths) with a missing pixel, indicated by the yellow band in Fig. 3.21(a), whilst the results of T2T-TDWs loosely follow the trend of the results of simulated straight perfect nanowires and the bound of asymmetry values in the structures with a missing pixel (see Fig. 3.21(b)).

The above results can be suggested that the trend of simulated and experimental results of H2H TDWs in the curved nanowires is comparable to the simulation results of H2H TDWs in the straight nanowires. However, the trend in the T2T TDWs is slightly different. The reason for that might be caused by combination effects of edge roughness, thermal excitation and the out-of-plane field component (see section 2.4.1 and Fig. 2.12) in which they are affected to the experimental results. Also, spin configurations of H2H TDWs are not equivalent to the T2T TDWs in curved nanowires and/or DW configurations are influenced by the field orientations with respect with pinning potential energy landscapes constituted by irregular edge roughness behaviour along the long edges of the curved nanowires (structural asymmetry for H2H and T2T locations).

Thus, the degree of asymmetry values of transverse domain walls were experimentally calculated from de-focused Lorentz images where the domain wall width profiles are larger than that of in-focused images [12]. Even so it does not change the observed results because the calculated values are compensated when the areas inside the TDW were reduced/ increased simultaneously at a specific condition of the measurement, *i.e.*, de-focused distance. Here, the experimental results were calculated for all Fresnel images with the same conditions. To make sure the calculated results from de-focused and in-focused (DPC)

images are consistent, a series of DPC images from the given structures were undertaken in the similar routines: oriented fields were applied in different angles with respect to the direction perpendicular to the easy axis to create DWs. An example is shown in Fig. 3.22 where H2H-TDWs were created in the 420 nm-width curved nanowire by the 0°, ±10° and ±20°-oriented-field-directions and then imaged by the DPC imaging technique.

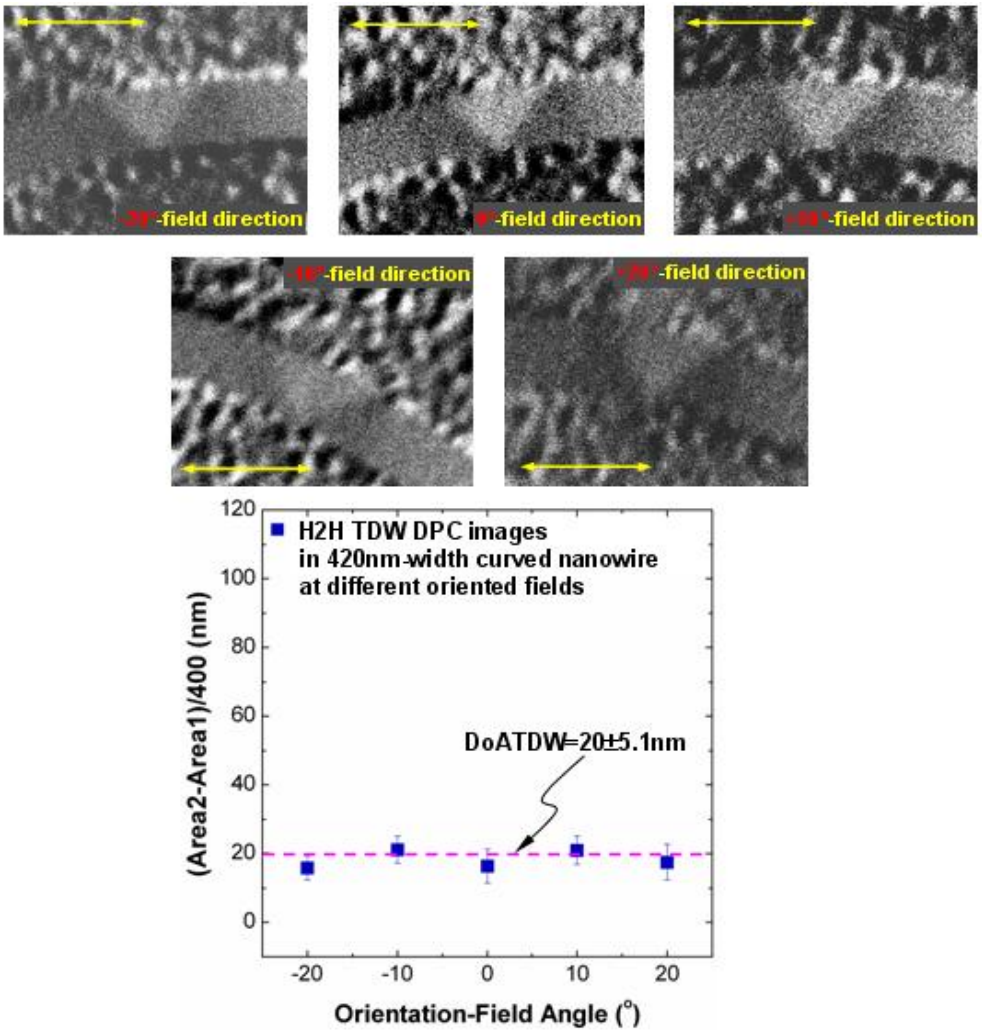

Fig. 3.22 DPC images of H2H TDWs in 10.5nm-thick-curved nanowire with 400nm-nanowire-width, the TDWs were created in different oriented-field directions, 0°, ±10° and ±20°. Results of degree of asymmetry in TDWs as a function of orientation field angles are shown in the graph. The arrows are indicated the sensitive directions of DPC signal.

Asymmetry values of those TDWs as a function of field orientation angles are presented in the graph of Fig. 3.22. One can see that the averaged value of degree of asymmetry of TDWs in different oriented direction angles, calculated from the DPC images,

is 18.4 ± 3.5 nm, while the averaged value measured from de-focused images which was presented in Fig. 3.21 is 20 ± 5.1 nm. So, they are fairly coincided and the small difference might belong to the stability of the domain wall configuration as a function of time. A TDW was observed to oscillate after nucleation in the absence of an external field. Depending on when the oscillation sequence the image was captured, the measured degree of asymmetry may differ. A short movie was recorded before DPC performances (not shown in the text). That means, even an external field was off after a domain wall creation, domain wall state was still affected by the residential field and/or DW oscillation is occurred in a wide potential well build up by the edge roughness of the structure [14].

3.4. SHORT SUMMARY OF THE CHAPTER

Throughout the chapter, quantitative information on the degree of asymmetry of TDWs was obtained experimentally and compared with simulation. A correlation between ratios of magnetization components (M_x and M_y) and areas inside transverse domain walls in straight ferromagnetic nanowires was investigated by means of micromagnetic simulation and MatLab calculations. Here, the in-plane magnetization components are related directly to the Fresnel image contrast. Thus, the investigated results are useful where the ratios of magnetization components and areas inside TDW were plotted as phase diagrams of STDW-ATDW transformation. From this observation, the boundary of STDW-ATDW is found and range of ATDW stability was quantified. Furthermore, using such calculation methods, effects of edge roughness from the straight to curved nanowires were indirectly characterized via the degree of asymmetry calculations in both simulation and experimental works. Our results are a new route-map of quantitative measurement for transition between symmetric and asymmetric TDWs. The results are helpful for the determination in TDW configurations at the static state after the application of a magnetic field or electrical current pulse when TDWs are driven by field or current. The variation in the trends of degree of asymmetry curves as a function of nanowire-widths are due to the edge roughness along the nanowires which acts as pinning sites at the curvatures of the curved-nanowires or asymmetries in the local potential well that are correlated with the pinning geometry [19]. Moreover, if the roles of the edge roughness are quantitatively determined, then effects on

domain wall de-pinning field/ current strength can be dynamically understood. Here, the de-pinning field/current is defined as the field/current supporting for a DW to overcome the pinning barrier of pinning sites when domain walls propagate in the nanowires under field/current [5, 14, 16]. Experimentally, vortex domain walls were sometimes nucleated in the curved nanowires at medium widths of 420-535nm. This might come from the potential energy landscape of the nanowire, particularly localized at DW locations. This also might come from thermal effects that affect the magnetizations in real structures where the experiments were performed at room temperature, while thermal effects were not included in the simulation results. Another factor might affect into the DW state is small residual field which was present after domain wall creation processes. Thus, in cases of the small resident field remained and thermal effects are included, STDW ↔ ATDW ↔ VDW transformations might be occurred with respect to the excitation and oscilatory relaxation of the domain wall reaches to its equilibrium position [18]. Based on the observed results, it can be concluded that H2H and T2T TDWs are formed in different manners in the curved nanowires where the edge roughness effects are assumed as uneven behaviour along the edge of the nanowires where the edge roughness was build up the potential energy landscape associated with localized stable and metastable states. Even the effects of edge roughness are mainly affected to the degree of asymmetry in TDWs, other effects belong to the FIB fabrication process might be concerned because of a number of FIB parameters can be induced to the material properties at near the edges of the specimens [20-25]. This also can be seen in Fig. 3.17 where the small darker layer grains were appeared near the edges of the FIB structures in the BF images.

REFERENCES

[1]. S. S. P. Parkin, M. Hayashi and L. Thomas, *Science* **320** (2008) 190

[2]. D.A. Allwood, G. Xiong, M.D. Cooke, C.C. Faulkner, D. Atkinson, N. Vernier, R.P. Cowburn, *Science* **296** (2002) 2003

[3]. D.A. Allwood, G. Xiong, C.C. Faulkner, D. Atkinson, D. Petit, R.P. Cowburn, *Science* **309** (2005) 1688

[4]. G. Hrkac, J. Dean and D.A. Allwood, *Phil. Trans. R. Soc. A* **369** (2011) 3214

[5]. A. Thiaville, Y. Nakatani, *Domain wall dynamics in nanowires and nanostrips* in *Spin Dynamics in Confined Magnetic Structures III*: *Topics in Applied Physics* **101** (2006) 161-205.

[6]. M. Kläui, *J. Phys.: Condens. Matter* **20** (2008) 313001R

[7]. Y. Nakatani, A. Thiaville, J. Miltat, *J. Magn. Magn. Mater.* **290-291** (2005) 750

[8]. R.D. McMichael, M.J. Donahue, *IEEE Trans. Magn.*, **33** (1997) 4167

[9]. I. Neudecker, M. Kläui, K. Perzlmaier, D. Backes, L. J. Heyderman, C. A. F. Vaz, J. A. C. Bland, U. Rüdiger, C. H. Back, *Phys. Rev. Lett.* **96** (2006) 057207

[10]. D. Petit, H.T. Zeng, J. Sampaio, E. Lewis, L. O'Brien, A.-V. Jausovec, D. Read, R.P. Cowburn, K. J. O'Shea, S. McVitie and J. N. Chapman, *Appl. Phys. Lett.* **97** (2010) 233102

[11]. D. Petit, A.-V. Jausovec, D. Read, R.P. Cowburn, *J. Appl. Phys.* **103** (2008) 114307

[12]. S. McVitie, M. Cushley, *Ultramicroscopy* **106** (2006) 423

[13]. C. W. Sandweg, N. Wiese, D. McGrouther, S. J. Hermsdoerfer, H. Schultheiss, B. Leven, S. McVitie, B. Hillebrands, J. N. Chapman, *J. Appl. Phys.* **103** (2008) 093906

[14]. Y. Nakatani, A. Thiaville, J. Miltat, *Nat. Mater.* **2** (2003) 521

[15]. J. Kim, M.-H. Jung, S.-B. Choe, *IEEE Trans. Magn.*, **45** (2009) 2481

[16]. M.T. Bryan, D. Atkinson, R.P. Cowburn, *Appl. Phys. Lett.* **85** (2004) 3510

[17]. J. Gadbois and J.-G. Zhu, *IEEE Trans. Magn.*, **31** (1995) 3802 and **34** (1998) 1066

[18]. S. Bance, T. Schreft, G. Hrkac, D. Suess, C. Brownlie. S. McVitie, J. N. Chapman, D. Allwood, *IEEE Trans. Magn.*, **42** (2006) 2966

[19]. A. Bisig, J. Rhensius, M. Kammerer, M. Curcic, H. Stoll, G. Schütz, B. van Waeyenberge, K.W. Chou, T. Tyliszczak, L. J. Heyderman, S. Krzyk, A. von Bieren, and M. Kläui, *Appl. Phys. Lett.* **96** (2010) 152506

[20]. C. L. Dennis, R. P. Borges, L. D. Buda, U. Ebels, J. F. Gregg, M. Hehn, E. Jouguelet, K. Ounadjela, I. Petej, I. L. Prejbeanu, M. J. Thornton, *J. Phys.: Condens. Matter* **14** (2002) R1175.

[21]. J. Fassbender and J. McCord, *J. Magn. Magn. Mater.*, **320** (2008) R579

[22]. D. McGrouther, W.A.P. Nicholson, J.N. Chapman, S. McVitie, *J. Phys. D: Appl. Phys.* **38** (2005) 3348

[23]. A. F.-Pacheco, J.M. de Teresa, A. Szkudlarek, R. Córdoba, M.R. Ibarra, D. Petit, L. O'Brien, H.T. Zeng, E.R. Lewis, D.E. Read and R.P. Cowburn, *Nanotechnology* **20** (2009) 475704

[24]. H.H. Long, E.T. Ong, T. Liu, H.L. Li, Z.J. Liu, E.P. Li, H.Y. Wu and A.O. Adeyeye, *J. Magn. Magn. Mater.*, **303** (2006) e299

[25]. W. F. Van Dorp and C.W. Hagen, *J. Appl. Phys.* **104** (2008) 081301R

Chapter 4

Conclusions and Future Work

4.1 OUTLOOK

A deeper understanding of DW creation and propagation in Py nanowires is crucial for the development of future spintronics devices [1-7]. An important characteristic of such devices is regarding the possible DW configurations. In general, three types of DW configurations such as VDW, STDW and ATDW usually exist in nanowires of different nanowire-thickness and widths, which was simulated and shown in a DW phase diagram reported by Nakatani *et. al*. [8], see Fig. 3.1(a). Much effort has been spent on DW observation techniques in order to observe DW behaviour directly under the application of a magnetic field or electrical current. However, DW transformations in real nanostructures have been paid less attention. Hence, the structure and behaviour of TDWs was extensively studied in this work by means of micromagnetic simulation [9] and Lorentz microscopy [10]. In particular, the focus being on the transformation of STDWs↔ATDWs which was quantitatively characterized from structure to structure, from perfect straight nanowires to imperfect straight and imperfect curved nanowires. Firstly, this aims to explore a correlation between the magnetization components (M_x, M_y) and region areas (A_1, A_2) inside a TDW in which a TDW is simply divided into two region areas by a virtual dividing line crossing the intersection of the TDW and perpendicular to the long edge of the straight structure. Secondly, if the above target is achieved, the correlation can be used to characterize the degree of asymmetry in TDWs experimentally. In fact, experimental nanostructures consist of different degrees of edge roughness or designed constrictions, an understanding of TDW transformation is a useful way to understand the role of defect in real structures indirectly where edge roughness plays a crucial role [11]. Based on the results that were observed and presented in this thesis, future plans are finally given, in which a promising project is described for continuation after this work.

4.2 CONCLUSIONS

In chapter 3, the degree of asymmetry of TDWs was characterized quantitatively in

both simulation and experiment. Interestingly, we obtained a correlation between ratios of magnetization components (M_x and M_y) and region areas (A_1, A_2) inside TDWs in perfect straight Py nanowires by means of OOMMF simulation and MatLab calculations. This is a key result of chapter 3 and also for the thesis, in which the transformation of STDWs↔ATDWs in perfect straight nanowires in different widths is a smooth curve for a particular thickness (see Fig. 3.6). As a notice, if the degree of asymmetry is equal to zero, a STDW is observed otherwise we have an ATDW. This correlation was then used to calculate degrees of asymmetry of created TDWs in imperfect nanowires such as straight nanowires with a missing pixel in different locations at the long edge opposite to the intersection of the TDW, straight nanowires with regular staircase behaviour at the long edges (*i.e.* ±45°-rotated straight nanowires) and uneven staircase behaviour at the long edges (*i.e.* ±30°-rotated straight nanowires and curved nanowires). From the given nanostructures, the role of edge roughness was explored by using degree of asymmetry calculations. For the straight nanowires with a missing pixel, the transformation of STDWs↔ATDWs was largely varied when the missing pixel located near the natural wall edges (see Fig. 3.9(b)) and was not significantly changed if the missing pixel located far from the natural wall edges (see Figs. 3.9(c) and (d)). Moreover, it has no significant differences in the degree of asymmetry if the TDW is created in either the perfect straight nanowire or the straight nanowire roated at ±45° (the edge roughness is regular staircase behaviour). In contrast, a DW configuration was formed with unpredictable behaviour in lower rotated-angles-straight nanowires, *i.e.* ±10°, ±30°, with the same width and thickness. Here, the DW configuration depends on the staircase behaviour with the uneven edge roughness behaviour acting as unpredictable energy landscapes at the perfect edge, leading to DW distortion at two natural wall edges in the relaxed state. Similarly, TDWs were formed with unpredictable configurations in curved nanowires with uneven edge roughness behaviour (see Fig. 3.13). All created TDWs in the above nanowires with regular and uneven staircase behaviour were calculated and plotted in the same graph for comparison (see Fig. 3.21). The results showed that the asymmetry values of the created TDWs were distributed around the smooth curve of the simulation for the created TDWs in the perfect straight nanowires. From the above results, it can be understood that the edge roughness

behaviour strongly affects the DW transformation during the relaxation process or dynamic states, which leads to DW movement with lower/higher energy states and the resulting DW can be moved faster/slower in rough/curved nanowires [11]. Clearly, a deeper understanding of such transformation will aid the interpretation of DW dynamic process under a magnetic field in the low, intermediate and high regimes of the velocity-field characteristic [3, 7, 11, 12], *i.e.* below and above the Walker breakdown field [13]. As closing remarks of chapter 3, our results are a new route-map of quantitative measurement for the transformation of STDWs↔ATDWs. The results are helpful for the determination of TDW configurations in the static state after the application of a magnetic field or electrical current pulse when TDWs are driven by field or electrical current. Moreover, this method can be used for other imaging techniques, *i.e.* MOKE magnetometry [1, 2, 6, 12, 14, 15], in which MOKE signals from the TDW are related to the magnetization components inside or either side of a TDW, the detected signals can be indirectly converted to the degree of asymmetry of the TDW via the region areas inside the TDW. Thus, a combination of this method and MOKE measurement, the transformations of STDWs↔ATDWs↔VDWs during DW propagation can be quantitatively determined. The transformation behavior within DW types was roughly confirmed by the authors in ref. [8, 11, 12], where the pinning behaviour depends on the incoming DW configurations in which a DW propagates through protrusions or notches with different geometries [3, 4, 7, 12, 15-20]. Hence, new structures can be designed to modify the total energy landscape profiles by using the merits of the edge roughness effects to enhance the DW velocity [11, 12], where the edge roughness behaviour was modified by making periodic protrusions with respect to the perfect edges of the structure [12].

4.3 FUTURE WORK

The main results of the project are purely focused on the effects of an external magnetic field on DW creation and propagation in nanowires where the DW configuration/ motion depends on structural effects, *i.e.* structural geometries, edge roughness, thickness gradient [21] (extrinsic parameters). Especially, the created TDW configurations in the relaxed state are strongly affected by the degree of the edge roughness. The TDW

transformations influenced by a changing DW energy landscape [22] created from a changing of the edge roughness behaviour (discussed in chapter 3). Thus, this is an important stage where understanding of the DW configuration is essential before exploring further into the DW propagation process in straight/non-straight nanowires. Moreover, DW propagation in non-straight nanowires was studied by means of horizontal DC and pulsed fields or two DC field directions (see section 2.4.2 and Fig. 2.13, results are not shown here). This aimed to explore the geometrical effects at particular locations in the nanowires affecting the DW propagation processes. Even so, the extrinsic factors have been found to dominate the threshold fields or currents required to propagate DWs in FM nanowires. A question is raised by the above results is, how intrinsic factors affect DW propagation in a magnetic field or electrical current. This should be extended as further plans.

Firstly, regarding the TDW transformation results, one can see that DW creation is a key point for the next steps of exploring the characteristics of DW motion. Our results can be used to quantify the TDW transformation using other techniques, if it is suitable, the structures can be delivered to other research groups where they are expert in MOKE magnetometry [1, 2, 12, 14] and/or XMCD [23, 24]. For instance, a test of MOKE signal processing is essential to be done and compared to our results to find a correlation with the degree of the asymmetry measurements. Moreover, the curved nanowires can be contacted to apply electrical current to pass through the structures to measure DW propagation induced by electrical currents where intrinsic parameters will be characterized, *i.e.* magnetic sample quality (grain size, magnetization reduction at a particular condition), thermal fluctuations (a random-fluctuating thermal field, $\boldsymbol{H}_{\text{thermal}}$, should be included to the effective field, $\boldsymbol{H}_{\text{eff}}$, in Gilbert's dynamic equation) and the spin-transfer torque contribution. In the case where a field and a current simultaneously act on a DW, the equation of motion for the magnetization was considered with inclusion of adiabatic effects [25, 26]. Thus, calculated DW velocity is a good method to determine intrinsic parameters experimentally.

Secondly, based on the results of DW propagation within separated nanowires, in DWTC-like structures (not included in this thesis), this was successfully achieved by a field driven method, as shown in Fig. 4.1. The results are also useful to go further on designing

other structures which are to be potentially applied in domain wall logic gate devices driven by an external field. Moreover, by patterning electrical contacts extended DW propagation by current driven motion with transverse field [27-29] or non-adiabaticity and damping parameters [30-32] and/or Rashba effect [33, 34] can be explored. Hence, the current induced DW propagation method as the further plans for two types of structures were investigated in the thesis, one of them can be illustrated in Fig. 4.1. As a notice, the current driven method is more efficient than the field driven method. Particularly, the optimal DWTC-like structure has an ability to trap, manipulate and release single cells and that are useful for biological and medical applications [35]. However, when the current induced DW motion is studied, Joule heating [36-40] is an issue needs to be considered.

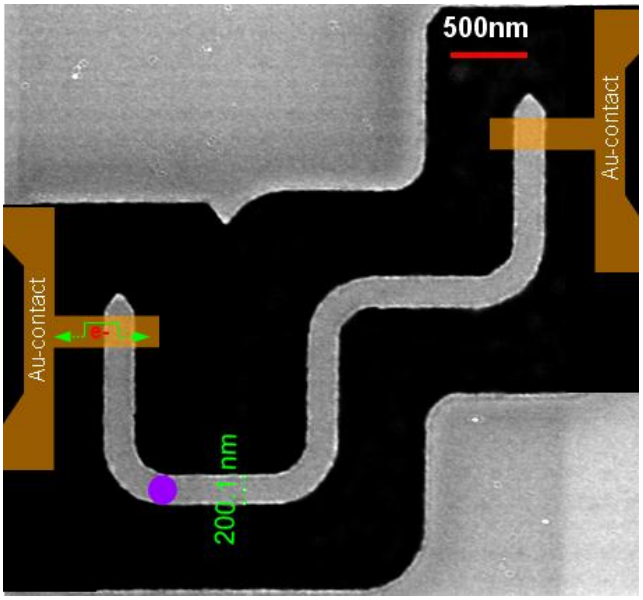

Fig. 4.1 shows an SEM image of the optimal DWTC-like structure which will be contacted with Au-contacts in order to carry out current driven DW propagation. A DW is created at the first corner of the first nanowire (marked a by violet circle) and is subsequently propagated through the chain by an electrical current.

REFERENCES

[1]. D.A. Allwood, G. Xiong, M.D. Cooke, C.C. Faulkner, D. Atkinson, N. Vernier, R.P. Cowburn, *Science* **296** (2002) 2003

[2]. D.A. Allwood, G. Xiong, C.C. Faulkner, D. Atkinson, D. Petit, R.P. Cowburn, *Science* **309** (2005) 1688

[3]. S. S. P. Parkin, M. Hayashi and L. Thomas, *Science* **320** (2008) 190

[4]. G. Hrkac, J. Dean and D.A. Allwood, *Phil. Trans. R. Soc. A* **369** (2011) 3214

[5]. C.H. Marrows and B.J. Hickey, *Phil. Trans. R. Soc. A* **369** (2011) 3027

[6]. P.S. Keatley, V.V. Kruglyak, P. Gangmei and R.J. Hicken, *Phil. Trans. R. Soc. A* **369** (2011) 3115

[7]. O. Boulle, G. Malinowski and M. Kläui, *Mater. Sci. Eng. R* (2011): doi:10.1016/j.mser.2011.04.001

[8]. Y. Nakatani, A. Thiaville, J. Miltat, *J. Magn. Magn. Mater.* **290-291** (2005) 750

[9]. M.J. Donahue and D.G. Porter, *Report No. NISTIR 6376* (*National Institute of Standards and Technology, Gaithersburg, MD*, 1999)

[10]. J.N. Chapman, *J. Phys. D: Appl. Phys.* **17** (1984) 623

[11]. Y. Nakatani, A. Thiaville, J. Miltat, *Nat. Mater.* **2** (2003) 521

[12]. E. R. Lewis, D. Petit, L. O'Brien, A. Fernandez-Pacheco, J. Sampaio, A.V. Jausovec, H.. Zeng, D.E. Read and R.P. Cowburn, *Nat. Mater.* **9** (2010) 980

[13]. N.L. Schryer, L.R. Walker, *J. Appl. Phys.* **45** (1974) 5406

[14]. D. Atkinson, D.A.Allwood, G. Xiong, M.D. Cooke, C.C. Faulkner and R.P. Cowburn, *Nat. Mater.* **2** (2003) 85

[15]. L.K. Bogart, D. Atkinson, K. O'Shea, D. McGrouther and S. McVitie, *Phys. Rev. B* **79** (2009) 054414

[16]. M. Hayashi, L. Thomas, C. Rettner, R. Moriya, S. S. P. Parkin, *Nat. Phys.* **3** (2007) 21

[17]. D. Petit, H.T. Zeng, J. Sampaio, E. Lewis, L. O'Brien, A.-V. Jausovec, D. Read, R.P. Cowburn, K.J. O'Shea, S. McVitie, J.N. Chapman, *Appl. Phys. Lett.* **97**(2010) 233102

[18]. Y. Labaye, L. Berger, J.M.D. Coey, *J. Appl. Phys.* **91** (2002) 5341

[19]. K.J. O'Shea, S. McVitie, J.N. Chapman and J.M.R. Weaver, *Appl. Phys. Lett.* **93**, (2008) 202505

[20]. D. McGrouther, S. McVitie, J.N. Chapman and A. Gentils, *Appl. Phys. Lett.* **91**, (2007) 022506

[21]. O. Petracic, P. Szary, H. Zabel, D. Görlitz and K. Nielsch, *Supperlattices and Mirostructures* **46** (2009) 728

[22]. S. Bance, T. Schreft, G. Hrkac, D. Suess, C. Brownlie. S. McVitie, J. N. Chapman, D. Allwood, *IEEE Trans. Magn.*, **42** (2006) 2966

[23]. J. Stöhr and H.C. Siegmann, *Magnetism*: *From Fundamentals to Nanoscale Dynamics*, Spinger Series on Solid-State Sciences **152** (Heidelberg 2006)

[24]. L. Bocklage, B. Krüger, R. Eiselt, M. Bolte, P. Fischer and G. Meier, *Phys. Rev. B* **78** (2008) 180405R

[25]. E. Martinez, L. Lopez-Diaz, L. Torres, C. Tristan and O. Alejos, *Phys. Rev. B* **75** (2007) 174409

[26]. V.V. Volkov and V.A. Bokov, *Physics of the Solid State* **50** (2008) R199

[27]. D.S. Eastwood, J.A. King, L.K. Bogart, H. Cramman and D. Atkinson, J. Appl. Phys. 109 (2011) 013903

[28]. J. Yang, G.S.D. Beach, C. Knutson and J.L. Erskine, *Phys. Rev. B* (2011) [in press]

[29]. L. Heyne, M. Kläui, D. Backes, T.A. Moore, S. Krzyk, U. Rüdiger, L.J. Heyderman, A.F. Rodríguez, F. Nolting, T.O. Mentes, M.Á. Niño, A. Locatelli, K. Kirsch, R. Mattheis, *Phys. Rev. Lett.* **100** (2008) 066603

[30]. C. Burrowes, A. P. Mihai, D. Ravelosona, J.-V. Kim, C. Chappert, L. Vila, A. Marty, Y. Samson, F. Garcia-Sanchez, L. D. Buda-Prejbeanu, I. Tudosa, E. E. Fullerton and J.-P. Attané, *Nat. Phys.* **6** (2010) 17

[31]. T. Koyama, D. Chiba, K. Ueda, K. Kondou, H. Tanigawa, S. Fukami, T. Suzuki, N. Ohshima, N. Ishiwata, Y. Nakatani, K. Kobayashi, T. Ono, *Nat. Mater.* **10** (2011) 194

[32]. N. Church, J.M. Feinberg and R. Harrison, G^3 **12** (2011) 1

[33]. C. T. Boone, J.A. Katine, M. Carey, J.R. Childress, X. Cheng and I.N. Krivorotov, *Phys. Rev. Lett.* **104** (2010) 097203

[34]. I.M. Miron, T. Moore, H. Szambolics, L.D.B. Prejbeanu, S. Auffret, B. Rodmacq, S. Pizzini, J. Vogel, M. Bonfim, A. Schuhl and G. Gaudin, *Nat. Mater.* **10** (2011) 419

[35]. M. Donolato, A. Torti, N. Kostesha, M. Deryabina, E. Sogne, P. Vavassori, M.F. Hansen and R. Bertacco, *Lab Chip* **11** (2011) 2976

[36]. C.Y. You, I.M. Sung and B.K. Joe, *Appl. Phys. Lett.* **89** (2006) 222513

[37]. K.J. Kim, J.C. Lee, S.B. Choe and K.H. Shin, *Appl. Phys. Lett.* **92** (2008) 192509

[38]. A. Yamagushi, S. Nasu, H. Tanigawa, T. Ono, K. Miyake, K. Mibu and T. Shinjo, *Appl. Phys. Lett.* **86** (2005) 012511

[39]. F. Léonard, *Appl. Phys. Lett.* **98** (2011) 103101

[40]. H. Fangohr, D.S. Chernyshenko, M. Franchin, T. Fischbacher, Guido Meier, *Phys. Rev. B* **84** (2011) 054437